ISTANBUL TECHNICAL UNIVERSITY ★ GRADUATE SCHOOL

DESIGN AND EVALUATION OF HIGH-K DIELECTRIC MATERIALS FOR LOW-POWER ‘GREEN’ OFET-BASED SENSORS

Ph.D. THESIS

Aybüke TAVASLI

Department of Materials Science and Engineering

Materials Science and Engineering Programme

OCTOBER 2024

ISTANBUL TECHNICAL UNIVERSITY ★ GRADUATE SCHOOL

DESIGN AND EVALUATION OF HIGH-K DIELECTRIC MATERIALS FOR LOW-POWER 'GREEN' OFET-BASED SENSORS

Ph.D. THESIS

Aybüke TAVASLI
(521192001)

Department of Materials Science and Engineering

Materials Science and Engineering Programme

Thesis Advisor: Prof. Dr. Levent TRABZON
Thesis Co-Advisor: Assist. Prof. Dr. Sheida FARAJİ

OCTOBER 2024

ISTANBUL TEKNİK ÜNİVERSİTESİ ★ LİSANSÜSTÜ EĞİTİM ENSTİTÜSÜ

DÜŞÜK GÜÇLÜ ‘YEŞİL’ OFET TABANLI SENSÖRLER İÇİN YÜKSEK-K DİELEKTRİK MALZEMELERİNİN TASARIMI VE DEĞERLENDİRMESİ

DOKTORA TEZİ

Aybüke TAVASLI
(521192001)

Malzeme Bilimi ve Mühendisliği Anabilim Dalı

Malzeme Bilimi ve Mühendisliği Programı

Tez Danışmanı: Prof. Dr. Levent TRABZON
Eş Danışman: Dr. Öğr. Üyesi Sheida FARAJİ

EKİM 2024

Aybüke TAVASLI, a Ph.D. student of İTU Graduate School student ID 521192001, successfully defended the dissertation entitled "DESIGN AND EVALUATION OF HIGH-K DIELECTRIC MATERIALS FOR LOW-POWER 'GREEN' OFET-BASED SENSORS", which she prepared after fulfilling the requirements specified in the associated legislations, before the jury whose signatures are below.

Thesis Advisor : **Prof. Dr. Levent TRABZON** ....
İstanbul Technical University

Co-advisor : **Assist. Prof. Dr. Sheida FARAJİ** ....
İstanbul Technical University

Jury Members : **Assoc. Prof. Dr. Tufan Coşkun KARALAR**
İstanbul Technical University ....

Assoc. Prof. Dr. Mustafa Berke YELTEN
İstanbul Technical University ....

Assoc. Prof. Dr. Eda GOLDENBERG
Gebze Technical University ....

Assist. Prof. Dr. Amir NAVİDFAR ....
Bahçeşehir University

Dr. Leszek A. MAJEWSKİ ....
University of Manchester

Date of Submission : 20 September 2024
Date of Defense : 17 October 2024

To my family,

FOREWORD

I would like to express my sincere gratitude to my scientific family, particularly my esteemed supervisor, Prof. Dr. Levent TRABZON, and my esteemed co-advisor, Assist. Prof. Dr. Sheida FARAJİ. Working with them throughout my Ph.D. journey was both a great opportunity and an immense privilege. I am deeply grateful for Prof. Dr. TRABZON’s unwavering support; he has been not only a supervisor but also a scientific mentor and father figure to me. I am equally thankful for the invaluable support of Assist. Prof. Dr. Sheida FARAJİ. She has been a true scientific mentor, standing shoulder-to-shoulder with me throughout this study. I am proud that we were able to contribute as women in STEM.

I am thankful to my thesis committee members; Assoc. Prof. Dr. Mustafa Berke YELTEN, Assoc. Prof. Dr. Tufan Coşkun KARALAR and Assoc. Prof. Dr. Eda GOLDENBERG for their contributions throughout my thesis progress meetings. They enhanced my scientific view and gave me the courage to express my study confidently.

I give my special thanks to Prof. Dr. Berta GÓMEZ-LOR, Dr. Mohammed Afsar UDDİN and my friends at ICMM-CSIC, Universidad Autónoma de Madrid for their heartfelt help and support in my studies. Another special thanks go to Dr. Leszek A. MAJEWSKİ at the University of Manchester for his guidance and scientific discussion. It was an honor to be a visiting researcher there and benefit from their scientific facilities. I would like to thank all researchers for their continuous help at the UoM.

I express my gratitude to the Scientific and Technological Research Council of Türkiye (TÜBİTAK), Science Fellowships and Grant Programme (BİDEP) and İstanbul Technical University BAP. This Ph.D. thesis was supported and funded by 2232 TÜBİTAK & 2211 BİDEP (project number 118C365) and İTU BAP project with project number 44645.

I would like to express my thanks to my colleagues at İTU MEMS for their valuable brainstorming by discussing the scientific aspects of our studies and cheerful outdoor activities on our campus. Experiments in a laboratory without friendly labmates are like foods without salt.

The words would not be enough to express my gratitude to my lovely family. They always believed me and supported me whatever the conditions. My dear mom, dad and brother always appreciated my efforts and wiped out my tears and sweat. I could not do anything without their sincere support. I love them to the moon and back.

Per aspera ad astra

October 2024

Aybüke TAVASLI
(Biomedical Engineer)

TABLE OF CONTENTS

Page

ABBREVIATIONS

A : Acceptor
AI : Artificial intelligence
BHJ : Bulk heterojunction
BGBC : Bottom gate – bottom contact
BGTC : Bottom gate – top contact
BL : Bottom-light
BP : Blood pressure
BSC : Back sweep current
BTz : PP(C14)DTBTz(HD)
C8-BTBT : 2,7-dioctyl[1]benzothieno[3,2-b][1]benzothiophene
CEC : Cyanoethyl cellulose
C_i : Areal capacitance
CPU : Central Processing unit
D : Drain
D : Donor
DMF : N, N-dimethylformamide
DPP-DTT : Poly[2,5-(2-octyldodecyl)-3,6-diketopyrrolopyrrole-alt-5,5-(2,5-di(thien-2-yl)thieno [3,2-b]thiophene)]
ECG : Electrocardiography
EGT : Electrolyte-gated transistor
EPSC. : Excitatory postsynaptic current
EPSP. : Excitatory postsynaptic potential
EA : Electron affinity
FET : Field-effect transistor
FeFET : Ferroelectric FET
G : Gate
HbO_2 : Oxyhemoglobin
Hb : Hemoglobin
HOMO : Highest occupied molecular orbital
HR : Heart rate

HRV : Heart rate variability

IoT : Internet of Things

IR : Infrared

IP : Ionization potential

IPA : Isopropyl alcohol

IPSP : Inhibitory postsynaptic potentials

LR-OFET : Light-receiving OFET

LTP : Long-term potentiation

LTP : Long-term plasticity

LUMO : Lowest unoccupied molecular orbital

MIM : Metal insulator metal

NC : Nanocomposite

NIR : Near-infrared

NP : Nanoparticle

OECT : Organic electrochemical transistor

OFET : Organic field-effect transistor

OPT : Organic phototransistor

OPV : Organic photovoltaic

OSC : Organic semiconductor

OTFT : Organic thin film transistor

OTS : *n*- octadecyltrichlorosilane

PCBM : [6,6]-Phenyl-C61-butyric acid methyl ester

PDD-TT : Poly(5,7-bis(4-decanyl-2-thienyl)-thieno(3,4-b) diathiazole-thiophene-2,5)

PEDOT:PSS : Poly(3,4-ethylenedioxythiophene):Poly(styrene sulphonic acid

PET : Polyethylene terephthalate

P3HT : Poly(3-hexylthiophene-2,5-diyl)

PI : Polyimide

PMMA : Polymethylmethacrylate

POC : Point-of-care

PP : Pulse pressure

PPG : Photoplethysmography

PPT : Polymer organic phototransistor

PT : Phototransistor

PTFE : Poly(tetrafluoroethylene)

PVD	: Physical vapor deposition
PVDF-HFP	: Poly(vinylidene fluoride-co-hexafluoropropylene)
S	: Source
SAM	: Self-assembled monolayer
SEM	: Scanning electron microscope
SOPT	: Small molecule organic phototransistor
SpO_2	: Arterial oxygen saturation
SPT	: Synaptic phototransistor
STP	: Short-term plasticity
SWIR	: Short-wave infrared
TGBC	: Top gate – bottom contact
TGTC	: Top gate – top contact
TL	: Top-light
TrFE	: Trifluoroethylene
UV	: Ultraviolet
Vis	: Visible
VOC	: Volatile organic compound
W	: Synaptic weight
XRD	: X-ray diffraction
ZrO_2	: Zirconium oxide

SYMBOLS

A : Area
Au : Gold
Al : Aluminium
X : Electron affinity
D* : Detectivity
d : Thickness
E_b : Binding energy
E_g : Bandgap
ε_r : Relative permittivity of the dielectric material
ε_0 : Permittivity of the free space (vacuum)
I_{DS} : Drain current
I_{ph} : Photocurrent
I_{dark} : Dark current
I_{on} / I_{off} : On current / off current
μ : Charge carrier mobility
Φ : Work function
P : Photosensitivity
P_{opt} : Optical power
R : Photoresponsivity
R_{bulk} : Bulk resistance
R_C : Contact resistance
$R_{channel}$: Channel resistance
S : Subthreshold swing
SS : Subthreshold slope
V_G : Gate voltage
V_{DS} : Source-drain voltage
V_{th} : Threshold voltage
Wt : Weight

LIST OF TABLES

Page

LIST OF FIGURES

Page

DESIGN AND EVALUATION OF HIGH-K DIELECTRIC MATERIALS FOR LOW-POWER 'GREEN' OFET-BASED SENSORS

SUMMARY

Today, people in developed countries live in modern conditions with high technology, accessible healthy nutrition, and advanced medical treatment. In this age of technology, investments in electronic sensors are significant. For example, the detection of volatile organic compounds through gas sensors is a pressing need for public health, particularly in cities where industrial plants are present. The need for sensors extends beyond gas sensors. In certain regions of underdeveloped countries, women and children require point-of-care sensors for emergencies. Patients and medical personnel prefer home-assisted, low-power, and flexible sensors due to innovative material choices and design advantages. Detection of analytes or oxygen concentration in blood is another crucial point in the biomedical field. These kinds of detections and tracements of analytes can be possible via Organic field-effect transistor (OFET)-based sensors. OFET-based sensors can achieve signal amplification and decrease the noise of the collected signals. A photoplethysmography device is the best example that comes to mind as an organic phototransistor (OPT) application. OPTs, namely light-receiving organic field-effect transistors (LR-OFETs), can receive light, and then send it through the tissue. Following that transmitted or absorbed light can give the oxygen concentration in blood. These all offer great opportunities to achieve high quality in chemical sensors and biosensors.

OFETs can be designed in four different configurations based on the position of the metal electrodes. These are bottom gate – bottom contact (BGBC), bottom gate – top contact (BGTC), top gate – bottom contact (TGBC) and top gate – top contact (TGTC). Organic phototransistors have the same structure as OFETs. An organic semiconductor (OSC) is the active layer component of the device. This organic compound can be a small molecule or polymer that is solution-processable and provides low-cost and easy mass production at low temperatures. Their tunable chemical structures provide superior advantages over conventional inorganic semiconductors. They feature a conjugation structure that facilitates charge transport through the molecule. Another component is a dielectric layer, responsible for enabling the insulator layer in the parallel plate capacitor of the device. One plate is the gate electrode, and the other comprises the source and drain electrodes. This configuration is known as the "metal insulator metal" (MIM) structure. Charge carriers are collected between the insulator and the semiconductor when the gate voltage is applied. A high-k constant dielectric material can provide a high capacitance value, enabling the OFET device to operate under low voltage (< 3 V). Nanoparticles (NPs) are excellent candidates for creating high-k constant nanocomposites (NCs) by blending them with dielectric polymers.

This thesis aims to design and focus on the exploration of OFET-based sensors using solution-processed polymeric dielectrics and organic semiconductors. It also investigates the potential of synthetic and natural polymeric dielectrics blended with nanoparticles on capacitors. The thesis is organised into five chapters: The first two

chapters consist of the published review articles on OFET and OPT devices. They provide a comprehensive background on these devices, supported by examples from literature, along with explanations of the mechanisms of the devices. The third and fourth chapters present the experimental research findings related to capacitors and OFET devices, offering new insights and data. The last chapter summarises the results, evaluates the research, discusses the challenges encountered, and concludes the thesis with planned recommendations for future work.

The first chapter consists of a published review article. This is a detailed review article that explains the structure of the OFET devices and their components by giving examples from the literature. OFET and OPT devices, as well as their operation mechanisms and basic equations, are illustrated. Sections 1.1 and 1.2 cover the principles of OFET, OPT, and OSC. Sections 1.3 and 1.4 explore applications of OPT and their future perspectives, respectively.

The second chapter sheds light on the artificial synapses based on OPT devices. This chapter covers a published review article. Among the sensor devices used to build artificial synapses, OFETs are one of the most promising candidates for neuromorphic computers and bioelectronics. Sections 2.3 and 2.4 provide comprehensive knowledge and basic parameters for OPT devices and solution process techniques. Section 2.5 underpins the topic with examples from the literature.

In the third chapter, nanocomposite capacitors for OFET applications are investigated and findings are reported. This chapter is in-press now. Poly(vinylidene fluoride-co-hexafluoropropylene) (PVDF-HFP) is one of the most used non-natural, ferroelectric, high-*k* dielectric materials, and cyanoethyl cellulose (CEC), is a natural dielectric polymer with a high-*k* value were deployed as polymeric matrixes. They are appropriate choices as dielectrics because of their high-*k* value and solution-processability at low temperatures. Zirconium oxide (ZrO_2) nanoparticles, namely zirconia NPs were blended at different weight (wt) % concentrations (1 wt %, 1.5 wt %, 5 wt % and 10 wt %). To design a bottom-gate configuration, aluminium (Al) was evaporated on the top of a pre-cleaned glass substrate using thermal evaporation at approximately 90 nm thickness. The prepared dielectric solutions were spin-coated on the Al-coated glass substrate at specific spin speeds for each polymer. Then, Al was coated again as a second plate of the capacitor to create Al/insulator/Al. The electrical properties of all MIM capacitor samples were measured within a defined frequency range (50 Hz – 1 MHz). C-V and C-f curves of the devices were drawn and interpreted for the electrical performance of the devices. Calculated areal capacitance (C_i, nF/cm^2) values were provided. The surface wettability properties and crystalline structures of the dielectric layers of the NC MIM capacitors were examined. Results showed that nanoparticle content in the polymer matrix had a significant impact on the performance of the devices. Results indicated that PVDF-HFP is more suitable because of its high C_i value and hydrophobic structure compared to the CEC polymeric matrix. 5 % wt ZrO_2 can be the optimum content for two dielectrics, C_i of CZ5 is 68.85 ± 2.16 nF/cm^2 and PZ5 is 57.79 ± 4.65 nF/cm^2 at 1 kHz. The dielectric constants (*k*) were 28.61 ± 0.1 and 35.68 ± 1.99 for CEC + ZrO_2 (5 wt %) and PVDF-HFP + ZrO_2 (5 wt %), respectively. Although leakage current density went up with the increased amount of NPs, All samples gave $< 1.75\text{x}10^{-6}$ leakage current density (A/cm^2) at 2 V which is optimum and desirable for applications in sensor devices.

In the fourth chapter, bioorganic BGTC OFET devices are designed, and their electrical performances are examined. Natural and organic dielectrics; mango sap, cactus sap and aloe vera were applied and tested regarding their dielectric performances in the MIM structure. To design a bottom-gate configuration, aluminium (Al) was evaporated on the top of a pre-cleaned glass substrate using thermal evaporation at approximately 90 nm thickness. The prepared dielectric solutions were spin-coated on the Al-coated glass substrate at special spin speeds for each polymer. Then, Al was coated again as a second plate of the capacitor to create Al/insulator/Al. As organic semiconductors, synthesized ones (PP(C14)DTBTz(HD) and PP(C14)DTFBTz(HD) in chloroform solvent) and commercial ones (Poly[2,5-(2-octyldodecyl)-3,6-diketopyrrolopyrrole-alt-5,5-(2,5-di(thien-2-yl)thieno [3,2-b]thiophene)] (DPP-DTT)) were spin-coated on the organic dielectric layers. Following that, gold (Au) metal (~ 40 nm thickness) was evaporated using a source and drain mask under thermal evaporation. The electrical properties of all MIM capacitor samples were measured within a defined frequency range (50 Hz – 1 MHz). The electrical properties of OFET devices were evaluated using a probe station. C-V, C-f and I-V curves of the devices were drawn and interpreted for the electrical performance of the devices. Calculated areal capacitance (C_i, nF/cm^2) values were provided. Cactus sap exhibited a high leakage current. Moreover, applying the cactus sap coating posed significant challenges due to its liquid state. It failed to function effectively as a dielectric in OFET devices. However, mango sap and aloe vera were successfully coated even though it was also in a liquid sap form. It was found that it can be utilised as a dielectric layer for OFET devices. It was seen that mango sap dielectric thicknesses influenced the areal capacitance (C_i) values of the MIM capacitors that the thinner layer (spin speed = 2500 rpm) had a 30 % higher value (42.56 ± 5.29 nF/cm^2 at 1 kHz). Leakage current densities were 3.64×10^{-7} A/cm^2 at 2 V for mango sap coated at 2500 rpm, and 6.88×10^{-7} A/cm^2 at 2 V for mango sap coated at 2000 rpm. Cactus sap was used as a dielectric layer with a PMMA passivating layer and gave 93.53 ± 8.23 nF/cm^2 areal capacitance at 1 kHz with < 10^{-6} A/cm^2 leakage current densities. DPP-DTT:PMMA-based OFET devices showed ~ 10 on/off ratios for mango sap-based devices and 3.5×10^3 on/off ratios for aloe vera-based devices. Aloe vera dielectric-based devices demonstrated low leakage current densities (< 10^{-8} A/cm^2 at 2 V) with high mobilities (μ_{sat}=0.6 ± 0.1 cm^2 /Vs of aloe vera + PMMA-based devices).

DÜŞÜK GÜÇLÜ 'YEŞİL' OFET TABANLI SENSÖRLER İÇİN YÜKSEK-K DİELEKTRİK MALZEMELERİN TASARIMI VE DEĞERLENDİRMESİ

ÖZET

Günümüzde yüksek teknolojiye sahip algılayıcı ve dönüştürücü cihazların kullanım alanı giderek artmaktadır. Gelişen ve gelişmekte olan ülkelerde yaşamın hemen her alanında kullanılan elektronik temelli sensör cihazları, sunduğu önemle birlikte vazgeçilmezliğini ortaya koymuştur. Genel olarak çevre ile ilgili çalışmalar, tıbbi çalışmalar ve güvenlik alanında yapılan çalışmalar sensörlerin kullanım alanlarının başında gelmektedir. Tüm bu alanlar erişilebilir sağlıklı beslenme, modern tıbbi olanaklara ulaşım ve güvenli bir ortamda sağlıklı yaşama konusunda bireylere hak ettiği özgürlükleri sağlamaktadır.

Şehir yaşamlarında artan sanayi ve trafik ile birlikte boy gösteren kötü hava kalitesi halk sağlığını olumsuz etkilemektedir. Hava kalitesinin iyileştirilmesi ve kontrol edilmesi için gaz sensörleri kullanılabilir. Bu cihazlar uçucu organik bileşikleri tespit edebilir. Sanayi atıklarının temiz, doğal sulara bırakılması da halk sağlığı için bir tehdit oluşturmakta ve bu analitlerin tespitlerinin yerinde hızlıca gerçekleşmesi sensörlerle mümkün olabilir. Az gelişmiş ülkelerde ise, özellikle kadınlar ve çocuklar için sağlıklı gıdaya ve doktora erişim hala istenilen seviyelerde değil. Bu bölgelerde acil durumlar için hastaneye ve tıbbi personele minimum düzeyde ihtiyaç duyan, hızlıca ve kolay teşhis yapabilecek ve tedavi edebilecek sensörlere ihtiyaç var. Bu sensörlere bu denli ihtiyaç duyulması ve kullanım alanlarının fazla olması sensör tasarımı ve malzeme seçimiyle ilgili konuları da beraberinde getirmektedir. Çünkü bu cihazların kullanımı arttıkça onların çevre dostu malzemelerden yapılması ve elektronik atık haline geldiğinde doğayı tehdit etmeden bozunması göz önünde bulundurulması gereken bir diğer husustur.

Hem hızlı ve kolay çalışabilmesi, hem de düşük maliyetle üretilip fabrikasyon üretime uygun olması sebebiyle organik alan etkili transistor (OFET) temelli sensörler öne çıkmaktadır. Bu cihazlar düşük gerilimle çalışabilir. Organik yarı iletken (OSC) ve yalıtkan kısımları için malzeme seçiminde geniş bir yelpaze sunmakla beraber, kullanılan substrat seçimi de esnek, biyouyumlu, biyobozunur ve hafif cihaz üretilmesine olanak sağlar. Ayrıca taşınabilir ve küçük boyutlarda tasarlanabilen bu cihazlar evde kullanıma uygundur. Çevre ile ilgili çalışmalarda, örneğin dere suyu ile ilgili bir çalışmada bu sensörleri örneğin alındığı yerde kullanabilmek mümkündür.

Işık alan OFET sensörler (LR-OFET) organik fototransistör (OPT) olarak adlandırılır. Kandaki analitlerin veya oksijen konsantrasyonunun tespiti, biyomedikal alanda bir diğer önemli noktadır. Bu tür tespitler OPT sensörleri ile mümkün olabilir. OFET tabanlı sensörler, sinyal amplifikasyonu sağlar ve toplanan sinyallerin gürültüsünü azaltır. Bir fotopletismografi cihazı OPT uygulaması olarak akla gelen en iyi örnektir. OPT'ler ışığı alır ve sonra dokuya gönderir. Ardından iletilen veya emilen ışık kandaki oksijen konsantrasyonunu verir.

OFET'ler metal elektrotların pozisyonuna göre dört farklı konfigürasyonda tasarlanabilir. Bunlar alt kapı - alt temas (BGBC), alt kapı - üst temas (BGTC), üst kapı - alt temas (TGBC) ve üst kapı - üst temastır (TGTC). Organik fototransistörler OFET'lerle aynı tasarıma sahiptir. Bir organik yarı iletken, cihazın aktif katmanıdır. Bu organik bileşik bir çözücüde çözünebilir ve düşük sıcaklıklarda, düşük maliyetli ve kolay seri üretim sağlayan küçük bir molekül veya polimer olabilir. Araştırmanın amacına göre ayarlanabilir kimyasal yapıları, geleneksel inorganik yarı iletkenlere göre üstün avantajlar sağlar. Molekül boyunca yük taşınmasını kolaylaştıran bir kimyasal konjugasyon yapısına sahiptirler. OFET'lerin bir diğer bir bileşeni, cihazın paralel plaka kapasitöründeki yalıtkan tabakayı etkinleştirmekten sorumlu bir dielektrik tabakadır. Burada bir plakayı kapı elektrot, diğer plakayı da kaynak ve drenaj elektrotları oluşturur. Bu konfigürasyona "metal yalıtkan metal" (MIM) yapısı da denir. Kapı elektrotuna bir gerilim uygulandığında yük taşıyıcıları yalıtkan ve yarı iletken arasında toplanır. Yüksek *k* sabitli ya da ince kalınlığa sahip bir yalıtkan malzeme, OFET cihazının düşük voltajda (< 3 V) çalışmasını sağlayan yüksek bir kapasitans değeri sağlayabilir. Nanopartiküller (NP), dielektrik polimerlerle harmanlanarak yüksek k sabitli nanokompozitler (NC) oluşturmak için tercih edilen en uygun malzemelerdendir.

Bu tez, çözelti halindeki polimerik dielektrikler ve organik yarı iletkenler kullanarak OFET tabanlı sensörleri tasarlamayı, fiziksel ve elektirksel karakterizasyonlarını yapmayı amaçlamaktadır. Ayrıca, kapasitörler üzerinde nanopartiküllerle harmanlanmış sentetik ve doğal polimerik dielektriklerin potansiyel etkilerini de araştırmaktadır. Tez ana hatlarıyla beş bölümden oluşmaktadır: İlk iki bölüm OFET ve OPT cihazları hakkında yayınlanmış derleme makalelerinden oluşmaktadır. Bu cihazlar hakkında literatürden örneklerle desteklenen kapsamlı bir temel oluşturulmuştur ve cihazların mekanizmalarının açıklamalarını sunmaktadırlar. Üçüncü ve dördüncü bölümler, kapasitörler ve OFET cihazlarıyla ilgili deneysel araştırma bulgularını sunarak yeni içgörüler ve veriler sunmaktadır. Son bölüm sonuçları özetlemekte, araştırmayı değerlendirmekte, karşılaşılan zorlukları tartışmakta ve tezi gelecekteki yapılması planlanan ve önerilen çalışmalarla sonlandırmaktadır.

İlk bölüm yayınlanmış bir derleme makalesinden oluşmaktadır. Bu makale, literatürden örnekler vererek OFET cihazlarının ve bu cihazların bileşenlerinin yapısını açıklayan ayrıntılı bir derlemedir. OFET ve OPT cihazlarının çalışma mekanizmaları ve parametreleri temel denklemlerle ve görsellerle verilmiştir. Bölüm 1.1 ve 1.2'de OFET, OPT ve OSC'nin temel prensipleri anlatılmıştır. Bölüm 1.3 ve 1.4'te, sırasıyla OPT'nin uygulamalarına ve gelecekteki muhtemel çalışmalara yer verilmiştir.

İkinci bölüm, OPT cihazlarına dayalı yapay sinapslara ışık tutan, yayınlanmış bir inceleme makalesini ele almaktadır. Yapay sinapsları oluşturmak için kullanılan sensör cihazları arasında OFET'ler, nöromorfik bilgisayarlar ve biyoelektronikler için başarılı sonuç veren sensörlerden biridir. Bölüm 2.3 ve 2.4'te, OPT cihazları ve çözelti halinde bulunan malzemeler için kaplama teknikleri için kapsamlı bilgi ve temel parametreler verilmiştir. Bölüm 2.5'te konu literatürden örneklerle desteklenmiştir.

Üçüncü bölümde, OFET uygulamaları için nanokompozit kapasitörler araştırılmış ve bulgular paylaşılmıştır. Bu bölüm şu anda bir dergide makale olarak basılması için gönderilmiştir. Poli(viniliden florür-ko-hekzafloropropilen) (PVDF-HFP), en çok kullanılan doğal olmayan, ferroelektrik, yüksek *k* değerine sahip yalıtkan malzemelerden biridir. Siyanoetil selüloz (CEC) yüksek *k* değerine sahip olmasının yanı sıra doğal bir yalıtkan malzemedir. Bu iki farklı polimer bu çalışmada polimerik matrisler olarak kullanılmıştır. Yüksek *k* değerleri ve düşük sıcaklıklarda çözelti işlenebilirlikleri nedeniyle yalıtkan malzeme olarak uygun seçimlerdir. Zirkonyum oksit (ZrO_2) nanopartikülleri (NP), ağırlıkça farklı konsantrasyonlarında (% 1, % 1,5, % 5 ve % 10) olacak şekilde polimer matrislerle karıştırıldı ve böylece nanokompozit bir yapı elde edildi. Alt kapı (BG) konfigürasyonunu tasarlamak için, alüminyum (Al), yaklaşık 90 nm kalınlıkta termal buharlaştırma kullanılarak önceden temizlenmiş bir cam alt tabakanın üstünde kaplandı. Hazırlanan dielektrik çözeltiler, her polimer için belirli dönüş hızlarında Al kaplı cam alt tabaka üzerine döndürerek kaplama ile kaplandı. Daha sonra, Al, Al/yalıtkan/Al MIM kapasitör oluşturmak için kapasitörün ikinci bir plakası olarak tekrar kaplandı. Tüm MIM kapasitör numunelerinin elektriksel özellikleri tanımlanmış bir frekans aralığında (50 Hz – 1 MHz) ölçüldü. Cihazların elektriksel performansını göstermek için cihazların C-V ve C-f eğrileri çizildi ve yorumlandı. Hesaplanan alan kapasitansı (C_i, nF/cm^2) değerleri grafiklerde verildi. NC MIM kapasitörlerinin dielektrik katmanlarının yüzey ıslanabilirlik özellikleri ve kristal yapıları incelendi. Sonuçlar, polimer matristeki nanopartikül içeriğinin cihazların performansı üzerinde önemli bir etkiye sahip olduğunu gösterdi. Nanopartikül eklendikçe yalıtkan malzemelerin hidrofilik özelliğinin arttığı görüldü. Saf CEC için 63.79° ± 1.25° temas açısı elde edildi, ardından eklenen ağırlıkça % 5 ZrO_2 nanopartikül ile yalıtkanın hidrofilisite değeri arttı ve temas açısı 39.93° ± 1.82° olarak ölçüldü. PVDF-HFP yalıtkan temelli malzemelerde ise ZrO_2 katkısının hidrofilsite üzerinde önemli katkısının olmadığı görüldü. PVDF-HFP yalıtkan malzeme kullanılarak elde edilen kapasitörlerde ölçülen alansal kapasitans değeri nanopartikül ilavesi ile birlikte ciddi derecede arttı. Katkısız PVDF-HFP polimerli kapasitörün değeri 38.2 ± 2.47 nF/cm^2 iken ağırlıkça 10 % ZrO_2 NP ilavesi ile 2 kattan fazla artarak (% 140) 91.86 ± 6.1 nF/cm^2 ye ulaştı. Benzer şekilde CEC temelli kapasitörlerde % 45 iyileştirilmiş kapasitör değeri (CZ10, 76 ± 3.03 nF/cm^2) gösterdiler. Ancak, nanopartiküllerin dielektrik tabakada kümelenmesi ve yüzey pürüzlülüğünün artması nedeniyle kaçak akım istenmeyen şekilde küçük bir miktar arttı. En düşük kaçak akım yoğunluğu $9{,}58\times10^{-8}$ A/cm^2 olarak CZ5 yalıtkan temelli kapasitörlerde ölçüldü. Tüm örnekler 10^{-7} A/cm^2'den düşük kaçak akım yoğunlu göstererek yüksek elektirksel performans sağladılar. *k* değerleri (yalıtkanlık sabiti değerleri) saf CEC için 16,31 ± 1,22'den CZ5 için 28,61 ± 0,1'e yükseldi. Benzer şekilde, PVDF-HFP temelli örneklerde 10,98 ± 1,09'dan (P) 35,68 ± 1,99'a (PZ5) önemli ölçüde artan bir eğilim görüldü. Ağırlıkça % 5 ZrO_2 katkılı PVDF-HFP yalıtkan katmanlar, saf PVDF-HFP dielektriğe kıyasla *k* değerini üç kat iyileştirirken, kaçak akım yalnızca 10^2 kat arttı.

Dördüncü bölümde, biyoorganik BGTC OFET cihazları tasarlanmış ve elektriksel performansları incelenmiştir. Doğal ve organik dielektrikler olan mango özü, kaktüs özü ve aloe vera bu çalışmada uygulandı ve MIM yapısındaki dielektrik performansları açısından test edildi. Alt kapılı (BG) bir yapılandırma tasarlamak için, alüminyum (Al), yaklaşık 90 nm kalınlığında termal buharlaştırma kullanılarak önceden temizlenmiş bir cam alt tabakanın üstüne kaplandı. Hazırlanan dielektrik çözeltiler, her polimer için özel dönüş hızlarında Al kaplı cam alt tabaka üzerine döndürülerek kaplandı. Daha sonra, Al, Al/yalıtkan/Al oluşturmak için kapasitörün ikinci plakası olarak tekrar kaplandı. Organik yarı iletkenler olarak, sentezlenenler (PP(C14)DTBTz(HD) ve PP(C14)DTFBTz(HD)) ve ticari olanlar (Poli[2,5-(2-oktildodesil)-3,6-diketopirrolopirrol-alt-5,5-(2,5-di(tien-2-il)tieno [3,2-b]tiofen)] (DPP-DTT)) kloroform çözücüsünde çözündürüldükten sonra organik yalıtkan katmanlar üzerine döndürerek kaplama ile kaplandı. Bunu takiben, altın (Au) metali (~ 40 nm kalınlık) termal buharlaştırma altında bir elektrot maskesi kullanılarak kaplandı. Tüm MIM kapasitör örneklerinin elektriksel özellikleri tanımlanmış bir frekans aralığında (50 Hz – 1 MHz) ölçüldü. OFET cihazlarının elektriksel özellikleri bir prob istasyonu kullanılarak değerlendirildi. Cihazların elektriksel performansını göstermek için C-V, C-f ve I-V eğrileri çizildi ve yorumlandı. Hesaplanan alan kapasitans (C_i, nF/cm^2) değerleri grafiklerde verildi. Kaktüs özü yüksek bir kaçak akım gösterdi. Dahası, kaktüs özü kaplamasının uygulanması, içersinde su bileşeninin yüksek olması nedeniyle önemli zorluklar ortaya çıkardı. OFET cihazlarında dielektrik olarak etkili bir şekilde işlev görmedi. Ancak, mango özü ve aloe vera sıvı özsu formunda olmalarına rağmen başarıyla kaplandı ve görece daha düşük kaçak akım sergiledi. OFET cihazları için dielektrik katman olarak kullanılabileceği sonuçlarla gösterildi. Mango özü yalıtkanın farklı kalınlıklarda kaplanmasının MIM kapasitörlerin alan kapasitansı (C_i) değerlerini etkilediği, daha ince olan katmanın (dönme hızı = 2500 rpm) alan kapasitans değerinin % 30 daha yüksek (1 kHz'de 42,56 ± 5,29 nF/cm^2) olduğu görüldü. Kaçak akım yoğunlukları, 2500 rpm'de kaplanmış mango özü için 2 V'da 3,64x10^{-7} A/cm^2 ve 2000 rpm'de kaplanmış mango özü için 2 V'da 6,88x10^{-7} A/cm^2 idi. Kaktüs özü, bir PMMA pasifleştirme tabakası ile bir yalıtkan tabaka olarak kullanıldı ve <10^{-6} A/cm^2 kaçak akım yoğunluklarıyla (1 kHz'de) 93,53 ± 8,23 nF/cm^2 değerini verdi. Aloe vera yalıtkan malzemesi tek başına kullanıldığında 124.17 ± 2.36 nF/cm^2, PMMA ile birlikte çift katmanlı olarak kullanıldığında 85.72 ± 1.46 nF/cm^2 alan kapasitans değerleri gösterdi. DPP-DTT:PMMA tabanlı OFET cihazları mango özü tabanlı cihazlarda ~ 10 açık/kapalı oranı ve aloe vera tabanlı cihazlarda 3,5x10^3 açık/kapalı oranı gösterdi. Aloe vera dielektrik tabanlı cihazlar yüksek taşıyıcı yük hızı (μsat=0,6 ± 0,1 cm^2/Vs aloe vera + PMMA tabanlı cihazlar) ve düşük kaçak akım yoğunlukları (2 V'da < 10^{-8} A/cm^2) gösterdi. Kaktüs temelli OFET cihazlar ise yüksek kapı akımı sebebiyle düşük elektriksel özellik sergiledi.

1. INTRODUCTION[1]

A phototransistor (PT) is a type of photodetector that converts an incident light signal into a detectable electrical signal. This three-electrode device amplifies the signal, reduces the noise and provides superior functionality to other photodetector devices, such as photodiodes [1–4]. Phototransistors have been used for decades in a variety of fields such as biomedical applications, optical communications, environmental and industrial studies, disaster weather prediction and fire warnings (Figure 1.1). Novel optical devices in biomedical applications can be more reliable, and rapid diagnosis and treatment can be achieved. Technological and scientific requirements led to the invention of new means of optoelectronic devices, in particular, those based on field-effect transistors (FETs) [2,5–8]. Conventional phototransistors are based on inorganic semiconductors which belong to IV, III - V and II – VI groups of the periodic table [4,6,9–11].

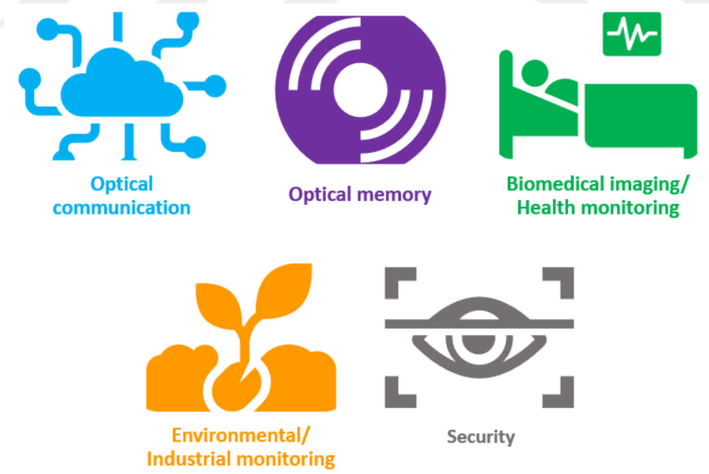

Figure 1.1 : The application areas of phototransistor-based sensor devices.

[1]This chapter is based on the following publication: **Tavasli, A.,** Gurunlu, B., Gunturkun, D., Isci, R., Faraji, S. (2022). A review on solution-processed organic phototransistors and their recent developments, *Electronics*, ***11***(3), 316.

The most well-known examples of PTs are based on Si from the IV group and GaAs, and InGaAs from the III – V group. The working wavelength range of the phototransistors differs depending on the semiconductor type. Generally, Si is used for the visible (Vis) to near-infrared (NIR) range, while InGaAs is used in the NIR region. Each region in the spectrum has various application areas related to their wavelength and the semiconductor bandgap. UV-sensitive photodetectors are designed to be utilized in sensor-required areas such as communication, security and biomedical fields. In the NIR and infrared (IR) range, biomedical and artificial vision are probed [11–14]. However, Si-based PTs are insufficient to be used in NIR [2]. In addition, these traditional inorganic semiconductors are not promising materials for wearable, flexible phototransistors in home-assisted or clinical sensor applications due to their rigid structure, and their high-cost production conditions are not suitable for cost-effective, high throughput technologies [4,6,15,16]. Organic materials, including polymers and small molecules, are the most common types and have given new opportunities to overcome the drawbacks [17–19].

Organic semiconductors (OSC) have shed light on mechanically flexible, soft, low-power, low-cost, non-invasive light optoelectronic devices for industrial and clinical implementations. Thanks to their tunable molecular structure, the bandgap of the organic semiconductor can be tailored according to the targeted application. The bandgap and the functionality of OSCs can be adjusted to enhance efficiency in the corresponding area of interest [3,7,19–23]. Due to the easy processing, large-scale production, lightweight structure and solution-processable manufacturing of organic semiconductors, new classes of optical devices have emerged. Two main subcategories of photodetectors are photodiodes and phototransistors. A photodiode is commonly a two-terminal device with a vertical structure in which the OSC layer is sandwiched between electrodes with an ohmic contact. Charge carriers are circulated until recombination occurs between symmetrical electrodes. As a result, photodiodes have > 100 % photoconductive gain and high responsivity. However, a phototransistor provides high sensitivity and low noise levels and shows high detectivity compared to photodiodes. It can be explained by the design of a transistor. The gate electrode plays a crucial role in modulating current and lowering noise. In addition, a phototransistor combines signal amplification and light detection in a single device. Hence, it can be integrated easily into devices and circuits. The active material can take the light directly without the shielding of electrodes [2,3,12,18].

Organic phototransistors (OPTs) are optically controllable devices based on organic field-effect transistors (OFETs) [1,6,18,21,24–26]. OFETs play a crucial role in optoelectronic research due to their organic active layer, three-electrode device structure, signal amplifying properties, low noise medium and low voltage operation depending on the dielectric type. OSCs intrinsically provide efficient light absorption properties, tunable bandgap, and lightweight, low-cost, and easy mass production by solution processing. In general, OSCs are employed in OFETs as a thin film, hence OFET configuration is often referred to as organic thin-film transistor (OTFT) [3,17,27–32].

It should be noted that flexible organic phototransistors have been mainly investigated for light detection in the ultraviolet (UV) – visible range. For instance, a blended polymeric semiconductor layer was examined under the 300 – 800 nm UV – Vis range with higher photocurrent (up to 10^5) achieved from the latter, attributed to the charge carrier trapping effect [33]. Recently, advances in OPTs focus on UV, short-wave IR (SWIR) and near IR detection have risen substantially [19,28,34–36]. Numerous research on NIR sensors is increasingly leading to point-of-care (POC) devices, such as pulse oximetry and blood pressure monitoring [9,15]. Most basic human characteristics can be evaluated by blood flow in the subcutaneous tissue. “Therapeutic window” or “diagnostic window” is considered in the light absorption of the tissue. Biological tissues exhibit low absorbance which explains why the long-wavelength range (600 – 1600 nm) of the NIR and SWIR light detection is particularly used in OPTs for biomedical studies [5,8,15,16,36]. Poly[2,5-(2-octyldodecyl)-3,6-diketopyrrolopyrrole-alt-5,5-(2,5-di(thien-2-yl)thieno [3,2-b]thiophene)] (DPP-DTT) and [6,6]-Phenyl-C61-butyric acid methyl ester (PCBM) are the popular choices OSC materials for NIR optical sensors. DPP-DTT:PCBM solution-based bulk heterojunction (BHJ) is frequently applied as the active layer in OPT studies [9,15,35,37]. In addition, poly(5,7-bis(4-decanyl-2-thienyl)-thieno(3,4-b) diathiazole-thiophene-2,5) (PDD-TT) is also used as NIR-sensing materials [38,39].

Both the field-effect transistor structures and solution-deposition techniques offer superior features and performance. However, some existing drawbacks and challenges in the realisation of fully solution-processed OFET and OPT, from a scientific and engineering perspective, should be contemplated [40]. A device can suffer from poor morphology and/or weak charge carrier mobility of the polymeric semiconductor materials [2,11]. The solution-processed layers can be susceptible to high temperatures or solvents that are used during the subsequent fabrication steps. A mismatch between solution-processed and vacuum-processed materials can cause low fabrication efficiency and reproducibility. Thereby, bottom gate OFET configuration is often preferred to prevent OSC from being damaged by the high temperature of the deposition of the electrode [41]. For instance, flexible substrates such as polyethylene terephthalate (PET) cannot survive the high temperatures required for indium tin oxide (ITO) electrode deposition. Hence, to obtain a high-performance device, compatibility of the deposition processes of electrodes and dielectric layers and/or OSC layers should be investigated. Moreover, the choice of solvents is critical to avoid smearing and dissolution of adjacent layers deposited from the solution. Hence, large-scale production of OFETs and OPTs with high reproducibility and efficiency rates is still a significant challenge. To keep the environmental stability of the organic materials, a suitable encapsulation layer should be applied to the device. It is crucial in terms of the lifetime of sensor devices [12,42]. Uncertainty remains on how to obtain fully solution-processed, flexible and long-term stable OFETs and photodetectors [40]. Extensive work is needed to address the shortcomings in the mass production of commercial products of fully solution-processed electronic and optoelectronic devices for practical applications.

1.1 Organic Semiconductors and Fundamental Principles of OFETs

After the introduction of OSC materials in the 1980s, OFETs have performance levels comparable to their polycrystalline (inorganic) counterparts [43,44]. Section 1.1.1 explains the structure and different types of organic semiconductors, charge carrier generation in the active layer, and their outstanding properties. An OFET device has various device configurations. Some parameters should be considered when designing an OFET device. The working mechanism of the three-electrode device is focused on along with trap limited charge carrier transport and contact resistance in Section 1.1.2. Solution-processing techniques adopted for OFET and OPT fabrication are given in Section 1.1.3.

1.1.1 Organic semiconductors

Organic semiconductors are carbon-based optoelectronic materials with unique solid-state physical properties stemming from the soft, Van der Waals bonding between their molecules [45]. They have enhanced light detection capabilities, ranging from UV to IR. They are used in OFETs, organic photovoltaics (OPVs) and photodetectors due to their fantastic features, such as soft molecular nature, mechanical flexibility, solution-processability, high-throughput, low-cost production, lightweight, absence of rare or toxic elements in their composition and eco-friendly nature [18,46–48]. They are popular choices, extensively explored in established and emerging optoelectronic applications. Additionally, the distinctive ability of OSCs to combine electronic and ionic conduction has positioned them as attractive candidates in organic electrochemical transistors (OECTs) [49], chemical and biological sensors [50] and neuromorphic devices [51].

From the chemistry point of view, organic semiconductors have *sp*^{2} hybridization (Figure 1.2). Sigma bonds are much stronger than pi bonds. The transition of electrons in $\pi - \pi^*$ orbitals requires the lowest energy, and the conduction occurs more easily. Therefore, it is crucial to have *sp*^{2} hybridization to conduct electricity [52–54].

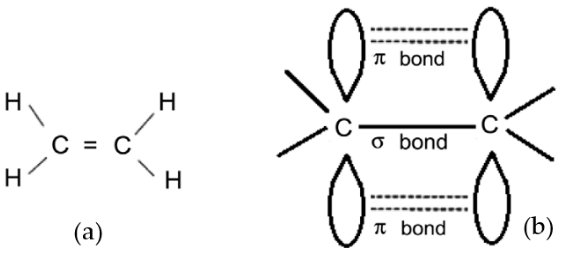

Figure 1.2 : Schematic representation of (a) chemical structure of the ethylene molecule, (b) σ and π bonds in the ethylene molecule. Reprinted from [54]. Copyright (2017), with permission from Elsevier.

In organic semiconductors, charge carriers are called polarons [31]. Polarons are self-localized. Localisation of charge carriers is associated with the hopping transport taking place in organic semiconductors [31,54]. Electrons hop from the highest occupied molecular orbital (HOMO) of the OSC to the lowest unoccupied molecular orbital (LUMO) of p-type semiconductors (and vice versa for n-type OSCs). For common OSCs, the bandgap can be ~ 1 – 4 eV. A small bandgap (E_g) can detect the longer wavelength of light. This opens new ways to benefit from organic semiconductors in optical devices for various applications.

Thanks to their tunable molecular structure, the bandgap of OSC molecules can be adjusted according to the aim of the application [2,11,55]. The efficiency, sensitivity and selectivity of the corresponding devices can be enhanced by tuning the bandgap and functionality of OSCs [3,19–23].

A comparison between organic and inorganic semiconductors along with their corresponding parameters is given in Table 1.1.

Table 1.1 : A comparison of physical and chemical parameters of organic and inorganic semiconductor materials [47,52,56].

Parameter	Organic SC	Inorganic SC
Binding energy	Weak (Van der Waals)	Strong (Covalent, metallic, ionic bonding)
Mechanical resistance	Weak (prone to gases and oxidation)	Strong
Charge carriers	Polarons, excitons (localized)	e^-, h^+, ions (delocalized)
Dielectric constant	≈ 3 – 4	≈ 11
Polarisation	Strong	Weak
Charge transport	Hopping	Band
Exciton	Frenkel	Wannier-Mott
Mobility	~10^{-6} – 1 cm^2 / Vs	~ 1000 cm^2 / Vs
Conductivity	Extrinsic	Intrinsic

Numerous examples of organic single crystals, thin films and nanowires used as the active layer in OPTs and OFETs have been reported in the literature (Figure 1.3) [1,35,57,58].

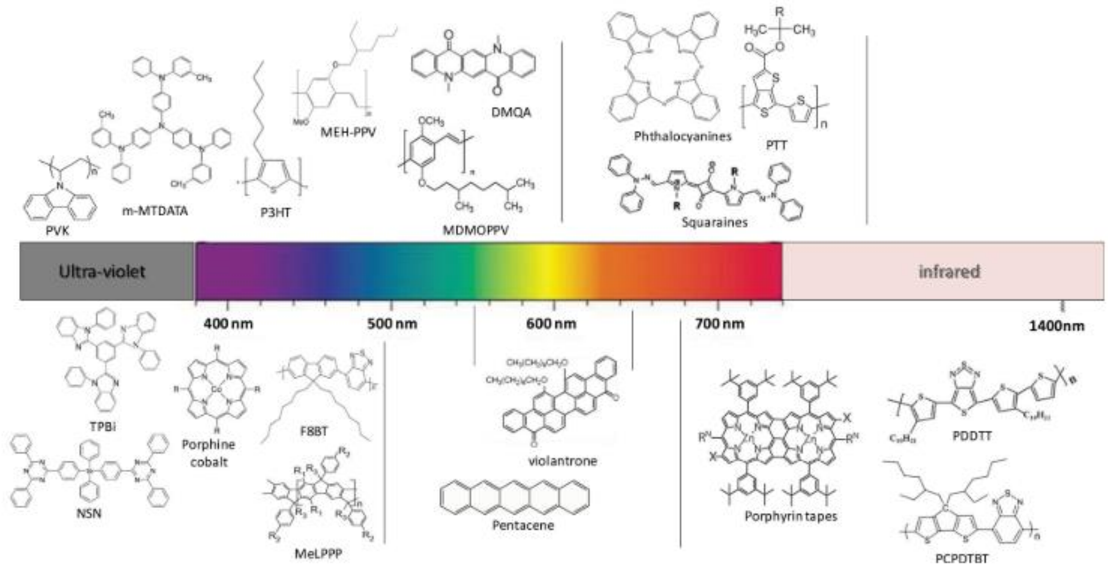

Figure 1.3 : Some examples of OSCs in a broad wavelength range of the spectrum. Reprinted with permission [3]. Copyright 2013, Wiley.

Organic molecules are composed of covalently bonded molecular units and their electron delocalisation ability depends on the intermolecular packing. Some of the intermolecular modes are soft meaning large vibrational amplitudes can occur at room temperature. Electronic and structural dynamics help explain the charge transport and optoelectronic properties in OSCs. The structure – property relation is one of the main aspects that guide scientists to understand the effect of the electronic structure on the charge carrier transport, and it allows the improvement of novel materials for optical device applications [45].

Thin films are key components of today's technological advancements. Their features differ from those of the bulk materials due to the nanostructure form [59]. In recent years, there has been a growing interest in organic dielectric and semiconducting thin films due to their compatibility with a wide range of materials, processing techniques and practical device structures [1,18,60]. As an active layer of an OFET device, polymers, small molecules and blends of these organic structures are the most widely used candidates. Polymer organic phototransistors (PPTs) or small molecule organic phototransistors (SOPTs) take their names from the chemical form of the active layer material [3,18,31,47,48]. These materials can be easily deposited using solution processing techniques [3,18,48]. Polymeric semiconductors exhibit superior solution-processing ability and compatibility with plastic substrates and can be used as pristine or in blends with small molecules in organic phototransistors. PPTs and SOPTs are explained in detail, and examples are given from the literature in Section 1.2.4. Noteworthy is that by the state-of-the-art approaches to the synthesis of organic semiconductors, chemical doping can be controlled, impurities can be eliminated, and high-purity materials can be obtained [7].

1.1.2 Fundamental principles of OFETs

An organic field-effect transistor is a three-electrode device, also called an organic thin-film transistor. Nowadays, sensors developed based on OFETs like chemical sensors for volatile organic compounds (VOCs), NIR-sensitive phototransistors and biosensors based on microfluidic-OFET have been increasing rapidly because of the advantages of OFET devices [22,29,33,61–66]. First and foremost, mechanical flexibility, low processing temperature and chemical functionality are the critical properties of OFET devices. Besides, one of their most important properties is the compatibility with a variety of substrate materials choices. Paper, textile or other biodegradable substrates can be utilized to reduce electronic waste [3,67–70].

An important difference from the other FET-based devices is that OFET works in the accumulation regime [31,71,72]. An OFET device is comprised of three components. One of them is the organic semiconductor which serves as the active layer. The second component is the dielectric layer. It plays an important role in the OFET device due to its capacitor mission. To operate at low voltages, a dielectric layer with a high dielectric constant (so-called high-*k*) is essential [73,74]. The last component is the metal electrodes, which are gate (G), source (S) and drain (D). There are different device configurations depending on the position of electrodes [66,75] that are given in Figure 1.4. There are four configurations based on the position of the electrodes. They are the bottom gate – top contact (BGTC), bottom gate – bottom contact (BGBC), top gate – bottom contact (TGBC) and top gate – top contact (TGTC). Each configuration has its pros and cons.

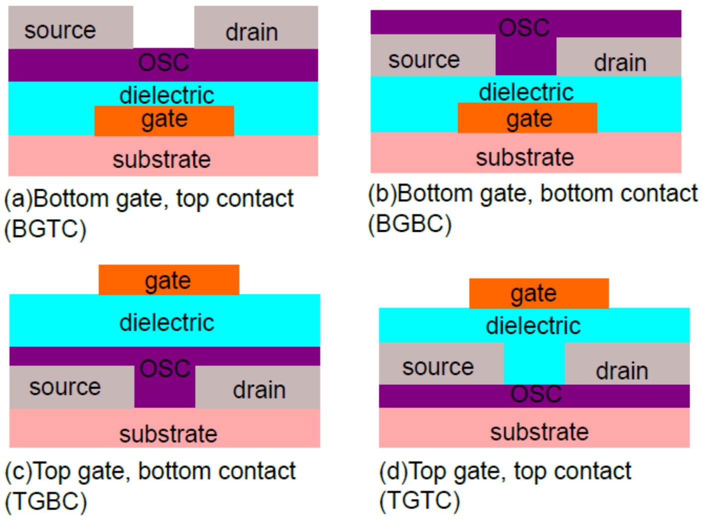

Figure 1.4 : Different geometrical configurations of an OFET; (a) bottom gate – top contact, (b) bottom gate – bottom contact, (c) top gate – bottom contact, (d) top gate – top contact.

The dielectric layer behaves like a capacitor between gate and source – drain electrodes. Charge carriers are stopped by the insulator layer, then they begin to accumulate [20,54,63]. That is why the OFET is working in the accumulation regime. The channel conductivity is modulated through the gate electrode. The role of the source and drain electrodes is to inject and withdraw charge carriers, respectively. When no gate voltage ($V_G = 0$) is applied to the gate electrode, very low current flows in the channel, so-called the off state. After applying a gate voltage, the charge carriers accumulate at the interface of the semiconductor/dielectric and a conductive active channel forms between source and drain. The sheet of mobile charge carriers at the interface leads to a higher current, which means the device is in the on state. It is necessary to elucidate that the on–off state of an OFET device is related to the threshold voltage position [47,54,63].

The current – voltage (I – V) output and transfer characteristics of a typical OFET are illustrated in Figure 1.5. Figure 1.5c shows the linear dependence of the square root of the drain with the gate voltage [7].

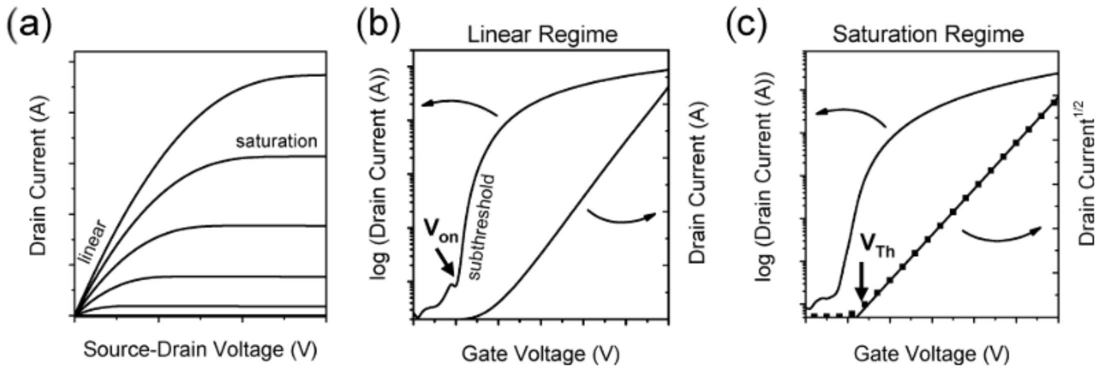

Figure 1.5 : A representative current-voltage characteristics; (a) output curve, (b) transfer curve in linear regime, and (c) saturation regime. Reprinted with permission from [7]. Copyright 2007 American Chemical Society.

An output curve demonstrates the drain current (I_{DS}) versus source-drain voltage (V_{DS}) at a constant gate voltage value. A transfer curve represents the drain current versus gate voltage at a constant V_{DS}. The onset voltage can be extracted from the semi-log plot (a quick step up of drain current above a defined low off-current) (Figure 1.5b). The subthreshold swing (S) is a change in V_G required to increase the I_{DS} by one order of magnitude in the $V_0 \leq V_G \leq V_{th}$. S depends on the gate dielectric capacitance and trap states. For an ideal OFET, a small S is highly desirable, and it describes the switching speed of the transistor. The number of trap states is equal to zero in an ideal device; thus, the theoretical minimum value of S is calculated at room temperature as 59.5 mV decade^{-1} [28]. S can be expressed as using equation (1.1):

$$S = dV_G / d(\log I_{DS}) \tag{1.1}$$

The slope of the drain current vs. gate voltage in the subthreshold region is defined as the subthreshold slope (SS = 1/S).

OFET has three modes that depend on the gate voltage and drain voltage; linear mode, saturation mode and cut-off (pinch-off mode) region, respectively (Figure 1.6).

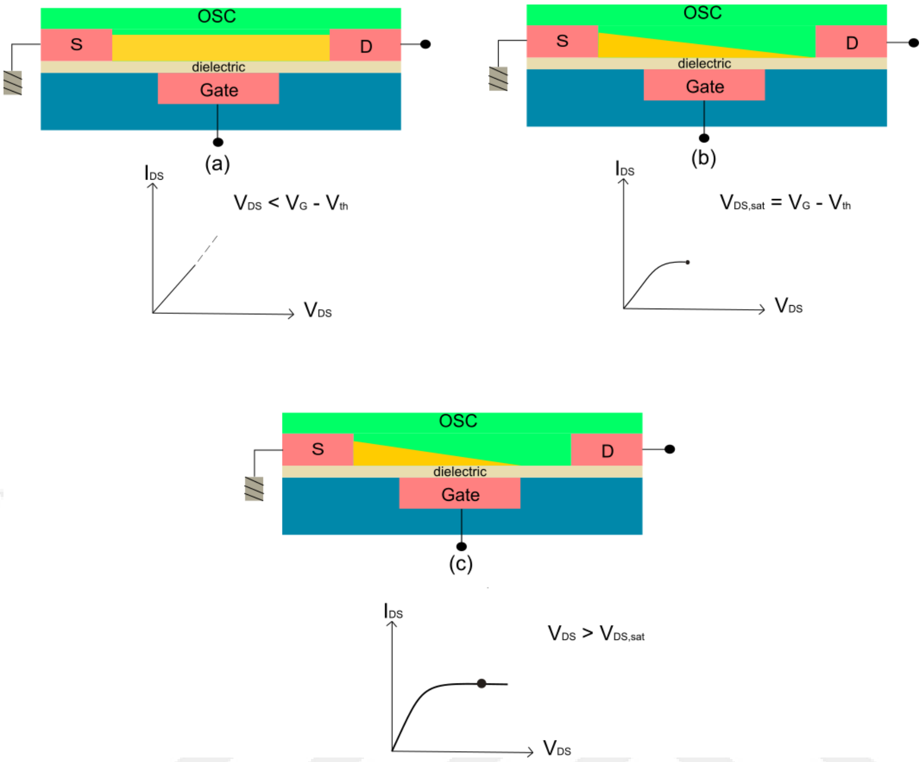

Figure 1.6 : Illustrations of operating modes of OFETs, (a) linear regime, (b) start of saturation regime, (c) the channel pinch-off and saturation regime.

When V_G is applied, while V_{DS} is zero charges are induced at the insulator/semiconductor interface uniformly. When a small V_{DS} is applied, charge carriers begin to move from source to drain through the active channel [29,30,47,63]. As seen in Figure 1.6, as the V_{DS} value increases, the mode changes and goes to the saturation regime. I_{DS} in linear and saturation regimes are shown by equations (1.2) and (1.3), respectively:

In the linear regime:

$$I_D = \frac{W}{L} C_i \mu \left(V_G - V_{th} - \frac{V_D}{2}\right) V_D, \quad V_D < V_G - V_{th} \tag{1.2}$$

In the saturation regime:

$$I_D = \frac{W}{2L} C_i \mu_{sat} (V_G - V_{th})^2, \quad V_D \geq V_G - V_{th} \tag{1.3}$$

where W is the channel width, L is the channel length, C_i is the areal capacitance of the dielectric, μ is the charge carrier mobility, V_G is the gate voltage and V_{th} is the threshold voltage.

The value of C_i is calculated using equation (1.4):

$$C_i = \frac{\varepsilon_r \varepsilon_0 A}{d} \qquad (1.4)$$

where ε_r is the relative permittivity of the material (i.e. the material's dielectric constant, k), ε_0 (8.854×10^{-12} Fm^{-1}) is the permittivity of free space (vacuum), A is the area of the capacitor plates, and d is the thickness of the dielectric layer. At an applied gate voltage higher than the V_{th}, the charge carriers (Q) in the channel start to accumulate (equation (1.5)) with respect to C_i and V_G.

$$Q = C_i (V_G - V_{th}) \qquad (1.5)$$

A larger capacitance value is required to lower the operating voltage. A high capacitance value allows the accumulation of more charge carriers at applied low voltage. Some strategies exist to increase the C_i (equations 1.4 and 1.5). One of the solutions is to use high-*k* (ε_r) dielectric materials to induce more charge carriers [28,76,77]. Another way is to decrease the dielectric thickness ($\sim d < 20$ nm). It should be noted that the dielectric thickness needs to be significantly thinner than the channel length ($L > 10\ d_{dielectric}$) to ensure that the gate voltage modulates the charge carriers in the channel [7,32]. Conventional studies use silicon dioxide (SiO_2) as both an insulator layer and a substrate on account of its smooth structure and availability. Other frequently chosen materials are metal oxides such as aluminium oxide (Al_2O_3, $k \approx 8$) and tantalum oxide (Ta_2O_5, $k \approx 23$). Meanwhile, low-*k* polymeric insulator materials such as polymethylmethacrylate (PMMA, $k \approx 3.5$), polyvinyl alcohol (PVA, $k \approx 7.8$) and poly(4-vinyl phenol) (PVP) have been utilized, as well. They are solution-processable and can be deposited on top or bottom depending on the device configuration. It is known from the literature that after dissolving in an orthogonal solvent, they can be coated on top of the OSC, and do not damage the OSC. Cellulose is also preferred as a natural high-*k* insulator material. Pure cellulose has a relatively higher *k* constant ($k \approx 6 - 8$) than other solution-processed polymers. Dry cellulose has air in its voids hence its *k* decreases to 1.5 – 4. To hinder this, fillers such as oil, resin, and inorganic particles are utilized [67]. Cyanoethyl cellulose (CEC) and CEC-based nanocomposite (NC) (using nanoparticles of barium strontium titanate (BST, $k \approx 16$)) dielectrics with PVP capping thin-films demonstrated have shown promises for low voltage, low power electronics [78]. Moreover, self-assembled monolayers (SAMs) came out as a modifying component that increases the capacitance by decreasing the thickness to a few nanometers. Hybrid dielectric materials have emerged to solve the problem of low-*k* values of polymers and high-deposition temperatures of inorganic materials. Hybrid materials combine organic materials with inorganic ones. Thus, they benefit from the easy deposition of organic materials and the flexibility and high capacitance of the inorganic ones. Researchers have shown a growing interest in polymer-ceramic dielectrics. Polymeric-nanoparticle (NP) dielectric composites date back to 1988. Polystyrene (PS) and the nanocomposition of titanium oxide (TiO_2) composite was one of the attempted high-*k* dielectric materials. BST and barium zirconate (BZ, $k \approx 11$) NPs are used with high-*k* fluorinated polymers such as poly(vinylidene fluoride-co-hexafluoropropylene) (PVDF-HFP) to make use of their superior features. In these studies, NPs agglomeration can be a complication in obtaining homogenous nanocomposite suspensions. A careful combination of organic solvents and NP-to-polymer volume ratio can be sufficient to rule out any required surface modification [79]. Inorganic – organic bilayer is another way to make a hybrid dielectric, for instance, PMMA/Ta_2O_5 [76]. Chen et al. reported the development of [77] low-power OFETs with a solution-processable nanocomposite of PVP and calcium titanate nanoparticles ($CaTiO_3$ NPs, $k \approx 150$) as the gate dielectric. For a p-type OFET, high-work function metals, such as gold (Au), and platinum (Pt) are chosen as the S / D electrodes. P-type OFET devices operate under a negative voltage (and vice versa for n-type devices) [31,32,46,71]. The larger the applied negative gate voltage is, the higher the induced holes appear in the conducting channel. By applying a negative drain voltage, holes begin to move to the drain electrode [47,71,80]. This is related to the HOMO – LUMO level of the semiconductor and the work function of the metal electrode [7,47,71]. Transition metal oxide (TMO)-based buffer layers, such as molybdenum trioxide (MoO_3), vanadium oxide (V_2O_5), and tungsten trioxide (WO_3) are generally deployed to decrease the hole injection barrier [81].

Trap states (Figure 1.7) exist in the HOMO – LUMO gap [82]. Once deep levels of traps are filled, charge carriers can transport through the channel by applying a V_{DS} bias. Traps can increase photosensitivity and the response time. For instance, in a p-type device, as more holes are trapped in the OSC, more electrons stay in the active channel due to charge neutrality.

So, the conductivity is increased. The insulator – semiconductor interface is defined as a high-trap density region [28,31,32,71,83]. This topic is elucidated in more detail in Section 1.2.2.

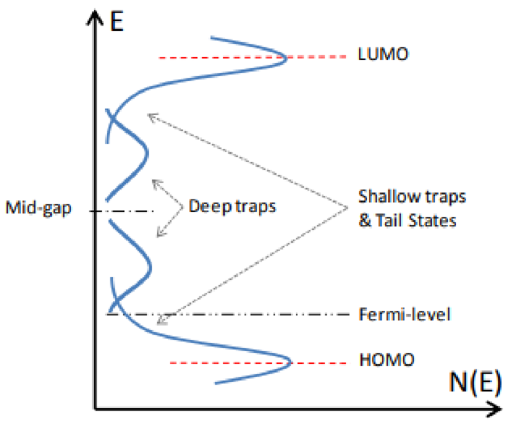

Figure 1.7 : A presentation of the trap states between HOMO and LUMO. Reprinted from [82]. Copyright 2013, with permission from Royal Society of Chemistry.

The final characteristic we discuss here is the contact resistance (R_C) of OFETs. It is the total resistance of source and drain contacts. Due to the injection of charge carriers from metals, they must pass a barrier. That is why it is called contact resistance [32,47]. One of them is channel resistance ($R_{channel}$). The drain current – gate voltage (transfer) curve is not a straight line because of contact resistance. Access resistance is another resistance that exists in OFET structures. The travelling of charge carriers from the source into the channel and back up to the drain causes access resistance. It is also known as bulk resistance (R_{bulk}). In BGBC structures, electrodes are in the same plane as the OFET channel; hence, access resistance is not an issue in that case. Charge carriers can be directly injected into the active channel layer at the insulator/semiconductor interface. In TC structure, the main source of the contact resistance is the access resistance. Charge carriers must travel through a few nanometers to arrive at the channel. Access resistance can be negligible when using polycrystalline films due to their rough surface [84]. When adopting TGBC and BGTC configurations, charges can be injected from both the edge of the source electrode and the overlap region with the gate electrode [7]. Much research has been focusing on lowering the contact resistance by applying various methods, such as preferring TC over BG configurations due to poor semiconductor morphology in the latter. Apart from that, the surface quality of semiconductors can be improved by some chemical modifications. Thiol-terminated (R-SH) hydrocarbon molecules are frequently applied to form a SAM layer on the metal contacts to mask it from the semiconductor [85].

1.1.3 Solution processing techniques for OSC deposition

The solution processing method is a promising deposition technique for fast, cost-effective, high-throughput fabrication of electronic devices on flexible/conformal substrates. It is highly compatible with most organic semiconductors and polymeric dielectric materials. The ease of fabrication and real-time control of parameters due to the low (room) temperature process make such deposition techniques attractive for OFETs and OPT devices. Examples of widely adopted solution-processing techniques are spin coating, drop casting, dip coating, spray coating, blade coating (or roll-to-roll method), gravure and inkjet printing. Nowadays, inkjet printing is widely used because it offers superior advantages over frequently preferred spin-coating. Inkjet printing is a rapid method with low material consumption, printing ability of arbitrary patterns, and high resolution [86,87]. Inkjet printing does not require direct contact with the substrates which in return reduces the risk of defects induced by contact with mechanical parts. By adopting inkjet printing, direct deposition of a controlled volume of functional materials is made possible via a material-efficient approach [88]. Fully inkjet-printed OFET prototypes are successfully attempted [89]. Nevertheless, inkjet printing is intrinsically slower than some other high-throughput printing methods, such as gravure. Parallelization (multi-nozzle) strategies are introduced to minimize such shortcomings [90]. The conventional channel length of an inkjet-printed pattern is normally limited to about 10 μm. By using electric fields to produce the formation of a droplet (electrohydrodynamic jet printing), materials can be patterned down to a resolution of 1 μm [91]. Smaller channel lengths can be achieved through techniques integrating printing with a self-assembly-driven process, such as self-aligned printing, in which the surface energy of a pre-printed pattern is modified with SAMs or surfactants [92].

Not all, but the majority of the polymeric OSCs can be deposited by solution processing. Polymeric OSCs have better solution-processability than small molecules. Blends of polymers and small molecules were prepared to facilitate easier and scalable solution deposition [93]. The solution process can allow unique aspects for controlling molecular packing in OSC material [3,18,20,26,66,75]. Creating a highly ordered and uniform surface is critical for efficient charge carrier transport and high-performance devices. However, it is not always possible to obtain highly aligned organic crystalline arrays due to challenges in controlling crystallographic orientation. OSCs can be distracted due to their fragility by high temperature, UV light, or organic solvents. That means any subsequent photolithography techniques can impair the solution-processed layer underneath [94,95]. Most recently, a solution shearing technique was used to successfully print water-soluble ink on the hydrophobic surface of an OFET device [94]. The solution shearing technique was chosen due to its simplicity and reformative feature on the molecular motifs [94,96]. In addition, this technique was combined with the screen-printing method, which is an inviting technique for high-quality industrial production. The fluid drying dynamics changed with the water-soluble surfactants which had been added to reduce the surface tension between OSC and resist. And they obtained highly aligned organic crystalline arrays as a result.

1.2 Organic Phototransistors

Organic phototransistors are a subcategory of organic light detectors that share the same three-terminal stack structure of an OFET. OFETs can be light-receiving or light-emitting. OPTs are light-receiving OFETs (LR-OFETs) [6,28]. In Figure 1.8, a typical OPT device structure is depicted. Depending on the direction of the light, the device configuration can be named bottom-light (BL) or top-light (TL).

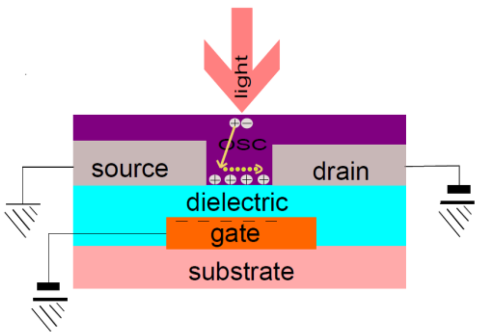

Figure 1.8 : A typical P-type OPT device structure (TL). During illumination, positive charges drift towards the channel.

Organic semiconductors generally serve as the active layer in OFETs and OPTs. They have a wide wavelength absorption range that absorbs light from UV to NIR. The absorbed light excites the energy states of molecules to produce excitons or to induce molecular conformational changes.

OPTs convert the light signals into electrical signals effectively and then amplify the signal thanks to their transistor structure. Thus, they provide both high sensitivity and low noise levels. With the detection capability of weak signals and the possibility of tuning the dielectric properties, organic phototransistors are excellent candidates for low-power operation applications [1–3,12,18,26,28,97]. OPTs have been used for decades in various fields, such as biomedical, energy and environmental studies [1,2,9,12,98,99].

1.2.1 Working modes of OPTs

1.2.1.1 Photovoltaic mode

In photovoltaic mode, the device operates in the accumulation region. When the device is in a turn-on state, for a p-channel device, the gate voltage is smaller than the threshold voltage ($V_G < V_{th}$). After illumination, a positive shift in V_{th} emerges. The semiconductor / dielectric interface can also trap electrons due to electron-capturing trap sites, such as hydroxyl groups [3,18,28,83,100]. Equation (1.6) [100] shows the photocurrent caused by the photovoltaic effect.

$$I_{ph,pv} = g_m \, \Delta V_{th} = \frac{Ak\mathrm{T}}{q} \ln\left(1 + \frac{\eta q \lambda P_{opt}}{I_{pd}\, hc}\right) \tag{1.6}$$

where g_m is the transconductance, A is the proportional factory, k is the Boltzmann constant, T is the temperature, q is the unit charge, η represents the photogeneration quantum efficiency, hc/λ is the photon energy, P_{opt} optical power density, and I_{pd} is the dark current for minority charges [75].

1.2.1.2 Photoconductive mode

In photoconductive mode, the device is in a turn-off state. In this mode, an OPT operates in the depletion region. For a p-channel device, the gate voltage exceeds the threshold voltage ($V_G > V_{th}$). Drain current (I_{DS}) shows a linear increase with optical power [3,18]. I_{ph} is proportional to the areal power density of the incident light [97]. The relationship between optical power density and photocurrent is given in equation (1.7).

$$I_{ph,pc} = (q\mu_p pE)WD = BP_{opt} \tag{1.7}$$

where μ_p is the mobility of charge carriers, p is the charge concentration, E is the electric field, W is the gate width, D is the depth of absorption region, and B is the proportional factory [3].

1.2.2 Performance parameters of OPTs

The performance of phototransistors is evaluated by different parameters. The two most important parameters are photocurrent and dark current. Photocurrent (I_{ph}) is the current that flows when the device is illuminated. Dark current (I_{dark}) is the current that flows in the absence of illumination in the channel. The p-type device has a large negative V_{th} in the dark current. When V_G is near zero voltage, the dark current is very low. To reduce dark current, one or a few monolayers of OSC are suggested [28]. As aforementioned, the on/off current ratio is determined by the position of the V_{th}. In general, a ratio > 10^6 is desirable. A low I_{off} is essential for low power consumption.

The ratio of the photocurrent to the incident optical power (P_{opt}) is referred to as the photoresponsivity (R) of an OPT device. The other two important parameters of a phototransistor device are photosensitivity (P) and detectivity (D*). The value of R depends on the dimensions of the OPT [28]. Table 1.2 comprehensively presents figures of merit of OPT devices.

Table 1.2 : Phototransistor merits of performance [5,11,26].

Figures of merit	Definition	Unit
Photoresponsivity (R)	$(I_{light} - I_{dark}) / P_{opt}$ [2]	AW^{-1}
Photosensitivity (P)	$(I_{light} - I_{dark}) / I_{dark}$	unitless
Detectivity (D*)	The minimum input optical signal to generate photocurrent. $D^* = (A\Delta f)^{1/2}R/S_n$ [3]	1 Jones = 1 $cmHz^{1/2}W^{-1}$
Linear Dynamic Range (LDR)	Range of incident optical powers for which the detector responds linearly [4]	$LDR = 10\log(P_{sat}/NEP)$
External Quantum Efficiency (EQE)	The ratio between the numbers of collected carriers and incident photon	EQE = hc / λq %

[2] $P_{opt} = P_{inc}S$, P_{inc} is the light intensity, and S is the channel area.

[3] A is the effective device area, Δf is the electrical bandwidth of the noise, and S_n is the noise density of the current.

[4] P_{sat} is the saturation signal power, and dB is decibel.

Table 1.2 (continued) : Phototransistor merits of performance [5,11,26].

Figures of merit	Definition	Unit
Noise Equivalent Power (NEP)	S_n / R	$WH^{(-1/2)}$
Noise Density (S_n)	It has multiple components, including thermal noise, which is significant in narrow band gap, shot noise and 1/f noise.	A / $Hz^{1/2}$
Photoconductive Gain (G)	Number of collected carriers divided by the number of photons absorbed.	$G = \tau_{lifetime}\tau_{drift}^{-1}$ unitless

The spectral detection range is another figure of merit in OPTs. For narrow-band applications, e.g., pulse oximetry, a specific spectral detection range is necessary. Low noise (NEP), high speed, high sensitivity and detectivity and selective spectral range are all favourable performance merits for OPT applications. Various studies have been dedicated to improving the electrical performance of OPTs. For instance, the relationship between inorganic nanoparticle density and photosensitivity was studied by Mok et al. [101]. They reported that since light absorbance of TiO_2 nanoparticles to white light is negligible, the photosensitive behaviour of the device could be attributed to light absorption of the Poly(3-hexylthiophene-2,5-diyl) (P3HT), which generated excitons in the composite film. However, the separation of charge carriers occurs at the interface of P3HT/TiO_2. For the higher density of TiO_2 nanoparticles, a larger interface area existed in the composite film. Therefore, more electrons could be trapped in the TiO_2 nanoparticles which correspondingly induced higher photosensitivity of the device. Liu et al. focused on low voltage OPTs and tuning of their electrical and photosensitive properties [102]. PVP and PMMA were used as modification layers that could block the electron injection because their LUMO levels were higher than that of the OSC (Figure 1.9a,b and c). When ΔVth values were evaluated, it was clear that the highest shift belonged to the unmodified one (unmodified ΔVth = 14 V, PVP-modified ΔVth = 7.6 V, PMMA-modified ΔVth = 5.8 V). Similar to these results, the R-value of PMMA-modified OPT was the lowest of them all ($R_{max,PMMA}$=223 mAW^{-1}, $R_{max,PVP}$=303 mAW^{-1} and $R_{max,unmodified}$= 761 mAW^{-1}). Moreover, Park et al. surveyed hybrid gate insulators (PVP – PMMA) on UV-sensing by comparing them to the conventional single-layered dielectric (PMMA) [103]. PVP was chosen due to its high sensitivity to UV light and its insulating capability. In their hybrid design, PMMA was combined with PVP due to its no-trap structure. Therefore, the new design could enhance optical switching. The reported solution-processed hybrid gate insulator–OPT had 1.29 times higher photoresponse than that of the conventional single-layered dielectric. After illumination, holes were extracted at the drain electrode, while electrons went to the gate (Figure 1.9f and g). During the UV exposure, the hybrid gate insulator – OPT device showed better performance (Figure 1.9d and e) (Currents for single-PMMA = 7.98 x10^{-11} A and hybrid-PVP/PMMA =1.17 x10^{-10} A).

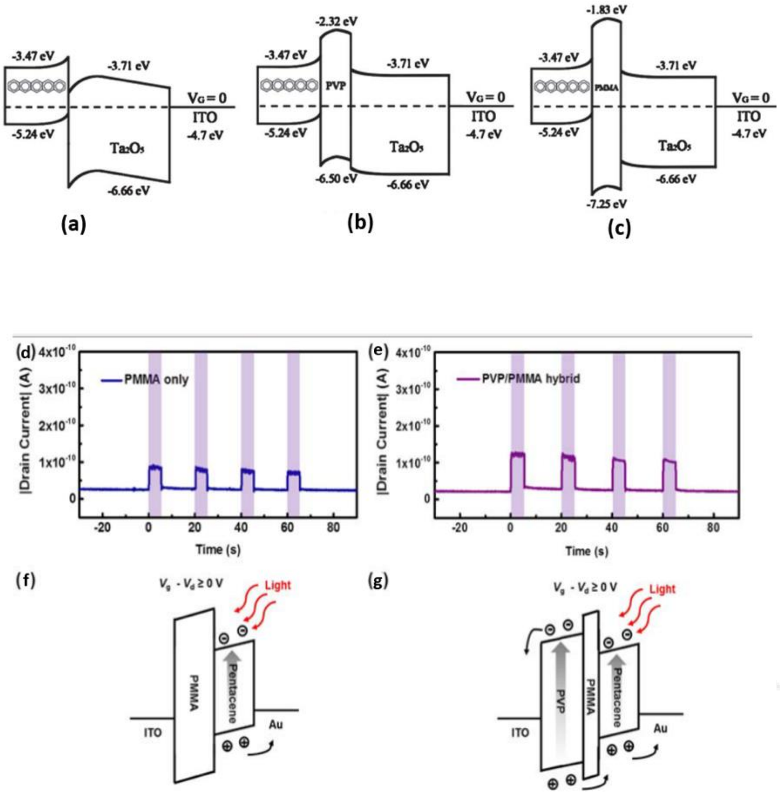

Figure 1.9 : (a), (b) and (c) indicate the energy band diagrams of unmodified, PVP-modified and PMMA-modified OPT memory in darkness. (d) and (e) illustrate dynamic photoresponsive behaviour of OPTs (PMMA and PVP/PMMA gate insulator), (f) and (g) show the operation. Reprinted from [102], [103]. Copyright 2012, with permission from Royal Society of Chemistry.

Park et al. also investigated bulk-effect photoresponsive gate insulators in OPTs [25]. They compared two different thicknesses of the PVP dielectric layer. It is a well-known fact that the greater the dielectric thickness is, the smaller the dielectric capacitance becomes. However, in their study, it was found that the thicker (d = 260 nm) PVP layer showed higher P and R values (for thin (d = 60 nm) dielectric, P = 6.14 x10^{1}, R = 0.95 AW^{-1}; for thick dielectric P =1.38x10^{3}, R =1.28 AW^{-1}). They attributed this behaviour to the absorption of more photons. For wearable devices, physically flexible and robust sensors are important performance parameters which should be complied with to obtain better results from wearers. If we are to design a wearable sensor, it should maintain its performance during and after stretching. Therefore, the mechanical parameters of organic phototransistors should be evaluated [6]. The durability and stability of wearable phototransistors are crucial performance parameters to facilitate them as suitable candidates for clinical applications. Encapsulating the active layer can be adapted to act as a barrier to air and humidity. Xu et al. used poly(tetrafluoroethylene) (PTFE)/Parylene as an encapsulation layer to make their phototransistors robust in terms of mechanical flexibility and air stability [15]. They reported that their devices exhibited good performance against the diffusion of oxygen and water molecules.

1.2.3 Charge photogeneration and separation in OPTs

Organic phototransistors convert the light into a flux of charge carriers. In the active layer, photogenerated excitons (e^{-}/h^{+} pairs) of high binding energy are created. A bulk-heterojunction structure formed by two materials is exploited to enhance the photogeneration, separation and collection in OPTs. As a result, an effective trapping of charge carriers in one component and the transport of the opposite charge carriers in another component occurs at the same time. Therefore, donor (D) and acceptor (A) layers are preferred for the photoinduced charge separation [3,53,80,104].

BHJ structures involving a narrow bandgap polymer and an acceptor effectively achieve the charge separation of excitons [9,23,105]. Herrera et al. studied the relationship between the blending ratio and the device behaviour [104]. P3HT was used as the p-type semiconducting polymer and PCBM was selected as the n-type small molecule. The OPTs were illuminated by green light (λ=525 nm) to detect the contribution of P3HT to charge carrier generation. Due to their high photoresponse, the authors suggested these BHJs as promising candidates for future studies. On the contrary, they pointed out that blending P3HT at ratios from 1 % to 20 % did not have a significant effect on charge dissociation. DPP-DTT and PCBM were used as BHJ in another study [9]. The devices denoted high responsivity (~ $5x10^{5}$ AW^{-1}). Hybrid transistor design gains attention in flexible electronics due to its attractive features, such as the solution processibility and transparency of photosensitizer molecules. In such a hybrid design, a photosensitizer molecule is applied to OPT to enhance the sensing range by separating charge absorption and charge transport. Conformational changes occur during exposure to UV and Vis light and cause some reversible variations in physical properties, colour, polarity, energy levels and π-conjugation

[1,28,106,107]. These molecules can be incorporated into OPT devices in the following three different ways [1]:

- Interface / surface engineering
- Doping in the channel / dielectric
- Direct use at the channel layer

Utilizing photosensitive molecules at the insulator/semiconductor interface is an effective method to modify device performance by controlling trap densities at the interface. Spiropyran (SP), spirooxazine (SPOx), diarylethene (DAE) and azobenzene (AZO) are the most widely studied photochromic molecules. These molecules have two switchable states. With illumination, several reversible processes take place. One is the non-ionic – ionic isomerisation which happens in SP molecules. The isomerisation of SP results in dipole moment changes which leads to a change in the dielectric constant (and capacitance) value. The other is the open-closed ring isomerisation in DAE molecules. And the last isomerisation type is cis – trans isomerization in AZO molecules [107,108]. Shen et al. used SP molecules in the gate dielectric layer in OTFTs [109]. They blended SP with PMMA to form a hybrid gate dielectric layer in BGTC configuration and deposited it using spin-coating. PMMA served as a good matrix to allow the isomerisation. With UV light, ring-opening occurred (Figure 1.10), and the dipole moment rose substantially (from 6.4 D to 13.9 D). It affected the dielectric constant (3.67, ~ 28 % larger than the closed case). Taking advantage of the more charge carrier capacity of the capacitance, an increase in the drain current was observed.

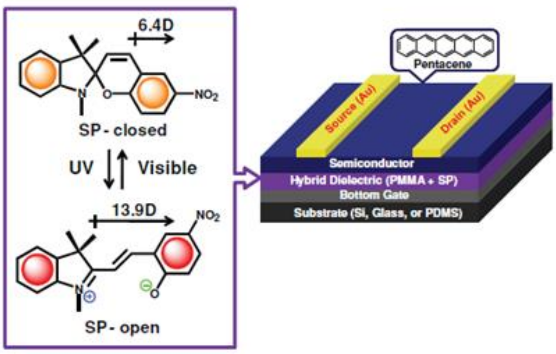

Figure 1.10 : Reversible isomerisation reaction and device structure. Reprinted with permission [109]. Copyright 2010 Wiley.

Kang et al. showed a dual-functional device (BGTC) capable of working both as a memory transistor and a phototransistor [110]. The motivation for the research was the necessity of multifunctional storage for the next generation of emerging technologies. They blended the spironaphthooxazine molecule with PMMA and integrated it as an insulator layer by spin-coating. A reversible electronic band structure was observed during the UV and Vis light illumination. By UV illumination, a reversible reaction occurred. The bandgap became narrower (Figure 1.11) which meant the charge-trapping effect increased.

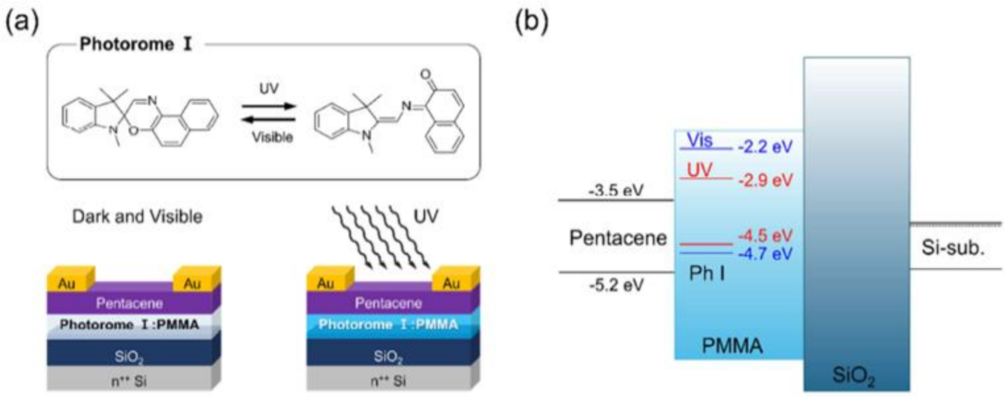

Figure 1.11 : Schematic of (a) device structure and isomerisation process, (b) energy band gap during Vis and UV. Reprinted from [110]. Copyright (2020) with the permission from Elsevier.

The study pointed out that UV light caused a form change from sp^3 to sp^2 hybridization. Conversely, after the exposure of Vis light, double bonds were broken. The device demonstrated a large memory window (~ 56 V) and indicated that their study was promising for organic non-volatile memory. Ishiguro et al. created a new design with a dual gate layer [111]. This new design brought in light field effect and electrical effect together. Optically active SP molecule/poly(triarylamine) (PTAA) mixture and inactive PTAA were applied in the transistor as the top and the bottom channels, respectively. The mixture of SP/PTAA was spin-coated. The open-ring SP had an ionic polarized form and worked as a charge scatter. On the contrary, the closed-ring type did not affect the channel, and the results were similar to the pristine PTAA layer. The optically induced change in the drain current was preserved despite switching off the UV light. It meant that the device had optical memory behaviour. Results were promising for the device to be a convenient candidate for optically and electrically controllable devices. Hayakawa et al. studied the DAE derivative molecule as an active layer in a BGTC design [112]. The photoisomerization caused changes in the energy levels. As a result, the charge carrier injection was affected, since π-conjugation of the molecule offered distinctive charge carrier transport due to differentiation on the π-orbitals overlap. In the open ring position, the work function of the source electrode and HOMO level of the DAE was larger than that of the closed ring type, and this made the charge injection more difficult (Figure 1.12). A reversible change in the drain current was observed by the light illumination. I_{on} / I_{off} current ratio reached nearly 1 x 10^2. They reported that the subthreshold swing value surged from 12 V/dec to 25 V/dec which could be attributed to the traps at the insulator / active layer interface induced by the illumination. The estimated trap density was found 5 x 10^{13} $cm^{-2}eV^{-1}$ after the illumination.

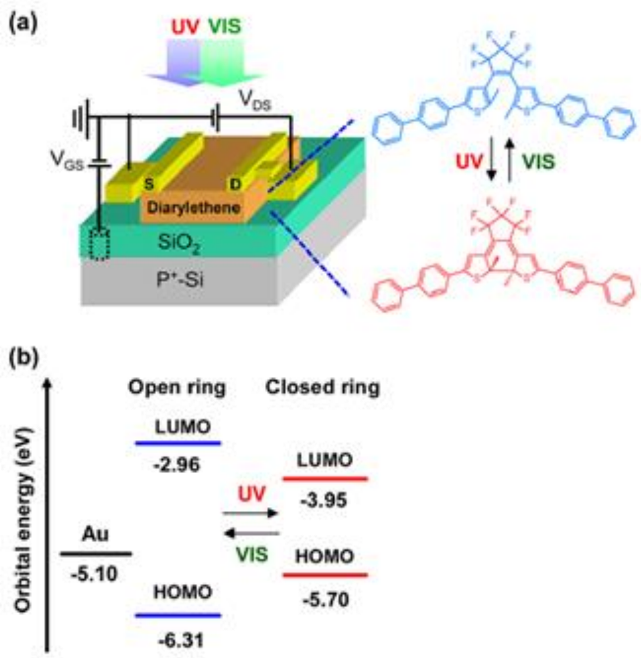

Figure 1.12 : Schematic of (a) device structure and isomerisation process, (b) the corresponding energy levels. Reprinted with permission from [112]. Copyright 2013 American Chemical Society.

1.2.4 OPTs based on solution-processed small molecules, polymers and blends

The solution process is compatible with high-throughput technologies and flexible substrates. Dip coating, spin coating, blade coating, drop-casting, spray coating and ink-printing are some common subcategories of solution processing. Such low (room) temperature processes are widely appealing for the cost-friendly and large-area production of OPT devices. Moreover, it offers unique aspects for controlling molecular packing in OSC materials. Not all but some of the small molecules and polymers can be deposited as an organic semiconductor layer by solution processing techniques.

Solution-processed polymeric phototransistors have shown superior characteristics than their small molecule-based counterparts. PPTs have high charge carrier mobility and wide absorption to facilitate the whole process of effective light absorption, while the $\pi - \pi$ interactions influence the conducting mechanism [3,18,20,66,75]. In Figure 1.13, the chemical structures of some small molecules and polymers used in OPT devices are shown.

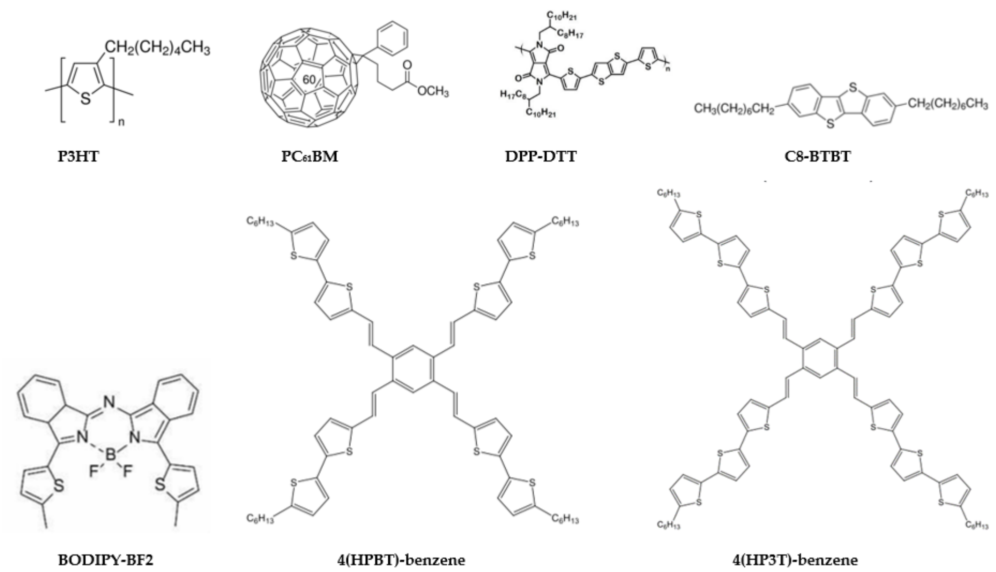

Figure 1.13 : Chemical structures of some solution-processed small molecules and polymers used in OPT devices.

The molecular packing of organic semiconductor molecules and polymers plays a significant role in the charge carrier mobility and output current of the OPT device. Researchers report that regularity, $\pi - \pi$ stacking, and lamellar motif can create outstanding changes in the polymer backbone features. Backbone structure, molecular weight, side chains and processing conditions (including solvents, annealing temperature and choice of substrate) can ultimately impact the transport of charge carriers and the performance of OFETs and OPTs. More efficiently, charge carrier transport takes place when the molecules of a conjugated polymer are in line with the direction of the current. Edge-on orientation stems from the c-axis of the semiconductor backbone. The c-axis is alignment with the substrate. In face-on orientation, the semiconductor backbone is parallel to the substrate. That is why an edge-on rather than a face-on orientation (Figure 1.14) is preferred in OFET and optoelectronic devices.

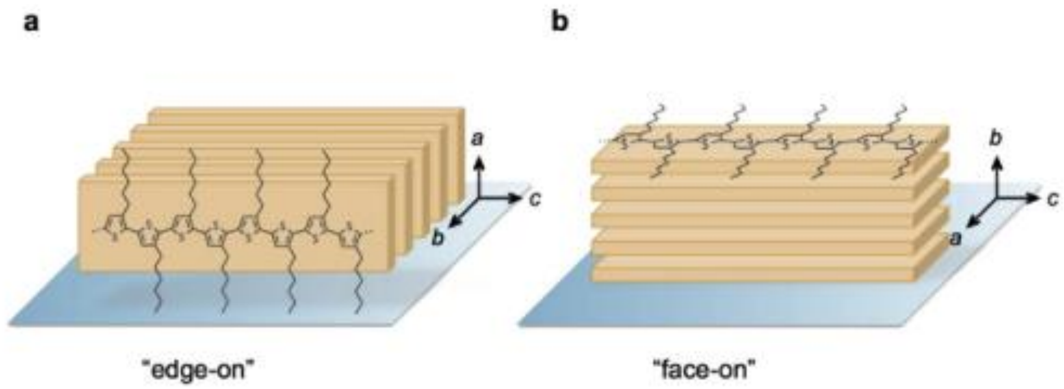

Figure 1.14 : Schematic representation of (a) edge-on and (b) face-on orientations of semiconductor backbone respective to the substrate surface. Reprinted from [113], Copyright (2015) with permission from Elsevier.

Changing molecular motifs can be achieved by introducing polar groups or alkyl groups. For instance, alkyl groups can change the charge orientation from edge-on to face-on [44,113]. Various substituents can be attached to the polymer backbones. Coupling polycondensation is widely used for thiophene-contained conjugated polymers. Apart from that, the fluorination effect is one of the most preferred ways to tune energy levels. The size of fluorine resembles hydrogen and the replacement of hydrogen with fluorine is a convenient method without the steric hindrance effect. Substituent effect and bridging atoms effect are other effective strategies for tailoring energy levels of polymers [114]. In one study, copolymers of 4-thieno[3,2-*b*]thiophen-3-ylbenzonitrile with anthracene (P1) and biphenyl (P2) were synthesised and characterised for optical, electronic and thermal properties [115]. These two novel copolymers promised a huge potential to be used as OSCs in electronic applications due to their low bandgaps (2.01 eV for P1 and 1.9 eV for P2). P1 had a higher HOMO level (E_{HOMO} = –5.74 eV) than P2 (E_{HOMO} = –5.54 eV). This was attributed to the steric hindrance of anthracene. The thermal gravimetric analysis showed that $\pi - \pi$ stacking in the P2 which had biphenyl groups, made the copolymer more stable at high temperatures. P2 copolymer was apt to provide high charge carrier mobility due to its backbone orientation and lower bandgap. Bronstein et al. reported thieno[3,2-*b*]thiophene-diketopyrrolopyrrole-based polymer for OFET and OPVs [116]. They applied thieno[3,2-*b*]thiophene units to modify coplanarity and these units provided more delocalised HOMO distribution. P1 and P2 polymers had similar structures except for a thiophene unit that didn't exist in the P2 polymer. P1 polymer (μ_{hole} = 1.42 ± 0.46 $cm^2(Vs)^{-1}$) exhibited higher hole mobility than P2 polymer (μ_{hole} = 0.037 ±

0.015 $cm^2(Vs)^{-1}$). This was attributed to the existence of disorders or traps. The reduced distance between the solubilising alkyl chains in P2 caused a steric hindrance. Therefore, it contributed to the charge carrier mobility differences between polymers P1 and P2.

Among the solution-processed small molecules, star-shaped oligothiophenes 1,2,4,5-tetra(50-hexyl-[2,20]- bithiophenyl-5-vinyl)-benzene (4(HPBT)-benzene) and 1,2,4,5-tetra(50-hexyl-[2,20]terthiophenyl-5-vinyl)-benzene (4(HP3T)-benzene) are commonly preferred ones [21]. A study reported the use of soluble 4(HPBT)-benzene and 4(HP3T)-benzene to obtain a sensitive OPT device [117]. The photoinduced electrons were trapped in the bulk while the holes were transported in the channel. It was observed a high I_{on} / I_{off} ratio ($4x10^4$) with high sensitivity (R more than 2500 AW^{-1}) and low gate voltage ($V_G = -10$ V) in a short response time (< 1 s). Their unique structure and short-chain length of 4(HPBT) demonstrated they are promising candidates for power-saving applications. P3HT is one of the solution-processible, conjugated polymers frequently used in OPTs. OSCs blended with inorganic nanoparticles have been recently applied as the photosensitive active layer. Organic–inorganic nanocomposites are a promising approach to enhancing the photoresponse of organic phototransistors [118]. Han et al. used nanocomposites to control the threshold voltage and embed gold nanoparticles into the P3HT layer to increase the photoresponse [118]. The device structure was BGBC and SiO_2 was used as the gate dielectric layer. Their previous study showed that Au NPs enhanced the charge carrier mobility [118]. They decided that 0.1 mg mL^{-1} was the optimum doping concentration [119]. The P3HT/Au NPs mixed solution was spin-coated on the substrate. After embedding Au NPs, the hole injection barrier decreased from 0.54 eV to 0.37 eV. The efficient hole extraction increased the mobility and led to a positive shift for V_{th} (from 12 V to 27 V). The p-type polymer and n-type inorganic nanoparticles blend are advantageous in OPTs due to the stronger impact of inorganic materials [120]. In their studies, Nam et al. used a BHJ of P3HT and different weight (wt) % (up to 50 % wt) zinc oxide (ZnO) NPs. ZnO materials are cheap, and their energy band structure is fitted for efficient charge separation with p-type polymers. The active layer solution was spin-coated on the top of the dielectric layer. The values of R_A and R_C (apparent and corrected responsivities, respectively) achieved at $P_{inc} = 0.27$ $\mu W/cm^2$ were 4.7 AW^{-1} and 2.07 AW^{-1} respectively, when 50 wt % of ZnO NP was blended in. In another work, [105] low-bandgap zinc oxynitride (ZnON) was applied to develop a narrow bandgap organic-inorganic hybrid phototransistor. For the BHJ layer, Poly[2,60′-4,8-bis(5-ethylhexylthienyl)benzo[1,2-b;3,4-b]dithiophene-alt-5-dibutyloctyl-3,6-bis (5-bromothiophen-2-yl) pyrrolo[3,4-c]- pyrrole- 1,4-dione] (PBDTT-DPP) and [6,6]-Phenyl-C71-butyric acid methyl ester ($PC_{71}BM$) were used as a light-sensitive active layer. The formation of the NP layer led to the transfer of electrons from the dissociation, while the deep HOMO of ZnO impeded holes. The device had a broad spectrum range from UV to NIR. The reported D* value reached over 10^{12} Jones with 122.3 dB LDR value and $1.7\text{x}10^{2}$ AW^{-1} R-value at 100 $nWcm^{-2}$ light intensity. A summary of other significant works on OPTs in line with the scope of this review is collated in Table 1.3.

Table 1.3 : Solution-processed OPTs with the device performance parameters.

Device type	OSC	Dielectric	μ $(cm^2(Vs)^{-1})$	R (AW^{-1})	Type of radiation	Wavelength (nm)	Ref
BGBC	P3HT:PCBM	SiO_2	-	-	UV-Vis	300 – 1000	[104]
TGBC	DPP-TTT/ TFP:PS	Cyanoresin (high *k*)	0.84	0.091	UV-Vis-NIR	250 – 1000	[121]
BGBC	DPP-DTT:PCBM	SiO_2	0.3	5×10^5	NIR	350 – 1000	[9]
BGBC	DPP-DTT:PCBM	Al_2O_3 / SiO_2	-	3.5×10^5	NIR	810	[15]
BGTC	PODTPPD-BT[5]: P3HT	PMMA	-	388.43	NIR	200 – 1000	[122]
BGTC	BODIPY-BF2[6]	SiO_2	1.13×10^{-1}	1.14×10^4	NIR	600 – 1000	[123]
BGTC	DPP-DTT	SiO_2	-	~ 246	NIR	600 – 1000	[35]

5 Poly[{2,5-bis-(2- octyldodecyl)-3,6-bis-(thien-2-yl)-pyrrolo[3,4-c]pyrrole-1,4-diyl}-co-{2,2′-(2,1,3-benzothiadiazole)- 5,5′-diyl}] is PODTPPD-BT.

6 4,4-difluoro-4-bora-3a,4a-diaza-s-indacene is BODIPY-BF2.

1.2.5 Novel organic semiconductors for photosensing

Today, more sensitive, high-performance polymers are needed in biomedical and information technologies to detect NIR and SWIR light and provide fast response to ensure one of the basic properties of the sensor devices. Advancements in science and technology have enabled the synthesis of new organic semiconductors for photosensing applications. Vella et al. developed a conjugated polymer for use in photodetectors in a broadband infrared region [124]. They aimed to create a narrow bandgap polymer to facilitate SWIR detection. To achieve this goal, they focused on the shell structure. It was reported in this study that if the conjugated polymer structure was based on an open shell, then they could obtain a very narrow bandgap polymer. The newly synthesised polymer was a high-spin ground state with < 0.1 eV optical bandgap. Thiophene substituent allowed the modification of $C_{16}H_{33}$ side chains and made designing a highly ordered organic semiconductor possible. The donor-acceptor conjugated polymer could sense NIR, SWIR light, and even long-wavelength infrared light. This solution-processable conjugated polymer exhibited a high D* value of more than 2.1×10^9 Jones. Lin et al reported a TGBC, hybrid hetero-phototransistors based on metal halide perovskite (MHP) – OSC [125]. The blend of the small molecule 2,7-dioctyl[1]benzothieno[3,2-b][1]benzothiophene (C8-BTBT) and the conjugated polymer indacenodithiophene-benzothiadiazole (C_{16}-IDTBT) was applied as the active layer in the channel. The mixed-cation and mixed-anion perovskite $FA_{0.83}Cs_{0.17}PbI_{2.7}Br_{0.3}$ (FACs, FA=formamidinium) was preferred as the light-absorbing layer. They created two types (type-I and type-II) heterojunctions and examined different gaps between MHP and OSC. Type I showed a straddling gap and it led to minimum recombination probability. The long-lived photocarriers enhanced the photoresponse rather than that of the type-II, staggered gap. Isci et al. [126] synthesised two thieno[3,2-*b*]thiophene (TT)-based molecules, TPE2-TT and TPE3-TT, and dithieno[3,2-*b*;3,2-*d*]thiophene (DTT)-based TPE2-DTT through Suzuki coupling reaction for optoelectronic applications. Thermal gravimetric analysis of TPE3-TT showed that it had stability for high temperatures. It meant this polymer was a suitable material for optical applications. Narrow bandgaps between 2.8 – 2.88 eV were obtained for the synthesised TPE-based molecules. The maximum absorption peaks were observed at 390, 360, and 389 nm for TPE2-TT, TPE3-TT, and TPE2-DTT, respectively. Computational studies were carried out. The HOMO of TPE3-TT was found as localized over TT. Besides, a minor delocalization over phenyl groups attached to TPE2-DTT was seen. These combinations can open new ways for thiophene-based polymers in optical applications. Such new classes of conjugated polymers can be used in high-efficiency, solution-processed optoelectronic devices. Kim et al. believed that making new D-A molecules was required to fabricate a high-quality device [127]. They synthesized a novel ultra-low bandgap (~ 1 eV) copolymers; poly(bicyclic 2,5-diazapentalene) (PDAP) as a strong electron acceptor and chalcogenophene donors (Furan (Fu), Thiophene (Th), or Selenophene (Se)) (Figure 1.15).

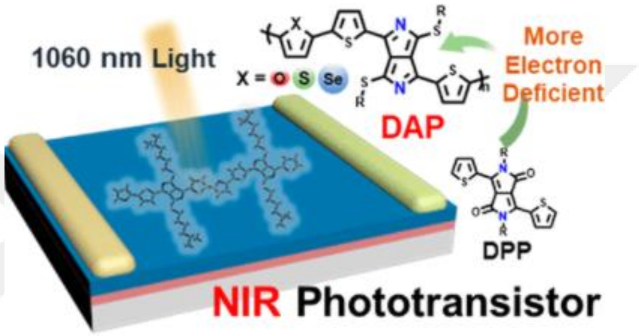

Figure 1.15 : Design of BGTC OPT device and the chemical structure of the active material. Reprinted with permission from [127]. Copyright 2021 American Chemical Society.

Especially, PDAP-Se gave the best combined EQE and D* values (6.56×10^4 % and 1.8×10^{12} Jones, respectively). All copolymers could sense NIR light at 1060 nm, and PDAP-Se showed the highest hole mobility (4.76×10^{-1} $cm^2(Vs)^{-1}$). This BGTC OPT device with a high response and detectivity levels in NIR light (1060 nm) offered a promising result to be a candidate for integrated circuits and optoelectronic devices.

1.3 Applications of OPTs and Photoactivated Memory Devices

OPTs have a wide variety of application areas such as visible light detection, biomedical health monitoring, remote diagnostics, electronic eyes, industrial process inspection, food and water quality control, environmental surveillance, energy, and optical memory. Recent advances in OPTs have been particularly focused on detection in the UV and NIR regions. UV sensors are gaining increasing attention for utilisation in the health and biomedical fields to prevent sunburn and skin cancer caused by sunlight [13,19,28,34–36]. Detection and quantification of the intensity of UV light plays a critical role in medical diagnostics. It has already been known that UV light can harm skin, and overdose exposure can lead to skin cancer. Individuals and children must avoid exposure to UV light without control and/or in the absence of safety measures. On the other hand, UV light is applied for phototherapy to cure skin diseases like atopic dermatitis. Under controlled conditions, UV light can be a useful tool in the biomedical field. For instance, a UV-B sensitive, low-voltage, solution-processed, thin-film phototransistor was developed for the safe and effective treatment of skin diseases [128]. To explore the effect of UV light on both causing and curing diseases, it is beneficial to quantify UV light carefully. UV light is mainly divided into three groups: UV-A (320 – 400 nm), UV-B (280 – 315 nm) and UV-C (100 – 290 nm). The detection of UV-A light and UV-B light is done by portable technologies. However, they do not offer high accuracy due to the continuous need for calibration [13]. High accuracy and real-time devices are still required. Low-voltage, solution-processed organic phototransistors are promising candidates in this field to obtain fast and accurate results. On the other hand, numerous kinds of research have been increasingly focused on the development of NIR-sensitive sensors for medical diagnostics, for instance, pulse oximetry and monitoring blood pressure [9,15]. Home-assisted biomedical sensors have gained more demand than ever before, due to increased hospitalisation during the Covid-19 pandemic [129–132]. Photoplethysmography (PPG) sensors can be integrated into home-assisted kits and offer tremendous advantage to monitor cardiovascular and atherosclerosis disease markers, such as heart rate (HR), blood pressure (BP), heart rate variability (HRV), arterial oxygen saturation (SpO_2), arterial ageing. Most basic human characteristics can be evaluated by the flow of blood in the subcutaneous tissue. PPG sensors can detect these indicators by monitoring pulsatile changes in blood flow [133–136]. The device can be operated in two different modes: Reflective or transmitting mode. Several studies include excellent work on PPG sensors [137–139]. “Therapeutic window” or “diagnostic window” are considered when studying light absorption of the tissue. Biological tissues exhibit low absorbance. It explains why long penetration distance is critically considered in biomedical sensors, otherwise, the light is scattered by cells and proteins. The long-wavelength range (600 – 1600 nm) of the NIR and SWIR account for light absorption through the tissue (Figure 1.16), which can penetrate the deep subcutaneous part [5,15,16,36]. Red and NIR regions provide the largest contrast between the absorption of oxyhemoglobin (HbO_2) and hemoglobin (Hb), thus enabling greater accuracy and selectivity in detection. Depending on the arterial pulse, the light absorption varies, hence the optical density and path length can change [15].

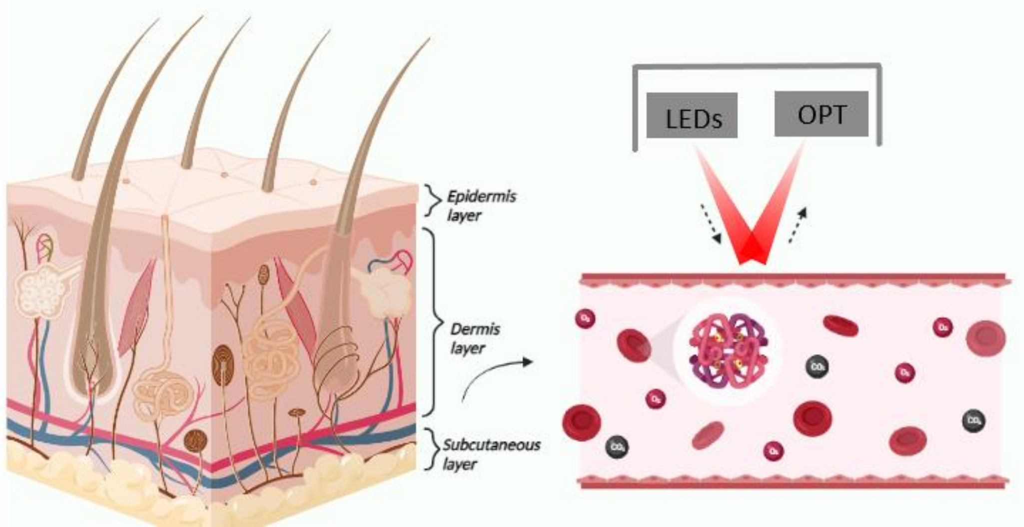

Figure 1.16 : Skin tissue and light absorption of erythrocytes. In this figure, the device mechanism is in reflective mode. This figure was created with BioRender.com.

Xu et al. reported using solution-processed DPP-DTT:PCBM BHJ as an active layer in OPT devices as PPG sensors in the reflection mode [15]. In this study, a hybrid design was demonstrated (Figure 1.17). They utilised a 1.8 µm-thick polyimide (PI) as the substrate, due to its smooth surface, good chemical stability, biocompatibility and excellent thermal stability. The applied bilayer dielectric (Al_2O_3/SiO_2) led to achieving a low operating voltage (< 3 V).

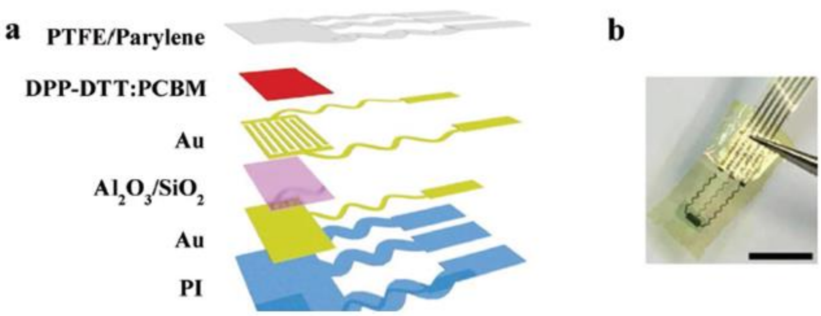

Figure 1.17 : Schematic of the (a) device structure of the flexible OPT, (b) figure of a freestanding OPT.Reprinted with permission [15]. Copyright 2017, Wiley.

To increase the mechanical stability of the sensor, PTFE/Parylene was used as the encapsulating layer. Comparing their device with commercial PPG and electrocardiography (ECG), they reported higher accuracy (0.3 % error) and better performance than conventional ones, giving promise for low power and real-time monitoring sensors. For evaluating pulse pressure variation, they compared their hybrid PPG and a commercial PPG by taking a reference pulse pressure (PP). In different positions of volunteers, PP showed fluctuating results, and hybrid PPG and reference PP exhibited similar trends. Most recently, Tao et al. reported tremendous improvement in detectivity levels for optoelectronic applications, especially UV-sensitive photodetectors [140]. They designed a device with a BGTC configuration and chose triphenylamine-based compounds as the light-sensitive active layer. 1,6-distriphenylamineethynylpyrene (1,6-DTEP) and 2,7-distriphenylamineethynylpyrene (2,7-DTEP) were designed and synthesized, and drop casted on *n*-octadecyltrichlorosilane (OTS)-modified SiO_2 / Si wafer. 2,7-DTEP showed P_{max} = $4.35x10^3$ and R_{max} = $1.04x10^5$ AW^{-1}. Its D* value was $5.28x10^{16}$ Jones under 370 nm UV light. Moreover, 1,6-DTEP showed Pmax = $1.6x10^5$, Rmax = $2.86x10^6$ AW^{-1} and ultrahigh D* value = $1.49x10^{18}$ Jones under 370 nm UV light. They attributed their results to the production of more photogenerated charge carriers under highly energetic illumination. They also mentioned that under 370 nm UV light, trap densities were reduced. The rhombic crystal structure of 1,6-DTEP gave the highest μmax value (2.1 $cm^2(Vs)^{-1}$) in the c-axis. I_{on}/I_{off} was up to 10^6. However, 2,7-DTEP gave μ value around 0.025 $cm^2(Vs)^{-1}$. Overall, they concluded that tighter molecular packing of 1,6-DTEP along with longer molecular conjugation led to higher D* and μ values. Most recently, Jiang et al. developed a transistor device that comprised an organic solar cell and a magnetic array covered by silver (Ag) nanowires (Ag NWs) [141]. They aimed to obtain a device that could be implemented as an artificial intelligent skin (touchless human–machine interaction) or used in optical communication. The photoactive P3HT: PCBM layer and the magnetic array part were deposited by spin-coating. When an appropriate magnetic field was applied, the magnetic array would be placed on the bottom contact. The photocurrent flowed through the device; thus, the phototransistor was in its on state. In other words, the magnetic part acted as a gate electrode. Li et al. studied an n-type small molecule as an active layer in BGTC OPT for the next generation of NIR-sensitive, low-cost sensing devices [39]. This n-type small molecule (BODIPY-BF2) was cast from the solution and showed good absorbance in the NIR region (around 850 nm). They reported that annealed (θ = 90°) film (for highly ordered texture) exhibited high mobility value (μsat = $1.13x10^{-1}$ $cm^2(Vs)^{-1}$) and on/off current ratio ($1.12x10^6$). R-value was reported as $1.14x10^4$ AW^{-1} at 850 nm for annealed (θ = 90°) film. The dynamic photoresponse of the device was reported stable;

thus, it could have served as a good light switch. The F groups of BODIPY-BF2 could provide an O_2 and/or H_2O barrier property, contributing to the stability and lifetime of the device. A flexible and novel design with ultrashort channel length was demonstrated by Zhong et al. [142] for organic electronics applications in the Vis region. Ag NWs were deposited on the dielectric layer, and a BHJ layer was chosen as the active layer (Figure 1.18). Poly[2,5-bis(alkyl) pyrrolo [3,4-c]-pyrrole-1,4(2H, 5H)-dione-alt-5,5'-di(thiophen-2-yl)-2,2'-(E)-2-(2-(thiophen-2-yl) vinyl)- thiophene] (PDVT-8) and $PC_{61}BM$ was used as the D / A. Solutions were prepared in a mixture of chloroform and chlorobenzene. BHJ was spin-coated on the Ag NWs. For flexibility, a PI substrate was deposited by blade coating. Under 720 nm light illumination, high R (750 AW^{-1}) and P (1 x 10^6) values were recorded. D* was as high as 4.54 x 10^{15} Jones.

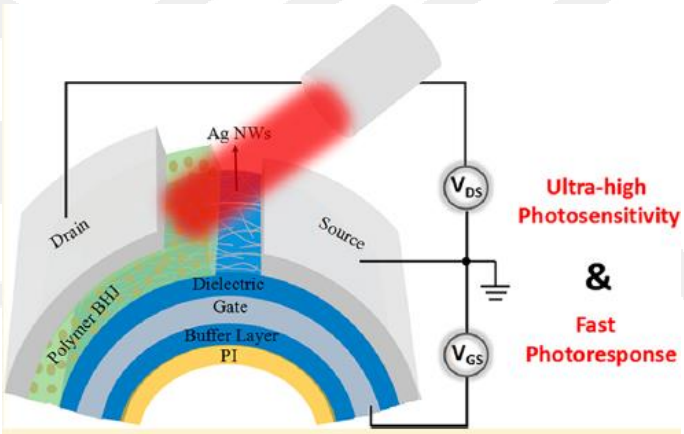

Figure 1.18 : Device structure of highly flexible and novel OPT. Reprinted with permission from [142]. Copyright 2018 American Chemical Society.

The lowest switch-on time of 0.72 s was achieved for 30 % chlorobenzene solutions. Moreover, at 30 % concentration, the surface area of crystals was found at the highest level. It was reported that this concentration could deliver the most efficient exciton dissociation. As the bending radius went down from 54 to 18 mm, a slight decrease of R was noticed which meant the device had good mechanical stability.

Liu et al. reported that a flexible, high-response OPT (BGTC configuration) could be produced by the introduction of a metal-ligand charge transfer molecule [143]. Ruthenium complex 1, a photosensitizer was used to enhance the responsivity and EQE value of the device by the active layer which was an n-type molecule *N,N'*-bis(2-phenylethyl)-perylene-3,4:9,10-tetracarboxylic diimide (BPE-PTCDI). Ruthenium complex 1 was deposited by drop-casting. At V_G = 80 V, the highest R-value (7230

AW^{-1}) and D* (1.9x10^{13} Jones) were obtained. The findings were attributed to electrons injection into the active component. When illumination excited the ruthenium complex, ground-state electrons were injected into the BPE-PTCDI. Ru^{2+} was oxidized to Ru^{3+}, which meant holes were trapped. PI substrate was selected to obtain a mechanically flexible device for wearable organic electronic, flexible image scanners, biomedical sensing gadgets applications. Lee et al. used a doping agent, tris (pentafluorophenyl)borane, to fabricate a short-wave infrared OPT [144]. They spin-coated poly[N,N'-bis(4-butylphenyl)-N,N'-bis(phenyl) benzidine as the gate-sensing layer in the SWIR range (λ = 1000 – 3200 nm) and achieved R level = 538 mAW^{-1} at λ = ~ 1500 nm and R = ~ 222 mAW^{-1} at λ = 3000 nm. When the light was exposed to the device, the gate-sensing layer absorbed the light and generated excitons. Following that, the charge separation occurred. Therefore, more holes could be induced in the P3HT active channel. Electron transfer provided the lower bandgap which was required to realise the SWIR absorption. They reported that their study was a step for the next generation of soft electronic applications. BHJ phototransistors can offer high-quality device design since they have layers for light absorption and exciton separation. Crosslinked polymeric semiconductor and BHJ bilayers were studied in a BGTC configuration to obtain a NIR light detection for imaging applications [145]. Crosslinked poly(N-alkyl diketo-pyrrolo-pyrrole dithienylthieno[3,2-b]thiophene) (PDPP-DTT) was induced on the dielectric layer as the conducting channel and BHJ (PDPP-DTT:PC_{61}BM) as the photoactive layer by spin-coating. PDPP-DTT is a low bandgap (E_g = –1.2 eV) material. Under 808 nm-wavelength NIR light, the photoresponse characteristics exhibited that BHS OPTs had a V_{th} shift to more positive voltages. When the device was exposed to NIR light, the drain current showed an increase due to photogenerated charge carriers. The maximum R-value was 2 x 10^3 A W^{-1} at a light intensity of 1.66 μWcm^{-2}. By benefiting from the electron capturing of PC_{61}BM, more photogenerated holes went from the BHJ layer to the crosslinked conducting channel. The movement of charge carriers contributed to the drain current. Bending studies were also conducted. It is reported that the maximum P was kept at 1 mm bending radius. It indicated that this novel OPT design could provide a durability response to mechanical bending. In another study, a hybrid active layer was applied for a flexible NIR light-sensitive, solution-processed OPT [40]. The hybrid layer was compromised of n-type metal oxide (In_2O_3) / polymer {5,5'-bis[3,5-bis(thienyl)phenyl]-2,2'-bithiophene-3-ethylesterthiophene]} (PTPBT-ET) in a

BGTC structure. The polymer PTPBT-ET layer was deposited by spin-coating. In_2O_3 initiated fast electron transport and PTPBT-ET was used for NIR light absorbance. The study reported good responsivity (R = 200 AW^{-1}) and D* value (1.2 x 10^{13} Jones). Under 810 nm NIR light, the device had high electron density, since electrons could jump easily to the conduction band of the metal oxide. As expected, the threshold voltage presented a negative shift (from 6.9 to – 1.52 ± 1.21 V). A high charge carrier mobility of 7.10 ± 1.31 $cm^2(Vs)^{-1}$ and 3.2 x 10^7 of I_{on} /I_{off} ratio was observed. The flexibility of the device was investigated by placing the device on a PI substrate and applying PMMA as the passivation layer. Despite slight distraction on NIR light absorbance, the passivation layer provided the electrical stability of the device under the 5 mm-radii bending test to 1000 cycles. They stated that the proposed design with hybrid materials had the potential for image sensors and wearable health monitoring.

Studies on information storage in a friendly and flexible way have spiked significantly due to growing technological advancements. Keeping large amounts of data with low power consumption and achievable high central processing unit rates are the top priorities of scientists. The molecular size of organic materials provides an improved storage capacity. Apart from classical ways of data storage, such as random-access memory, read-only memory, or hard disk drive, researchers have been focusing on memristors and field-effect transistor-based memory devices. The emergence of flexible and wearable sensory devices, security, and communication technologies has encouraged the exploration of lightweight, soft and tailorable organic materials in OFETs, ferroelectric FET (FeFET) devices [146], and electrolyte-gated transistors (EGTs) [41,147,148]. In these designs, the gate electrode is the control terminal, while the transduction terminal is comprised of source and drain electrodes. Regarding data storage, memory devices can be volatile or non-volatile [41,147]. Volatile memory keeps the stored data only if the device is fed by a continuous voltage. After removing the voltage, the memory goes back to its initial state. However, a non-volatile memory device can continue to hold the information even if the power is switched off. FET-based non-volatile memory is attained via two different mechanisms. The working principle of FeFET memory devices is based on the polarisation change by using a ferroelectric dielectric layer in the transistor [149]. One of the most popular organic, solution-processable ferroelectric materials is PVDF, a copolymer of VDF and trifluoroethylene (TrFE). This type of memory is based on dipole orientation. Another memory category is based on charge/ion trapping [150]. Trapped charge carriers contribute to the device in the writing and erasing process. All these processes can be interpreted by the memory window which is the V_{th} shifting range in the writing and erasing process and is significant in assessing the memory device efficiency [41,147].

In a photomemory study [151], P(VDF-TrFE) was applied as a ferroelectric material for a TGBC-designed OFET. P(VDF-TrFE) contributed to two additional non-volatile states compared to traditional OPTs due to the polarisation of this ferroelectric material. The device showed the low resistance state ”1” after applying a – 100 V gate voltage in the writing process and the high resistance state “0” following the 100 V gate voltage in the erasing process. These two states retained up to 10^3 seconds which was promising for the long data storage capability. Under the three different states (state 0, state 1, and 60 V gate voltage state) for 10 s light pulse at 80 mW / cm^2 light intensity, varying photo-to-dark currents were observed. Therefore, it was reported that memory states could be modified by changing photo-to-dark current. When under the “0” state, positive polarisation occurred. That meant hole carrier density couldn’t reach the high levels. After light illumination, free e^-/h^+ pairs dissociated, giving rise to the hole carrier density. On the other hand, under the “1” state, negative polarisation occurred, so high hole carrier density was already induced. Increased hole carrier density was not obtained under light illumination which was the case in the “0” state. The authors claimed that this study could shed light on information storage and flexible electronics. Another study focused on the impact of dual functionality on non-volatile organic photonic transistors with both n-type and p-type materials [152]. The rod-coil material was used as a floating gate layer due to its functionality. The rod part was from a conjugated core and the coil part had long alkyl side chains. This material provided the necessary charge carrier trapping. This material served as both the charge carrier transport and memory layer, the negative effect of the energy barrier was hindered, and this led to the creation of a low-power consumption (0.1 V) organic photonic memory device. Threshold voltage shifting was observed in n-type (0.84 to – 7.01 V, negative shift) and p-type (positive shift) behaviour. Hence, a successful charge carrier trapping and writing process was achieved. Fast programming time (< 3 s) and prolonged retention time (over 10^4 s) demonstrated a promising new approach for photonic memory applications. Xu et al. fabricated a dual-band, hybrid (organic / inorganic) active-layer phototransistor for secure communication applications [153].

The organic active layer was a C8-BTBT single-crystal array. The device presented a high R-value of > 1.72 x 10^4 AW^{-1} and a broad absorption range (UV – Vis) in the 252 – 780 nm regions. The hybrid phototransistor was integrated into a matrix array (10 x 10 pixels) and performed successfully in secure communication. The C8-BTBT pattern was deposited through a shadow mask with "SOS" characters on a quartz plate, so the characters were invisible. This plate was exposed to the light illumination. Under Vis light, no characters could be seen, since C8-BTBT had high transparency to the Vis light. However, under the UV light, the C8-BTBT absorbed the light and as a result, SOS characters appeared (Figure 1.19) and remained until after the UV light was removed. This approach made it possible to keep information encrypted.

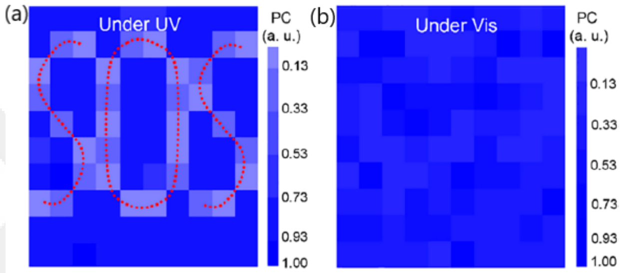

Figure 1.19 : The visibility of the "SOS" characters under (a) UV light, and (b) Vis light. Reprinted with permission from [153]. Copyright 2019 American Chemical Society.

Huang et al. reported a UV-sensing OPT device (Figure 1.20) for photomemory storage and photodetectors by UV light programming / electrical erasing mechanism [154]. Pentacene was selected as the active layer in the BGTC configuration.

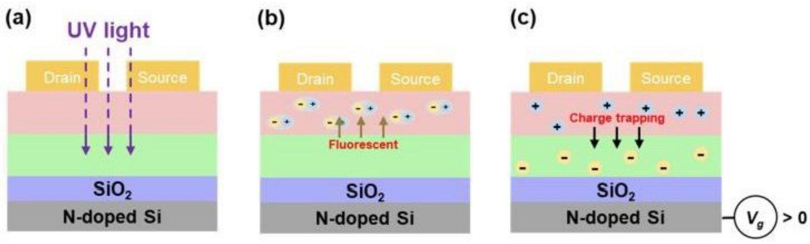

Figure 1.20 : Schematic diagram of the programming process of OPT, (a) OPT under the UV light, (b) the photoinduced excitons in pentacene, (c) charge trapping under reverse bias. Reprinted from [154]. Copyright 2019, with permission from Royal Society of Chemistry.

Below the active channel layer, doped fluorescent electret film was deposited at various doping ratios. The electret layer emitted strong fluorescent illumination, following that pentacene could absorb fluorescent light. The photogenerated excitons were separated when V_G was applied. Electrons were trapped in the electret layer; thus, hole concentration in the channel increased substantially (Figure 1.20). The electrical erasing process could occur when the opposite gate voltage. Electrons were detrapped and they neutralized the holes. Their results showed a memory window of 37.2 V, P-value of 1.92x10^6 and R-value of 45 AW^{-1} at 365 nm.

Poor charge extraction and low dissociation can limit the OPT device working in the NIR region. Low dimensional materials including quantum dots [155], nanowires [156], and 2D materials [157] were reported to offer solutions for high photoconductive gain or tunable Fermi level [158]. A novel design, solution-processed graphene/organic phototransistor was reported by He et al. [159] for NIR region detection. They designed a multifunctional device that could work both as a pulse monitor and a photomemory. They induced an electron extraction layer of ZnO on the graphene channel to block holes. A Graphene/ZnO/Ternary bulk heterojunction was adopted. The ternary BHJ layer expanded the response of the device to the longer wavelengths (760 – 1100 nm). After NIR light illumination created excitons diffused into D and A layers and became free dissociations. ZnO blocked the holes to enter the graphene layer with the help of a deep HOMO level (– 7.8 eV). Hence, recombination was prevented. The device exhibited a high R-value (6.1x10^6 AW^{-1}) and D* (2.4 x 10^{13} Jones). One of the main advantages of this study was to show pulse monitoring without contact in transmission mode (Figure 1.21). Figure 1.21c and d presented remote pulse monitoring.

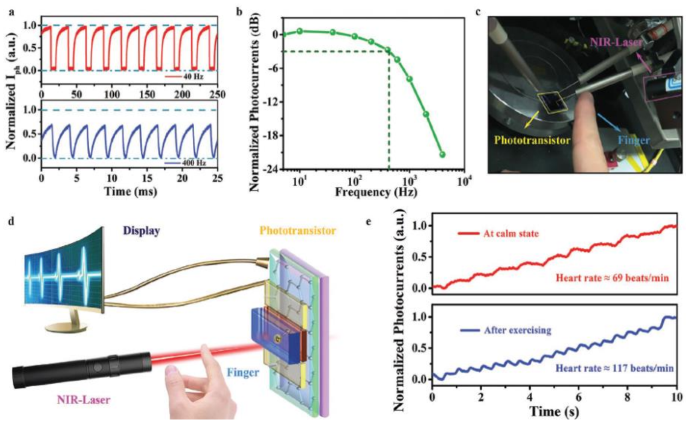

Figure 1.21 : Schematic of (a) normalized photocurrents of the phototransistor under light modulation, (b) normalized photocurrents as a function of modulating frequency, (c) and (d) the real image and the schematic of NIR-sensitive, pulse monitoring OPT sensor in transmission mode, respectively, (e) author's pulse signals and heart rate at calm state and after exercising. Reprinted with permission [159]. Copyright 2021, Wiley.

Results were promising for a non-touching approach. Non-touched monitoring agreed with remote and non-invasive monitoring. Moreover, this device could be turned into a photomemory device with a retention time of 1000 s in the atmosphere as a gate voltage of – 20 V.

PI:C5-BTBT based, solution-processed BGTC-designed OPT was designed [160] and investigated under different criteria, such as blending ratio effect, UV sensitivity, and electron-withdrawing groups. C5-BTBT is a small molecule that is blind to Vis but sensitive to UV-A light. Results were encouraging for photomemory applications. The 70 : 30 blending ratio (PI:C5-BTBT) gave the highest R (429 AW^{-1}) and P was 10^6, it had lower surface roughness (2.73 ± 0.4 nm) than others as PI content increased. By introducing PI, C5-BTBT grains merged. This can be explained by the reduced grain boundaries leading to higher mobility ($\mu = 1.00 \pm 0.17$ $cm^2(Vs)^{-1}$). Results showed that PI:C5-BTBT blends with fast writing < 1 s, and long retention times (149 s) could be preferred for the stored information applications.

1.4 Outlook and Future Perspectives

In this chapter, we methodically explained organic phototransistors, their basic properties, and their application areas supported by outstanding examples from the literature. Organic phototransistors offer unique advantages due to their field-effect structure and organic semiconductor active layer. The OSC bandgap tunability provides tremendous features. In addition, the chemical structure of OSCs can be modified to meet specific requirements. Their soft nature and flexible structure make them useful choices over conventional and rigid inorganic competitors. Solution-processable OSCs have made prototype and large-scale production fast and cost-effective. Biomedical imaging (e.g., continuous health monitoring), wearable electronics, optical communication (e.g., secure communication of encrypted information optical memory storage) and environmental monitoring devices are among the demanding application fields, where OSCs can be effectively utilised. Advancements in recent years have improved the electrical performance of OPT-based sensor devices, in particular, photosensitivity and photodetectivity. By synthesizing and exploring new organic materials (polymers, small molecules and blends), scientists can go beyond the possibilities to make device operations reach their climax. When it comes to wearable devices, biocompatibility is an indispensable criterion.

Therefore, various selections of natural and environmentally friendly materials are tried and tested. However, further work is required to improve the performance of OPTs in terms of their sensitivity and selectivity to various wavelengths of choice, low power consumption, bending capability sensor lifetime, and environmental stability to ensure device high-quality standards. Information technologies are growing and the OPT technology with its tremendous features could open new fascinating opportunities. Soon, phototransistor-based medical diagnosis and health monitoring sensors and home-assisted, and POC gadgets could be mass-produced cost-effectively using environmentally friendly materials and techniques with great reproducibility rate and peerless performance efficiency.

2. ORGANIC PHOTOTRANSISTORS AND THEIR APPLICATIONS AS ARTIFICIAL SYNAPSES[7]

2.1 Abstract

Sensors and the Internet of Things (IoT) have been revolutionizing our world by establishing a smart and more sustainable environment. Low-temperature processing and chemical functionality of organic semiconductors, high-k of natural dielectric materials, and mechanically flexible substrates make organic field-effect transistor (OFET)-based sensors an attractive alternative in many fields which including biomedical, security, environment, and neuromorphic computing technologies. One of the most striking application areas of OFETs is artificial synapses. Indeed, several electronic field-effect devices have recently been proposed to simulate synaptic functions of the biological brain. OFETs offer excellent opportunities to replace the conventional von Neumann's computing systems. Among the sensor devices used to build artificial synapses, OFETs are one of the most promising candidates for neuromorphic computers and bioelectronics owing to their easy processing, flexible device configuration, mechanical bendability, low cost, biocompatibility, and ductility. As such, organic phototransistors (OPTs) have attracted attention due to their many advantages, namely the simple preparation process, easy integration, and tunable optoelectronic properties over various device configurations. Moreover, the use of OPTs to emulate the unique properties of biological synapses is regarded as the key to the advancements of artificial intelligence (AI).

Herein, we first review the fabrication and operating mechanisms of OFETs and OPTs, briefly. The recent developments and applications of organic phototransistors as artificial synapses are thereafter described.

[7] This chapter is based on the following publication: **Tavasli, A.,** Atila, D. T., Faraji, S., Majewski, L. A., Trabzon, L. (2024). Organic phototransistors and their applications as artificial synapses, *Sensors and Actuators A: Physical*, ***371***(115311).

2.2 Introduction

This chapter introduces organic phototransistors explaining the fundamentals of their operation and discussing their potential applications as artificial synapses. Especially, the importance of the solution process in the development of low voltage OPTs is explored. From analog biomedical to digital information technologies, sensors find many practical uses. As such, many research disciplines must come together to create novel designs of sensors. At present, scientists are not restricted to using only conventional materials. Organic semiconductor (OSC)-based sensors have attracted considerable attention due to their unique advantages such as low-cost processing, good mechanical flexibility, as well as good biocompatibility and ductility. Organic phototransistors are a subcategory of light sensors called photodetectors. They have been intensively investigated because their three-electrode device structure offers exceptional advantages. It helps reduce the noise and amplify the signal from the external medium in a single device [161–163]. An OPT usually possesses a thin film transistor structure and uses an organic semiconductor as the active layer.

The organic semiconductor layer plays a crucial role in OPTs. It is the active layer of the design, and it can be deposited from the solution at room temperature, it can dramatically streamline the device fabrication process. Hence, OPTs can tackle the hindrance of high-temperature deposition conditions which paves the way for large-area, high-volume production. The fast and simple process, as well as cost-friendly procedures, make solution-based deposition techniques the popular choices for OPT fabrication. As such, lightweight, flexible, eco-friendly, and easily processible OSCs the best candidates for today’s highly demanding sensor market. By tailoring their chemical structures, one can achieve a new OSC material with very different properties [11,164,165]. Both polymers and small molecules can be used as the device sensing layer. They can be employed in the bulk heterojunction or hybrid layers. OPTs can detect a broad spectrum of light. This makes them suitable for a variety of applications such as biomedical imaging, security, and information technologies [14,166]. For instance, keeping large amounts of data in a low voltage device with a high central processing unit (CPU) is an increasingly popular field of study for scientists. Field-effect transistor (FET)-based memory devices such as ferroelectric FET can accommodate such needs. Non-volatile memory, a type of data storage in which memory does not go back to its initial state even when the power is cut off, can also be realized by OPTs [146,167]. A good example is the OPT-based optical memory where device operation relies on the dipole orientation and/or charge trapping [149,150]. AI has become a global topic of interest that frequently comes across in daily life. AI congregates different aspects of science. One of them is neurological studies. Synaptic phototransistors (SPTs) mimic the human neurological communication network. Similarly to the neurotransmitter matter released in synaptic gaps, charge carriers in SPTs are transferred from the source to the drain electrode in the transistor channel that acts like neurotransmitter molecules in the brain [167–169]. Moreover, the human brain has a visual perception which can be mimicked with OPT devices. As a result, there is a huge scientific demand to demonstrate brain-like computers by utilizing OPTs and their optical memory properties [170]. One of the challenges of neuromorphic engineering is the fact that currently available microelectronic fabrication technologies have been optimised to provide billions of homogenous units that operate at very high (nanoseconds) speeds for conventional circuits but these are not immediately compatible with many neuromorphic designs. Biological neural networks are composed of imprecise, heterogeneous computational units, with very dense connectivity, which process spatiotemporal analogue signals at a slow (millisecond) timescale.

While brain-like machines can be force-fit into digital technologies, they may be better suited for alternative implementation using solution-deposited, large-area electronic devices. These devices could form the basis of printed neuromorphic circuits that can be individually written and provide circuits that are readily customised at little cost. Also, there are major problems with organic semiconductor electronic devices for use in conventional circuits, i.e. they are relatively slow, low current, and do not provide high accuracy. These are the properties that biological neural networks already work with very effectively. Neuromorphic designs may provide solutions for robust analogue circuits operating under these constraints. Hence, the marriage of organic semiconductor electronics and neural systems appears to be a promising and original area of research that exploits the strengths of the circuit design and the constituent electronic devices. Apart from these above-discussed areas, OPTs can also be applied for clinical requirements.

The operation mechanism and applications of OPTs are discussed in greater detail in the subsequent sections. Firstly, Section 2.3 explains the fundamentals of OPT operation. Following that, novel designs of OSCs for OPTs and the solution processing techniques that are often utilized in the production of organic phototransistors are discussed in Section 2.4. The recent developments in the application of OPTs for artificial synapses are thoroughly reviewed in Section 2.5. Finally, a summary and the future prospects of organic phototransistors are given in the conclusion section.

2.3 Organic Phototransistors and Their Operation Mechanism

An organic phototransistor has the same structure as an OFET. Four different configurations are realized based on the position of the gate, source, and drain electrodes. An organic semiconductor layer, a dielectric layer, and a substrate complete the design of the transistor. With regards to the electrodes, in the case of ohmic contacts, the current can pass in either direction. On the other hand, in rectifying contacts, the current is allowed only in one direction. Work function (φ) is the required energy to remove an electron. Electron affinity (EA) (χ) is the energy released when extracting electrons from the lowest unoccupied molecular orbital (LUMO) level, while ionization potential (IP) is the energy required to remove the holes from the highest occupied molecular orbital (HOMO) level. To choose a proper electrode with the aim of low contact resistance, generally, the Mott-Schottky model (vacuum level alignment) is taken into consideration. For a p-type OFET, high-work function metals are used for the source and drain electrodes due to their well-aligned structure with the HOMO level of the p-type OSCs. Generally, the work functions of OSCs are in the range of 4.8 – 5.3 eV. Gold (Au) (5.1 eV) is the most common metal for electrodes, while palladium (Pd), platinum (Pt), and nickel (Ni) are the alternatives. Easy hole injection from the electrode accounts for the necessity of the high work function metal due to the barrier height. For n-type OSCs, LUMO levels are usually between 3 and 4 eV. Low work-function metals are preferred for this reason. Aluminium (Al) and calcium (Ca) metal electrodes are the most appropriate candidates. One drawback of these metals is their highly reactive nature.

They can degrade rapidly with air exposure. When the metal and the semiconductor are brought into contact with each other, charge transfer occurs which leads to “band bending” in the organic semiconductor and the formation of energy barriers. When the

Fermi level of metal is below that for the organic semiconductor, downward band bending occurs. When the Fermi level of metal is above that of the organic semiconductor, the situation is reversed. As a result, the accumulation of charge carriers takes place at the metals–semiconductor interface [7,171–173]. Dielectric/ semiconductor and electrode/semiconductor interfaces have strong impacts on the transistor performance. Surface morphologies of OSC significantly influence the transistor operational characteristics, as well, depending on whether it is on the top or bottom. Another distinctive factor influencing OFETs is the presence and density of the trap states in the active layer, particularly in the top contact (TC) configuration before the metal electrode evaporation [7]. Two configurations of OFET, the bottom gate – top contact (BGTC) and bottom gate – bottom contact (BGBC) are frequently chosen for sensing studies. In the BGTC configuration, due to the intimate contact between the OSC and source (S) / drain (D) electrodes, contact resistance is usually low. However, there are some shortcomings to consider in the BGTC configuration. For instance, the deposition of electrodes by evaporation at high temperatures or solution-processed metal ink/polymer electrodes may damage the OSC layer. Attaining a small channel length is another difficulty in this configuration. However, Li et. al. showed that benefiting from the nanoscale channel length and the improvement of gate control ability, vertical OFETs display small subthreshold swings (73 mV/dec) and threshold voltages (V_{th} = –1.2 V) which improves transistor switching performance [174]. Also, in another study that focused on an artificial retina – visual system carried out by Feng et. al. [175], a vertical synaptic transistor was successfully designed with an ultrashort channel length of 3 nm. Another choice of device structure is the BGBC configuration. It allows very small channel lengths since in this design, S / D electrodes are first defined on the dielectric layer, followed by deposition of the OSC film. Although bottom contact devices are easier to integrate into low-cost manufacturing, they generally show much higher contact resistance compared with their TC counterparts [29,173]. Furthermore, S / D contact treatment with self-assembled monolayers is necessary for BC structures to obtain high carrier mobility. When charge carriers are injected from the metal electrodes they must pass an injection barrier. This barrier manifests itself as the contact resistance which is the sum of the channel resistance ($R_{channel}$) and the contact resistance (R_C). Due to the position of the electrodes in the BGBC configuration, the bulk resistance is not an issue. This is because charge carriers can be relatively easily injected into the active layer channel [176].

- Key analytical parameters of OFETs are [32]:
- The mobility of charge carriers (μ)
- The threshold voltage (V_{th})
- The subthreshold swing (S)
- The on/off current ratio (I_{on} / I_{off})

Charge carrier mobility (μ) is a fundamental figure of merit in OFETs. It expresses the relationship between the applied electric field and the charge carrier velocity. Its unit is cm^2 $(Vs)^{-1}$. The threshold voltage (V_{th}) is the minimum required voltage at which the device begins to accumulate charge carriers in the active layer. Its unit is V. The subthreshold swing (S) measures how quickly the transistor can be turned on from the off state. Its unit is V/dec. The on/off current ratio (I_{on} /I_{off}) describes a ratio of the on to off current. I_{off} is the current when the device is off. I_{on} is the current when the device is fully on. In an ideal case, the I_{on} should be as high and I_{off} as low as possible. The values of μ, V_{th}, S, and I_{on}/I_{off} depend on the morphology and structure of the semiconductor, and the quality of the semiconductor/dielectric interface. If S is known, then the interfacial trap density can be N_{it} calculated using equation (2.1):

$$N_{it} = \left(\frac{\mathrm{Slog(e)}}{k\mathrm{T/q}} - 1\right)\frac{C_G}{q^2} \tag{2.1}$$

where k is the Boltzmann's constant, T is the absolute temperature, q electron charge and C_G is the gate capacitance per unit area. The unit of N_{it} is cm^{-2} eV^{-1}. If N_{it} is assumed zero, the S value is around 60 mV/decade at T = 300 K [177,178]. Hence, S describes the quality of the semiconductor/dielectric interface. The presence of traps causes an increase in S.

Developing a dielectric material with a high capacitance value is an attainable and frequently preferred method to achieve low voltage sensor devices. This often means employing high-k (ε_r) dielectric materials [179]. The impurities at the OSC/dielectric interface and the surface roughness of the dielectric layer can distract the electrical properties of the device. The defects and/or chemical groups of the dielectric surface, for instance, silanol groups (– Si – O) on SiO_2, can act as traps of electrons [180].

Surface modification with self-assembled monolayers (SAMs) is a suitable choice to improve the electrical and morphological properties of the device. They have been developed with various functionality techniques such as attachment selectivity, cross-linking, hydrophobic and hydrophilic characters. A typical structure of a surfactant is composed of a terminal group, an alkyl linear chain, and an anchoring group. The anchoring group binds to the dielectric surface. The responsibility of the alkyl liner group is to make van der Waals interactions for the SAM self-ordering process. The terminal group provides stronger interactions with the OSC layer [181,182]. One of the most popular gate dielectric treatments is the application of silanes such as *n*-octadecyltrichlorosilane (OTS). Tantalum pentoxide (Ta_2O_5) is a suitable candidate for low voltage, high-current OFETs due to its high-*k* ($k \approx 20$) value. Mohammadian et al. made the anodic oxidation method. Anodization is a low-cost, solution-processed deposition process [73]. In OTS-modified Ta_2O_5, OTS molecules were attached to the dielectric surface through the chemical reaction. Results demonstrated that OFETs using OTS-modified Ta_2O_5 worked well under 1 V with μ = 0.22 $cm^2(Vs)^{-1}$. Nevertheless, there is an inevitably growing interest in low-waste dielectric materials for a sustainable electronic future. Natural and environmentally friendly dielectrics can be employed such as almond gum ($k \approx 8$) [183], gum arabic ($k \approx 30$) [74], khaya gum ($k \approx 30$) [184], and cashew gum ($k \approx 38$) [185]. These materials are popular choices for low-waste, biodegradable, high-*k* dielectric materials for low voltage OFET applications [186].

The semiconductor type and choice of dielectric influence the threshold voltage. By utilizing a high capacitance dielectric, more charge carriers are induced within the channel which enables the OFETs to operate at lower voltage due to decreased V_{th}. Functional groups in the dielectric can cause additional shifts in the threshold voltage. Due to the existing electron-rich terminal groups, V_{th} shifts to a more positive voltage range. Therefore, the charge carriers are already accumulated in the active channel layer even at $V_G = 0$ V. For a p-type device, trapped electrons contribute to the negative gate bias which makes the device operate at low voltages. The positive shift of threshold voltage is related to the concentration of holes. It can be said that the positive V_{th} shift is related to the trapped holes at the interface.

Two mechanisms account for the V_{th} shift in OPTs. First, under illumination, the photogenerated excitons in the OSC dissociate into free charge carriers; electrons (e^-)

and holes (h^+). Charge carriers are collected at/under the electrodes. In a p-channel device, electrons accumulate under the source electrode while the photoinduced holes in the channel flow to the drain electrode. Accumulated electrons reduce the charge injection barrier. The second mechanism is attributed to trapped electrons at the interface between the semiconductor and the dielectric. Trapped electrons decrease the potential of hole injection. It results in a decline in contact resistance and an increased drain current [32,177,187–191]. Although it has been thought of as a pitfall, in some cases, used to increase photosensitivity. For instance, polylactide (PLA), a biomaterial, is preferred to induce the charge trapping effect in OPT devices by tuning the interface of semiconductor/dielectric. Results indicate that using a polar group has a favorable effect on photosensitivity [33,192]. Deep and shallow traps are taken into consideration to understand the mechanism in detail. The origin of traps can be impurities, structural defects, grain boundaries, and self-trapping. Traps have a huge impact on charge carrier transport because the trapped charge carriers are no longer able to move. The columbic repulsion force between the trapped and other electrons gets stronger while the electron density increases [187]. The detrapping process is thermally activated. Deep traps only affect the V_{th} [177,193]. After deep traps are filled, charge carriers can move and are mobile. Trapped charge carrier concentration can be quantified [194,195] using equation (2.2).

$$\Delta N = \frac{V_{th} \text{ x } C_i}{q} \tag{2.2}$$

where ΔN is the trapped charge carrier concentration, Δ_{th} is the threshold voltage shift, C_i is the capacitance, and q is the elemental charge.

Hysteresis can be interpreted from the transfer curve. Back sweep current (BSC) is the sweep from the "on" to the "off" state. Lower BSC is related to a lack of charge carrier trapping. Traps at the interface between OSC and the dielectric layer, as well as dielectric charge storage, are responsible factors for the existence of hysteresis in OFETs and OPTs [182].

Critical points for analyzing an OPT device in a nutshell:

- One must decide whether the device is p-channel, n-channel or ambipolar. Basic transistor characteristics can be interpreted from the output and transfer characteristics.

- Mobility (μ), threshold voltage (V_{th}) and I_{on} / I_{off} current ratio are important figures of merit.
- If the V_{th} shift exists, it means a charge carrier generation has occurred.
- The value of S indicates the charge carrier trap density.
- For low voltage OPTs, the optimum dielectric layer thickness (d) and dielectric constant (*k*) have to be determined.
- The dark current (I_{dark}) and after illumination, the light current (I_{light}) are parameters to consider for the light sensing performance.
- The OPT is evaluated upon exposure to the incident light of different wavelengths (λ) and optical powers (P_{opt}).
- The performance of OPTs is characterized by determining responsivity (R) photosensitivity (P) and detectivity (D*) as the most important figures of merit.
- One should evaluate the current-voltage hysteresis of the OPT.
- Establish if the environmental stability of the device makes it superior to its rivals on the market.

2.4 Solution-based Processing Techniques and Organic Semiconductors for Organic Phototransistors

An effective sensor should meet the requirements of the application area of interest. Lai et al. mentioned critical members for OFET devices. Transparency, flexibility, large-area fabrication, and the ability to operate under low voltage are fundamental requirements for today's point-of-care and wearable sensors [196]. Solution-processed organic small molecules and/or polymers can satisfy all the above requisites. The solution-based deposition techniques facilitate easy and cost-effective thin film coating even on natural, flexible polymers. The whole process is conducted at room temperature, and after coating, an annealing process is applied to evaporate the solvent. However, thermal evaporation techniques require a high temperature to evaporate source material in a high vacuum environment that may damage organic semiconductors. Thermal evaporation devices are more complicated than the solution process types of equipment which are not cost-effective and consume much energy. Hence, it is not a handy way to deal with this kind of device for coating [197]. Although thermal evaporation isn't a convenient way to coat organic polymers, small molecules [198] such as 2,7-dioctyl[1]benzothieno[3,2-b][1]benzothiophene (C8-BTBT) can be coated by this technique which allows to the growth of a crystalline, highly ordered film [199,200] on the surface and leads to a faster device in synaptic transistors [201].

2.4.1 Solution-process techniques: Spin coating and inkjet printing

Room temperature, cost-friendliness and high throughput of solution-based techniques make them the inevitable choice for large-area productions of sensor devices [202]. Combining the advantages of organic electronic materials with the superior functionality of solution-processed techniques leads to outstanding devices at the end of the production process. Solution-process offers a tremendous advantage by controlling the molecular packing. Solution-based techniques can be classified into three categories: self-assembly, coating, and printing. The most popular method for coating the organic semiconductor and dielectric layers in OPT devices is spin-coating. In spin-coating, the operator drops the material solution from the top onto the center of the substrate and rotates it. Spin speed and duration, and substrate surface hydrophilicity are critical factors in spin coating [203]. The spin speed and acceleration have a major impact on the control of the thickness of the coated layer [179]. Inkjet printing is another solution-processable method for large-scale production. Droplets are deposited through a nozzle onto a substrate. Viscosity and the quality of the solution are important properties in obtaining a uniform deposited layer. Although its machinery process is not cost-effective, inkjet printing is an efficient method to achieve high-quality thin films without material wastage [204].

2.4.2 Solution-processable organic semiconductors and polymeric phototransistors

Phototransistors can detect different wavelengths of the spectrum which is in line with the aim of the study. The working range of phototransistors is related to the semiconductor material and its bandgap. Inorganic semiconductors are preferred in phototransistors since they have a high charge carrier mobility. Moreover, traditional inorganic materials have been widely in demand due to their high dielectric constant when used as the insulator layer. In inorganic semiconductors, there is an energy gap, so-called bandgap, between the top of HOMO and the bottom of LUMO. This is the bandgap that allows a material to be either insulating or semiconducting. However, especially in recent years, organic semiconductors have stepped forward. Not only their solution-processability and low-cost manufacturing production but also their flexibility move them into advanced studies. Their traditional counterparts are produced by high-temperature vacuum deposition techniques which are not cost-friendly. Moreover, traditional semiconductors are rigid and are not suitable for wearable electronics. The flexibility of OSCs even after many cycles of bending is essential to today's wearable sensor studies that are used in biomedical and security applications. OSCs have both sigma σ bonds and π bonds in their structure due to sp^2 hybridization. π bonds allow more flexible charge carrier transport between molecules since they require less energy than σ bonds [54]. In organic semiconductors, charge carriers are called polarons. Polarons are self-localized. Localization of charge carriers is associated with the hopping transport taking place in OSCs [54]. For intrinsic semiconductors, there is no intentional doping. Therefore, they have low free-charge carriers. Intrinsic charge carrier concentration is shown by equation (2.3).

$$n_i = N_0 \exp\left(-E_g/_{2kT}\right) \tag{2.3}$$

where n_i is the intrinsic carrier concentration, N_0 is the effective density of states (DOS), E_g is bandgap energy, k is the Boltzmann constant, and T is temperature.

Some special methods are being employed to generate charge carriers in OSCs [54,171,205]:

- Chemical doping
- Photoexcitation (generation of electron-hole pairs)
- Carrier injection from electrodes
- Field-effect doping

It is noteworthy that by the state-of-the-art approaches to the synthesis of organic semiconductors, chemical doping can be controlled, and impurities can be eliminated, thus high purity materials can be obtained [7]. In organic semiconductors, the dielectric constant (ε_r) is low ($\varepsilon_r \approx 3 - 4$), however, it is very high for inorganic semiconductors (ε_r of Si=11). Binding energy comes from Coulombic Force between $e^- - h^+$. Thus, OSCs have high binding energy. In this case, "Frenkel Exciton" is applicable in which $e^- - h^+$ pairs (excitons) are tightly bonded to each other [54,171,206]. Binding energy (E_b) can be described by the following equation (2.4):

$$E_b \cong \frac{q^2}{4\pi\varepsilon_r\varepsilon_0 R} \tag{2.4}$$

where q is the elemental charge, ε_r is the relative permittivity of the material (i.e. the material's dielectric constant, k), ε_0 (8.854×10^{-12} Fm^{-1}) is the permittivity of free space (vacuum), and R is the exciton radius.

Polymers and small molecules are the active layers of organic phototransistors. Thiophene-based conjugated molecules are electron-rich, planar aromatic heterocycle molecules that are the most extensively investigated molecules due to their simple functionalization ability. They have demonstrated the highest reported mobilities of solution-processed polymers [207]. Poly(3,4-ethylenedioxythiophene) (PEDOT) is a member of polythiophenes and combining it with poly(styrene sulphonic acid) (PSS) substantially improves its solubility. Due to the electrical conductance and biocompatibility of PEDOT:PSS, it can be used in sensor devices even as an invasive sensor. It has tremendous potential in the studies of electronic sensor devices and biomedical flexible sensors such as organ-on-a-chip designs and biosensors based on organic electrochemical transistors [208–210].

Polymeric phototransistors (PPTs) take advantage of outstanding features of organic semiconductors such as lightweight and solution-processability. Therefore, they require special polymers and molecules that their bandgap match with the energy of the light [202,211,212]. For instance, fullerenes are not suitable for red light due to their wide bandgap (1.6 – 2 eV). Mixing donor and acceptor layers to make a bulk heterojunction or combining them as separate planar layers helps to improve the molecules. Another problem is the low mobility of NIR light-sensitive n-type small molecules. OSCs are responsible for light absorption, exciton creation, exciton separation and charge carrier transport. Designing the chemical structure of polymer or small molecule differently from their pristine form and/or using a single layer or heterojunction structure makes a huge impact on the the light absorption, separation of charge carriers and charge carrier mobility. Polymers show a more controllable molecular structure over small molecules. One attainable method is to endow OSCs with convenient functional groups. Introducing different side chains into the polymer can change the solubility of the polymer. A more soluble polymer active layer is highly profitable for solution-processed OPT studies. Air and humidity stability are critical factors for OPT sensor devices and their shelf life. The degradation mechanism is related to the surrounding environment of the device and its microstructure. Unencapsulated OFETs are susceptible to air and humidity, hence, the oxidative degradation of organic materials and absorption of polar H_2O molecules occur. It decreases the lifetime and quality of the sensor devices [213]. To establish long-term stability, solutions can be compiled like modifying chemical structures by removing susceptible groups and/or encapsulation the device. Electron-donating groups make the device less stable in the ambient environment. On the other hand, substituting electron-withdrawing functional groups can lower the HOMO level and increase the stability of the material. However, for the transient bioelectronic devices, the degradation rate and method are the critical factors in designing the device with biodegradable substrates such as paper, silk fibre and chitosan in the application areas of biomedical studies [186]. Improving the semiconductor/dielectric interface, creating additional layers (light absorption layer and conducting channel) as hybrid layers, and mixing OSC material with nanoparticles or photoactive materials make the low light detection of OPTs possible [81,211,212,214–216]. Changing molecular weight or adding new side chains makes it possible to gain a novel ability to yield high mobility in the active layer. Crystallinity is a morphology parameter that affects efficient charge carrier transfer. Closely packed, well-ordered molecules promote high mobility. $\pi - \pi$ orbital overlap between neighbouring molecules can increase the charge carrier delocalization. It should be noted that structural defects such as grain boundaries and grain size have a pivotal impact on intermolecular charge carrier transfer. Grain boundaries can cause the scattering of charge carriers in organic molecules and may result in a decrease in mobility and high threshold voltage. Modifying the molecular structure, adjusting the bandgap, improving the interface between the semiconductor/dielectric layers, and controlling crystallinity are all methods to achieve high-performance, reliable and efficient OPT devices [202,214].

2.5 The Application of Organic Phototransistors on Artificial Synapses

2.5.1 Synaptic phototransistors

Conventional digital computers utilize the von Neumann architecture in which the memory units and the processing units are separated. However, this architecture creates a bottleneck in modern computing needs, such as big data and neural network applications. The energy required to transfer the data between the memory and the processing unit limits the efficiency of these computers. Nevertheless, the human brain’s ability to store and process data in massive parallelism within the same structure offers a more energy-efficient architecture in orders of magnitude compared to conventional computers. Thus, replicating the human brain can offer an alternative to the von Neumann bottleneck. Not only the large energy consumption in von Neumann architecture is a critical problem, but also the amount of space they require is dramatically huge. The number of neurons in the human brain is anticipated approximately 10^{12} with 10^{15} synapses in 1 kg weight of the brain. Even though there are numerous neurons numerically, the energy consumption is extremely low (< 20 W vs. 15 MW of CPUs). The question that comes to mind is how this can be recreated with electrodes and semiconductors [186]. Every 10 fJ/synaptic event energy consumption of human brain functions (vs 10 pJ/synaptic spike for CMOS chips) includes memory, learning, gaining new experiments and information storage simultaneously. This fantastic low consumption is executed with the help of the adenosine triphosphate molecules in synaptic transmission. Neuromorphic computing, or neuromorphic engineering is a branch of computer engineering which gets inspired by the human brain and its functionality. Creating a sensor based on synaptic transistors that works like a human brain with low energy consumption is a tremendous approach to mimicking the biological side of the human brain mechanism. For these reasons, artificial synapses are a promising research topic for meeting today’s computing needs [217]. Synaptic transistors shed light on the realization of brain-like computing by mimicking brain functions for low-energy consumption sensory applications. Therefore, memory and learning are the main functions of the artificial synapses. Figure 2.1 shows the comparison between the biological elements and the respective artificial elements.

Transmission of neural signals is crucial for the human brain's perceptions, cognition, and memory functions. Synapses are a gap between neurons; releasing neurotransmitters through the synapses is a result of stimulating the brain's senses. The human brain can learn from experiences [218]. In a biological structure, synaptic plasticity describes a change in the strength of synaptic connections [219]. Synapses control the plastic strength of connections between neurons for data transmission. In the human brain, neurons are capable of going through changes in the process of gaining new experiences like learning and memorising. These modifications and the ability for adaptation give them the “plasticity” property.

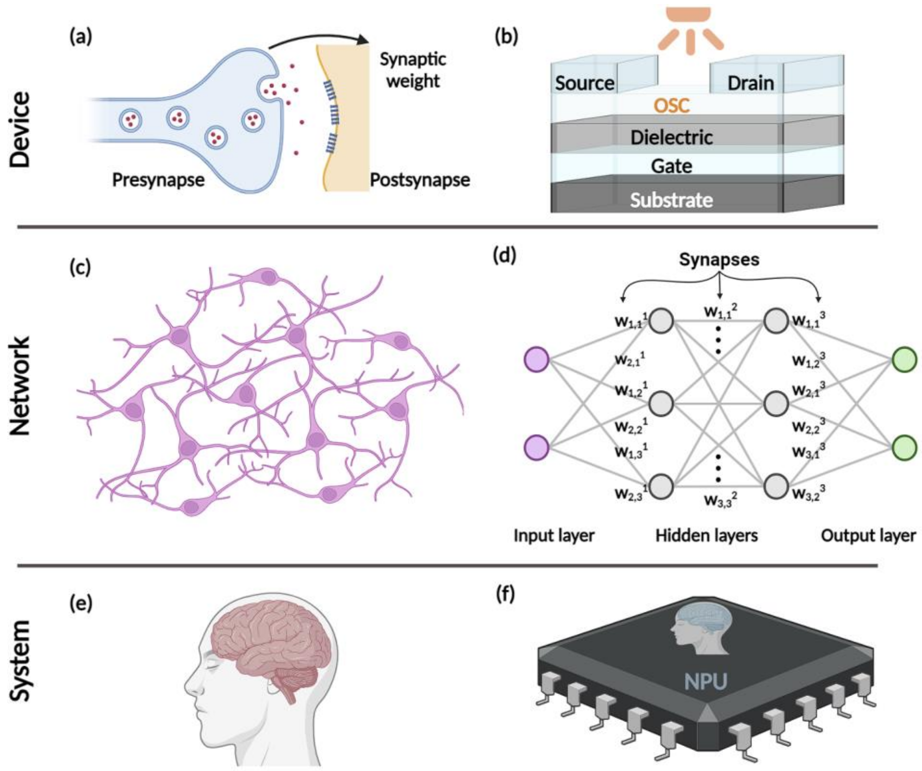

Figure 2.1 : Biological (a, c & e) & artificial (b, d & f) neural networks from device level to system level; (a) synaptic transmission through neurotransmitters, (b) simple light-receiving organic field effect transistor, (c) biological neural network, (d) artificial neural network, (e) human brain, (f) neural-network processing unit. This figure was created with BioRender.com (accessed on 29 Feb 2024).

The information flow that sometimes increases or decreases in these situations is called potentiation or depression, respectively. When the amount of released neurotransmitter molecules scales up, the postsynaptic neuron becomes sensitive to the triggers. In other words, the response of the target cell to the action potential increases which is called “synaptic potentiation”. As the human brain gets new experiences, the connection between neurons is getting stronger which is known as long-term potentiation (LTP). LTP allows humans to learn and remember their past experiences. Both electrical signals and chemical molecules react together in the neuron connection. When the presynaptic neuron is stimulated, the generated electrical signals go through the axon, and the action potential reaches the axon. Subsequently, neurotransmitter molecules are released and bind to the receptors on the postsynaptic neuron. Action potential on the membrane of the neuron controls the channel of ions. Opening of voltage-gated Na^+ channels results in the entering of Na^+ ions into the cell which is known as depolarization. Repolarization is related to closed Na^+ channels and opened K^+

channels. K^+ ions go to the outer part of the cell, which causes an increase in the negative voltage inside of the cell.

Transistor design with its three-electrode configuration can mimic these synaptic connections and transmission, so-called artificial synapses. For instance, mobile charge carriers in the channel are assumed as neurotransmitters. Synaptic weight means a charge carrier in the drain current (I_{DS}) and it is controlled by the trapped charge carriers. Synaptic plasticity can be described as a change in synaptic weight (W) which is related to the channel conductance. It can be short-term or long-term. Short-term plasticity (STP) is for information transmission, encoding and filtering of the neural signal. On the other hand, long-term plasticity (LTP) leads to more permanent changes in memory and learning. In a synaptic phototransistor, input signals are received and processed and appear thereafter as output signals. A gate electrode represents the presynaptic input terminal, and source and drain electrodes illustrate the postsynaptic output terminal [170]. The photogating effect occurs when photo-induced charge carriers are trapped. This effect plays a crucial role in synaptic transistors that can mimic synaptic functionalities. In a p-type synaptic transistor, hole-trap-assisted photogating is the main mechanism that lies under a negative V_{th} shift [175]. Photocurrent in the channel rises due to increased photoinduced gate modulation. This not only improves the response but also enables a long lifetime of charge carriers. The weight change of excitatory postsynaptic current (EPSCs) is defined as the difference between the maximum current (I_{max}) and minimum current (I_{min}) and this current is the drain current after and before light stimuli, respectively. EPSC is triggered by light stimuli and this leads to an increase in the channel conductivity [220]. Therefore, it isn't wrong to say that a gate bias can modulate the weight change.

Memory window is another term in synaptic transistors to describe the V_{th} shift range or the shifting range of the transfer curves through applying writing and erasing gate bias [194]. In the context of biological synapses, the synaptic weight refers to the strength of a synapse. Higher synaptic weight results in a transmission with a higher postsynaptic response. This behaviour allows the memory and processing functions to be done simultaneously in the biological synapse. As the synaptic weight increases the memory will strengthen, thus achieving long-term memory. Vice versa, the decrease in synaptic weight results in forgetting behaviour. This characteristic of the synapses is regarded as synaptic plasticity [218]. In the context of three-terminal artificial synapses, this behaviour is mimicked by changing the conductance of the channel as mentioned. Transistors can allow higher stability and repeatability for the operation of artificial synapses. Positive and negative gate voltages have an indisputable and controlled effect on the artificial synapses. Programming and reading are enabled in the gate electrode and the semiconductor channel. Transmission of information and learning are achieved at the same time in the OFET [221].

On the biological side, signals stimulate presynaptic receptors, and neurotransmitters are released, as a result, excitatory and inhibitory messages (excitatory postsynaptic potentials or EPSPs - inhibitory postsynaptic potentials or IPSPs) are sent out which increase and decrease the postsynaptic action potential, respectively. Likewise, related to the positive or negative voltage pulse, the source – drain current is changed as if behaving like the EPSP and IPSP. Dynamic ratio (on/off ratio) is the ratio of maximum conductance to minimum conductance. A larger dynamic ratio is preferred since a broader range of synaptic strength implies a better mapping capability and will better mimic the synaptic plasticity structure. Spike timing-dependant plasticity (STDP) suggests that the time difference between the presynaptic and postsynaptic spikes (interval) determines whether the synapse will strengthen or weaken. If the presynaptic spikes come before the postsynaptic spikes, synapses will strengthen, and if they come before the postsynaptic spikes they will weaken. The related figures of merits [222] for artificial and biological synapses are given in Table 2.1.

Table 2.1 : Artificial and biological synapse figures of merits.

Term	Biological Brain	Artificial Synapse
Synaptic plasticity	The term explains how the brain works. The synapses could strengthen or weaken depending on the synaptic activity.	The artificial synapse applications are trying to mimic plastic structure, and the following behaviours are tested as the parameters.
Synaptic weight	Main parameter that quantifies synaptic plasticity. Higher synaptic weight will result in a transmission with a higher postsynaptic response.	Synaptic weight in artificial synapses can be realized by the conductance of the channel. Change in synaptic weight can be calculated as $\Delta W = \frac{G_2 - G_1}{G_1} \times 100\%$, where G_1 and G_2 represents the channel's conductance before and after the stimuli respectively.

Table 2.1 (continued) : Artificial and biological synapse figures of merits.

<table>
<tr><th>Term</th><th>Biological Brain</th><th>Artificial Synapse</th></tr>
<tr><td>Short term synaptic plasticity (STP)</td><td colspan="2">Rapid changes activated by transient stimuli used for information transmission, encoding and filtering of the neural signal. PPF / PPD are the typical behaviours of STP.</td></tr>
<tr><td>Long term synaptic plasticity (LTP)</td><td colspan="2">More permanent changes in memory and learning, showing persistent excitatory / inhibitory behaviour, revoked by multiple inputs. Adjusted synaptic weights help form neural networks.</td></tr>
<tr><td>EPSC or EPSP / IPSC or IPSP</td><td colspan="2">Terms respectively mean excitatory post synaptic current, excitatory post synaptic potential, inhibitory post synaptic current and inhibitory post synaptic potential. These are the main device outputs analyzed with the input presynaptic signals.</td></tr>
<tr><td>Paired pulse facilitation/ depression (PPF / PPD)</td><td colspan="2">PPF is the synaptic behaviour where postsynaptic current (PSC) increases when a second input spike is supplied immediately following the first one. PPF index is defined as the ratio of the second PSC to the first one. Vice versa, the decrease in PSC due to paired input signals is called PPD.</td></tr>
<tr><td>Energy consumption</td><td>The energy consumption of biological synapse is around 10 fJ with spike voltage around 10 mV, ionic current around 1 nA and spike period around 1 ns.</td><td>Decreasing the energy consumption is of major importance in artificial synapses. Currently, around 10 pJ of energy is consumed per synaptic peak in CMOS chips.</td></tr>
<tr><td>Memory window (MW)</td><td colspan="2">MW is the difference between the threshold voltages during writing and erasing processes. It is an important parameter for memory applications and should ideally be large enough to ensure reliable reading.</td></tr>
</table>

Few architectures exist for three-terminal artificial synapse applications. Some of the designs are electrolyte-gated (EGFET), ferroelectric-gated (FeFET), floating gate (FGFET) and Van der Waals heterostructure (vdWH-FET) synaptic transistors (Figure 2.2) [222].

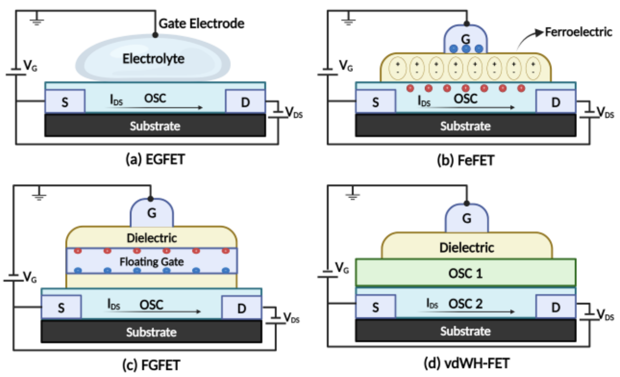

Figure 2.2 : Schematic representation of four simple top gate, bottom contact OFET architectures with applied forward bias; (a) EGFET, (b) FeFET, (c) FGFET, (d) wdWH-FET. This figure was created with BioRender.com (accessed on 29 Feb 2024).

The main benefit of EGFETs is the low energy consumption due to their low voltage operation. The EGFET works using the interaction between the ions in the electrolyte and charge carriers in the semiconductor. When an external electric field is applied, the ions either move towards the semiconductor or away from it, thus changing the carrier concentration in the semiconductor layer and changing conductance. In the context of artificial synapses, the migration of ions in the electrolyte can be analogous to the release of neurotransmitters, thus attracting the attention of neuromorphic device researchers. FeFETs on the other hand benefit from ferroelectric insulators as the gate layer and function as superior non-volatile memory devices. They exhibit low power consumption, and fast writing/erasing properties. These devices utilize the reversible polarization of the ferroelectric materials to create an electric field that changes the conductivity of the semiconductor layer. The two-dimensional (2D) ferroelectric materials are promising due to their potential for size reduction and elimination of current problems of three-dimensional (3D) ferroelectric materials such as the presence of charge carrier traps and gate leakage currents. FGFETs utilize the addition of a floating gate layer to the traditional FET structure. The addition of a floating gate by splitting the dielectric layer helps charge carrier trapping to retain conductivity for a longer time, which makes it a good choice for mimicking the long-term synaptic behaviours. Alternative structures such as semi-floating gate FETs are formed to overcome the high voltage requirements and long response time of the simple FGFETs. WH-FET transistors consist of combinations of different 2D semiconductors stacked on top of each other. By stacking semiconductors with different properties, various electrical and optical behaviours that mimic biological systems are achieved. Thus, heterostructures are a highly promising structure for synaptic transistors and neuromorphic applications [222].

Artificial retina applications are one of the most critical fields for artificial synapses. Phototransistors are a member of optoelectronic devices, and artificial vision systems can be configurated by applying phototransistor mechanisms thanks to their memory, signal processing and light-receiving properties [164]. Colour sensing, visual-assisted learning, and image processing are the areas in which artificial synapses can be facilitated [223–225]. Synaptic transistors open new ways in the progress of artificial intelligence by allowing the construction of a system like the biological structure.

2.5.2 The applications of synaptic phototransistors

Low-power sensors are essential implements in practical clinical applications. An ultralow power, vertical OFET was designed, and an electrolyte gate was applied for multisensory artificial synapses [226]. Blend of Poly(3-hexylthiophene) (P3HT) and 1,6-bis(trichlorosilyl)hexane was selected as a semiconductor layer in the corresponding study and spin-coated on the bottom drain electrode. A 5 × 5 synapse array was created, and the "X" letter was chosen as a model (Figure 2.3) to train image memory. Experiments showed that ten high amplitude (− 0.8 V) presynaptic stimuli with 0.5 s pulse width spaced by 0.1 s allowed long-term memory keeping for 300 s. Results were promising for image learning and memorizing functions.

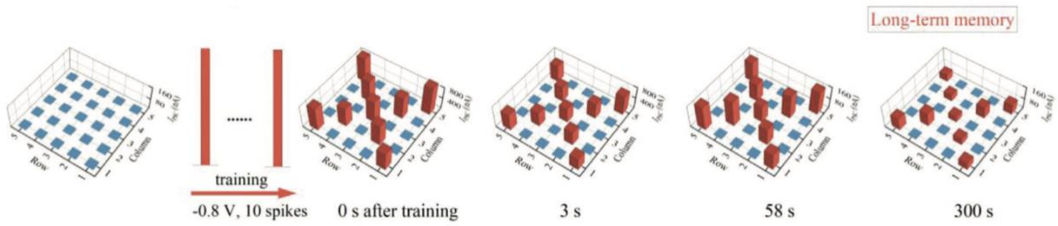

Figure 2.3 : The long-term memory state with ten high amplitude spikes of –0.8 V (spike width of 0.5 s, spaced by 0.1 s). Reprinted with permission from ref. [226]. Copyright 2022 John Wiley & Sons.

Another work [227] examined solution-printed OFET for designing a photosynaptic device in bionic optoelectronics. They introduced a Schottky barrier to regulate charge carrier injection and achieved a remarkable reduction in energy usage. Blade coating technique was applied for the OSC deposition, to create oriented growth of grains in OSC thin films for excellent charge carrier transport. Treated Ag S / D electrodes were used, they had lower HOMO levels than that of the OSC layer. This situation led Schottky barrier occurring. As the negative gate voltage was applied, holes accumulated at the interface. When the light illuminated the OSC, light-induced charge carriers went from the source to the drain and caused excitatory postsynaptic current (EPSC) (Figure 2.4).

The EPSC reached a peak value of 8 pA and then decreased to 3.9 pA after 60 s following the taking off light. The current decay was explained by the de-trapping process of the photogenerated electrons in the channel.

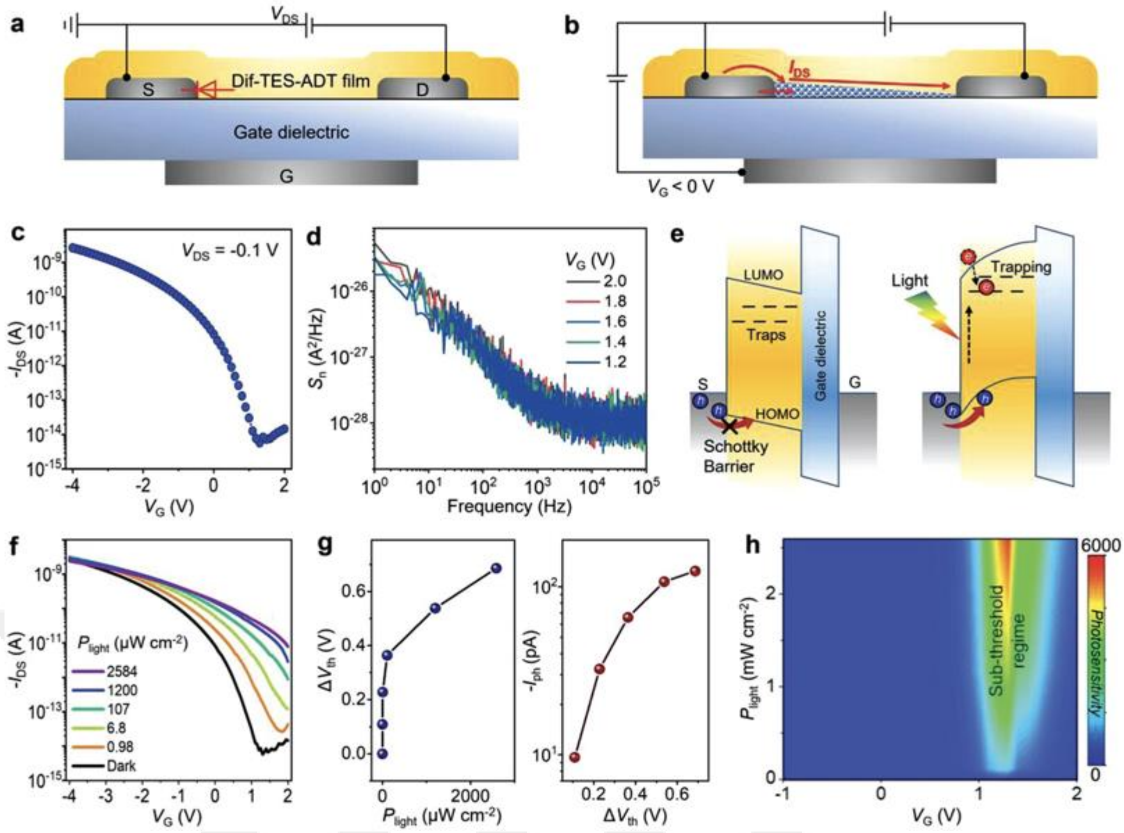

Figure 2.4 : (a) and (b) show the device under no V_G and a negative V_G, respectively, (c) gives room-temperature transfer characteristics at $V_{DS} = -0.1$ V, (d) measured noise power density (S_n) of the device, (e) energy band diagrams of Dif-TES-ADT and PFBT-treated Ag electrodes before (left) and after (right) light illumination, (f) transfer characteristics of the FSP-OFET in the dark and under white illumination, (g) dependence of threshold voltage shift (ΔV_{th}) on P_{light} (left panel) and dependence of photocurrent I_{ph} on ΔV_{th} (right panel), (h) extracted photosensitivity as a function of P_{light}. Reprinted with permission from ref. [227]. Copyright 2022 John Wiley & Sons.

As the W_{pulse} was increased, the EPSC peak current increased. Results manifested that the obtained time scales aligned with the STP process in the biological synapse. In the visible range, this OFET sensor showed sensitivity over an extended wavelength range, hence considered extremely suitable for recognising visible signals in the human vision system.

Detection of ultraviolet light and near-infrared light is always the target of military and biomedical applications. In the work by Jiang et al., [228] deep ultraviolet light stimulation was detected by a bottom gate-top contact (BGTC) synaptic transistor structure. Poly(3-hexylthiophene) (P3HT) was spin-coated as the OSC layer and a flexible poly(ethylene terephthalate) (PET) substrate was used to realise wearable artificial synaptic devices in the future. To mimic the biological behaviour, deep ultraviolet light was considered as the external stimulus, so that presynaptic neuron treatment was facilitated, while I_{DS} was the postsynaptic current. ΔEPSC reached 6.2 nA in the first 4 s of light stimulation, then gradually turned its initial current. As the light pulse width increased from 2 to 14 s, the ΔEPSC value went up from 2.84 to 17.57 nA, showing a good modulation effect. It was given that the ΔEPSC was controlled by varying the light pulse parameters. It meant that the deep ultraviolet light stimulation of the synaptic plasticity was accomplished. In addition, the learning and forgetting properties of the human brain were simulated by the illustrated “H” letter on an array. The array was triggered with different light pulses which were considered as learning sessions. After completing the learning session, the forgetting session was started. Results elucidated that this design could mimic learning, forgetting and storing information.

Another study reported on the synthesis of three fluorinated polystyrene polymers (ortho (*o*)–FPS, meta (*m*)–FPS, and para (*p*)–FPS) with superior charge-trapping properties [229]. The polymers were synthesised using radical polymerization by introducing fluorine atoms to polystyrene. The aim was to study different molecular positions of fluorine atoms in the benzene ring via side-chain engineering. The physical and chemical effects of these polymers on dielectric properties, and charge carrier trapping – de-trapping process were investigated for artificial synapse applications. The synthesized polymers were used as gate dielectric with the p-type 2,7-Didodecylbenzo[b] benzo [4,5] thieno [2,3-d] thiophene (C12-BTBT) semiconductor layer in BGTC structure OFET-based artificial synapses. All three OFETs had similar on/off currents around 10^{-3} A and 10^{-10} A, respectively (Figure 2.5). Photon memory performance of the OFET is measured by programming the OFET with 80 V gate voltage and 365 nm light for 1 second, erasing with – 80 V gate voltage for 1 second. The memory windows for C12-BTBT/*o*-FPS, C12-BTBT/*m*-FPS, and C12-BTBT/*p*-FPS OFETs were respectively 75 V, 80 V, 97 V. All three OFETs could retain memory for 10000 s with C12-BTBT / (*p*)–FPS showing the best retention curve. Introducing both the F atom and the para (*p*) position of the atom enhanced the charge storage capability. Increased molecular polarity led to higher ε_r. The OFETs also showed synaptic behaviours due to the enhanced charge carrier storage capabilities of the FPS dielectrics.

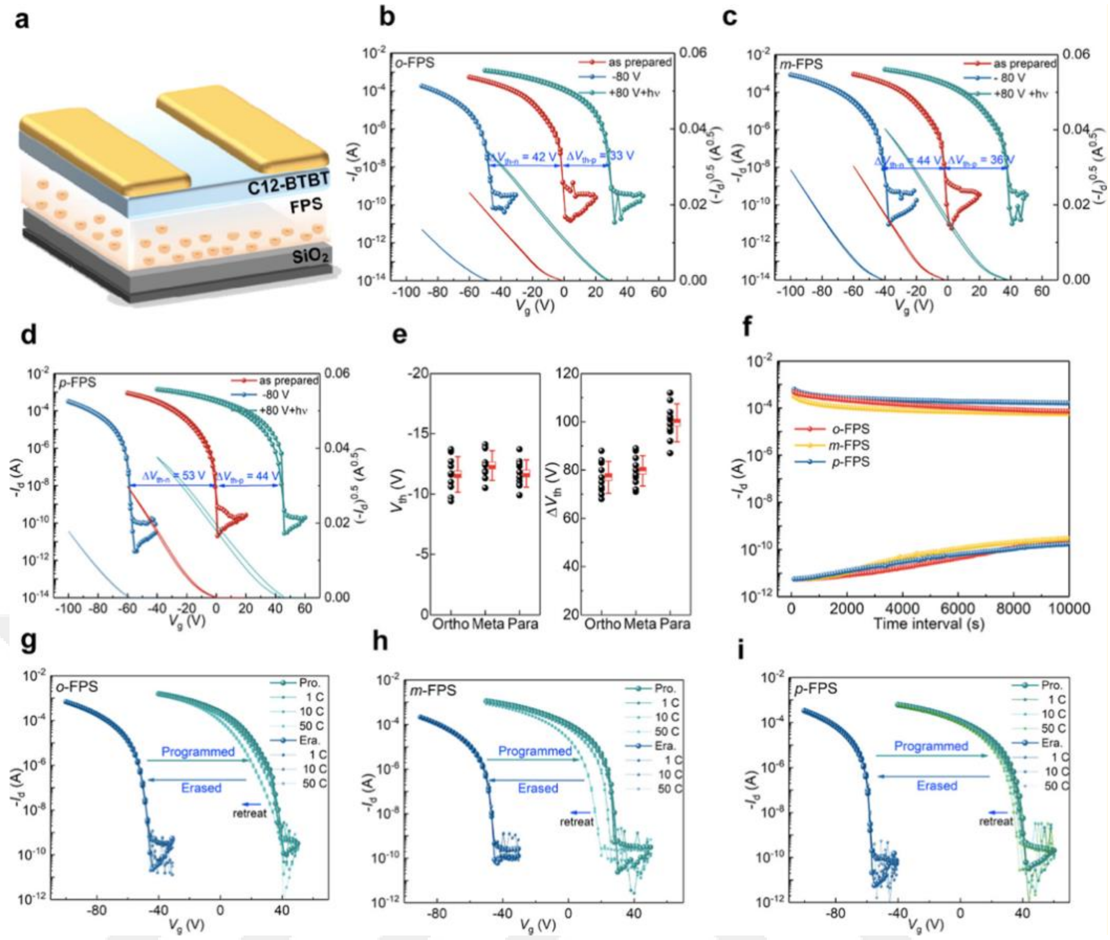

Figure 2.5 : (a) Device structure of OFET, (b−d) transfer characteristics of OFETs with (b) o-FPS, (c) m-FPS, and (d) p-FPS dielectric layers, (e) comparison of V_{th} and ΔV_{th} for OFETs with o-FPS, m-FPS, and p-FPS dielectric layers, (f) photon memory retention characteristics of OFETs with o-FPS, m-FPS, and p-FPS dielectric layers, (g−i) repeat stability of photon memories with (g) o-FPS, (h) m-FPS, and (i) p-FPS dielectric layers repeatedly scanned 50 gate−voltage cycles. “C” represents circles. Reprinted with permission from ref. [229]. Copyright 2022 American Chemical Society.

Under a 365 nm light spike with 0.5 s duration, OFETs showed spiking EPSC with the (*p*)–FPS having the slowest decay of around 30 seconds. Multiple light spikes with increasing duration resulted in a much higher EPSC value with higher decay time. 10 to 30 spikes were found to be enough for short-term memory, while after 50 spikes (*p*)–FPS OFET achieved long-term memory with 1544 nA EPSC. A perceptron system was implemented using artificial synapses with an input layer, hidden layer, and output layer. The system detected handwritten digits, and the recognition rate increased significantly after 100 training epochs.

2.6 Conclusions

Organic semiconductors offer excellent advantages due to their unique features which makes them ideal candidates as the active layer for photo-sensing field-effect transistors. The architectural design of the device and the material selection for both the active layer and dielectric layer are very important points to be considered. Side-chain engineering and adding functional groups are being researched to improve organic semiconductors, and as a result, the performance of sensor devices has been advanced. Advantages are not limited to the chemical side of organic polymers. High-mobility, solution-processed semiconductors and thin and/or high-*k* dielectric layers are necessary to realize low-voltage devices that display superb electrical properties. Low-cost fabrication techniques and lightweight, flexible end products make OFETs an inevitable option for envisaging mass production. Organic phototransistors allow scientists to go further along with the new developments in sensor applications. Currently, artificial synapses based on OPTs have been studied and the focus on artificial synapses is on the rise due to their low energy consumption and fast response. On the other hand, research on mimicking the human brain enables the storage of information and memory functions, such as learning/forgetting. OPTs paving the way towards potential. They are promising devices for sensing visual activity, and soon, they can be utilized in human vision applications.

3. DESIGNING ZrO_2-BLENDED NANOCOMPOSITE MIM CAPACITORS FOR FUTURE OFET APPLICATIONS AND THEIR CHARACTERIZATIONS

3.1 Abstract

Organic field-effect transistors (OFETs) have been used for various sensor applications due to their excellent advantages over diodes and other electronic devices. Capacitors are one of the key components of the OFET designs that consist of two metal electrodes as parallel plates and a dielectric layer between the plates. The dielectric material should be thin and/or have a high-*k* constant value to achieve a high areal capacitance value (C_i), so more charge carriers can be accumulated at the interface between the dielectric and the organic semiconductor, and the device can operate under low voltage (< 3 V). It is also essential to fabricate a capacitor by using cost-effective techniques and at low temperatures. Solution processable dielectric materials allow to use of spin coating. In this study, high-*k* nanoparticles (NP), ZrO_2 metal oxide ceramic was blended with two different polymer matrixes, poly(vinylidene fluoride-co-hexafluoropropylene) (PVDF-HFP) and cyanoethyl cellulose (CEC) at varying concentrations (1, 1.5, 5, and 10 wt %) and occurred nanocomposite (NC) dielectrics were spin-coated on an aluminium evaporated glass substrate and annealed at 90 °C. The physical and electrical properties of fabricated metal insulator metal (MIM) capacitors were examined. It was seen that ZrO_2 NPs enhance the surface wettability of the CEC-based MIM devices (39.93° ± 1.82° for 5 wt % ZrO_2 in CEC). PVDF-HFP-based samples had hydrophobic surfaces even with ZrO_2 NPs inside of them. All capacitors show an amorphous structure in the tetragonal crystal structure. Capacitance values illustrated a gradual increase with rising ZrO_2 metal oxide content in the polymer matrixes. Pristine PVDF-HFP-based capacitors showed 38.2 ± 2.47 nF/cm^2, and areal C_i increased sharply to 91.86 ± 6.1 nF/cm^2 for 10 wt % ZrO_2 in PVDF-HFP. Similarly, areal capacitances were 52.36 ± 2.04 nF/cm^2 and 76 ± 3.03 nF/cm^2 at 1 kHz for CEC and 10 wt % ZrO_2 in CEC, respectively. The dielectric constants (*k*) were 28.61 ± 0.1 and 35.68 ± 1.99 for CEC + ZrO_2 (5 wt %)

and PVDF-HFP + ZrO_2 (5 wt %), respectively. Although leakage current density went up with the increased amount of NPs, All samples gave < 1.75×10^{-6} leakage current density (A/cm^2) at 2 V which is optimum and desirable for applications in sensor devices.

3.2 Introduction

Today, technological advancements bring huge innovation into the world of sensory devices. Organic field-effect transistors (OFETs) are one of the popular choices for sensor applications due to their low cost, easy fabrication conditions and good quality outcomes. Their three-electrode structure makes them the ideal candidate because of their ability to lower the noise and amplify the signal compared to diodes. The signal amplification feature is precious, especially for detecting biological signals which give low signals normally. Not only OFETs but also light-receiving OFETs or the most well-known name organic phototransistors (OPTs) can be adapted to various fields such as clinics, security, artificial synapses and environmental studies [164,230–235]. Several research studies have recently focused on low-power consumption, and operation under low-voltage (< 3 V) OPTs for biomedical and imaging applications. From ultraviolet light (UV light, ~ 300 nm) to near-infrared light (NIR light, ~ 700 nm – 900 nm) OPTs can detect the light in a large electromagnetic spectrum [236–241]. By endowing OFETs with biomolecules, biosensors can be created as well and OFET-based biosensors are also applied for distinctive areas like detecting disease biomarkers such as hormones, and proteins or sensing volatile organic compounds (VOCs) [242–244]. All these developments mean that large-area fabrication with cutting-edge technology is essential for OFET-based sensor applications. Therefore, the solution-processed technique has incredible importance, it is carried out at room temperature and is very cost-effective, an easy-to-use method [29,245]. Solution-processable, high-k dielectrics and organic semiconductors are desirable for research applications. Alternative dielectric layers are gaining attention for electronic applications over the traditional ones like SiO_2 [246,247] and another motivation is to use inorganic oxides to make high capacitance layers.

A dielectric layer is one of the main components of an OFET device since OFETs work under accumulation mode and the dielectric layer acts as a capacitor between the semiconductor and gate electrode. Capacitors are significant components of the sensor devices. High-*k* value and thin-thickness (*d*) dielectric material is the most desirable hence it gives high areal capacitance (C_i) that leads to high drain current (I_{DS}). Poly(vinylidene fluoride-co-hexafluoropropylene) (PVDF-HFP, $k \approx 11$) is one of the most used non-natural, ferroelectric, high-k dielectric materials [248].

Natural dielectric polymers have a huge advantage in using biotechnology and nanotechnology studies since they are biocompatible, biodegradable and have minimal toxicity towards the environment [249]. These studies are subfields of green electronics also known as bioelectronics. Biodegradable substrate and natural dielectric-based OFET devices can be used for drug delivery, biosensing, diagnostic, therapeutic applications and food packaging. Temporary body implants based on biodegradable OFETs can be used safely [186]. They waste low energy by using natural and sustainable polymers which are desirable high-*k* polymers since they can hinder harmful waste (e-waste) in nature and lead to the creation of eco-friendly electronics such as khaya gum and almond gum [184,250,251]. For instance, cashew gum (a main β-galactose (1→3) chain with branches of β-galactose (1→6) and terminal residues of glucuronic acid, arabinose, rhamnose, 4-O-methyl glucuronic acid, xylose, glucose, and mannose) (CG, $k \approx 38$) [185] dielectric solution is prepared just using distilled water, so it does not include any harsh chemical residue inside. Besides, cyanoethyl cellulose (CEC, $k \approx 14$) is the other popular choice for the dielectric layer because of its high *k*, high areal capacitance value and naturality [78]. Recently, natural, four kinds of Pinaceae pine resins have been researched for dielectric material [249].

Nanocomposites (NCs) are another good option to increase the areal capacitance value in that they are made of nanoparticle (NP) metal oxide materials and dielectric polymeric materials. It is the most common method to increase the *k* value of natural dielectric products [78,164]. A high-k nanocomposite dielectric layer allows the accumulation of more charge carriers at the interface, leading to a decrease in the operating voltage of the device. In the literature, Al_2O_3 [252], ZrO_2 [253], TiO_2 [254], and HfO_2 [255] can be compiled as potential candidates for metal oxide dielectric materials. TiO_2 [256] and ZrO_2 are the common candidates for biomedical applications related to their high biocompatibility. ZrO_2 has attracted much interest and is the most appealing one due to its thermal stability, biocompatibility, high bandgap (5.8 eV) energy and high permittivity ($k \approx 25$). These metal oxides can be fabricated using various strategies such as vacuum deposition, solution-processed deposition [257–259], and atomic deposition layer [252,260]. Fabrication techniques affect the morphology and microstructure of the given dielectric material. Dielectric layers suffer from expensive deposition methods that also apply high temperatures to form the layers which in turn come with a disadvantage related to the cost and effectiveness. The sol-gel method is a popular preferred technique to generate the metal oxide layer [253,261]. However, it requires a precursor chemical which adds a step more in the fabrication process and a high-temperature process to obtain a good film [262]. Another solution-process technique is spin-coating which offers advantages because of its easy-to-use operation, and suitability for large-areas and low-temperature conditions. After preparing a dielectric solution without any precursor chemical, just using nanoparticles and polymeric matrix and casting this solution via spin-coating decreases the cost and prohibits wasting time.

In addition, the low-temperature process makes using polymeric matrixes and organic semiconductors possible without degradation. Dielectric materials and organic semiconductors should be compatible with each other when their solvent and glass transition temperature (T_g) are taken into account. The high temperature of the annealing of the OSC can harm the quality of the dielectric layer which has low T_g. A dielectric layer should have adequate solvent resistance. Apart from that, a relatively high T_g is a good property for an OFET device if it is required to fabricate the device above room temperature. The interface between the dielectric and electrode and the dielectric and organic semiconductors in the metal-insulator-metal (MIM) and metal-insulator-semiconductor (MIS) structures can be affected negatively due to the high annealing temperature. Defects on the metal electrode and the dielectric, especially the oxygen vacancies induce a low capacitance value [263,264]. It is attractive and expected that by increasing the nanoparticle concentration, higher capacitance values can be reached [259]. On the other hand, high NP concentration raises an issue because it provokes a less smooth and non-uniform layer that inevitably gives higher leakage current density. Therefore, to keep the electrical quality of the device stable, the optimum concentration of NP and the most stable fabrication conditions become more of an issue.

Herein, we report a nanocomposite MIM capacitor (Figure 3.1a and 1b) based on two different polymeric matrixes (PVDF-HFP, CEC) (Figure 3.1c) blended with zirconium oxide nanoparticles (ZrO_2 NP) as dielectric solutions at varying concentrations (1, 1.5, 5, and 10 wt %).

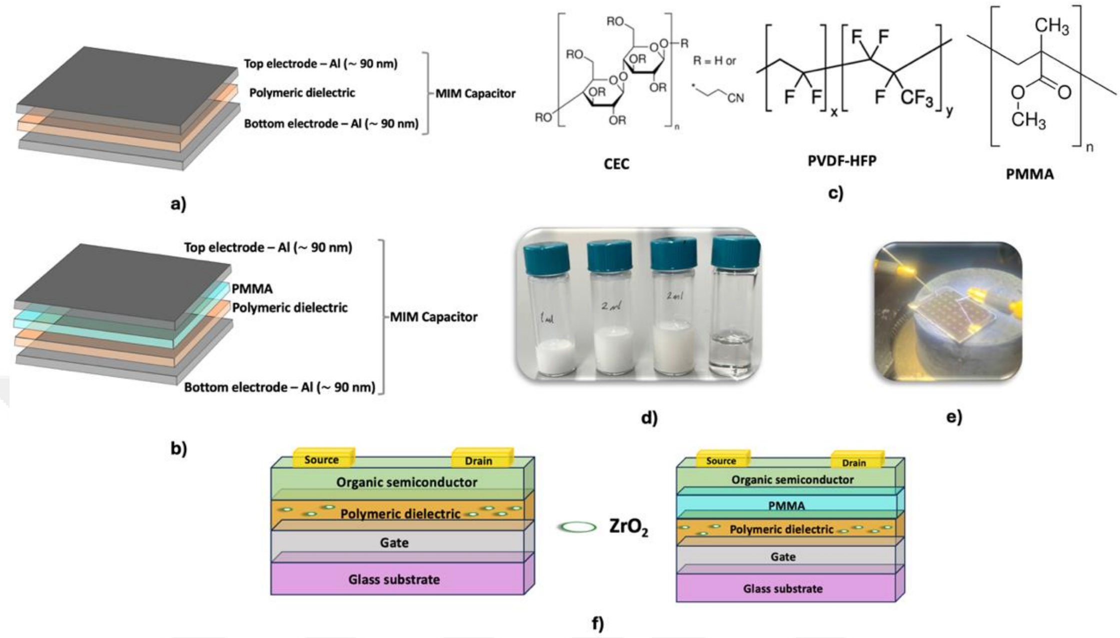

Figure 3.1 : Schematic of (a) and (b) MIM capacitor and PMMA coated MIM capacitor, respectively, (c) chemical structures of dielectric materials, poly(vinylidene fluoride-co-hexafluoropropylene), cyanoethyl cellulose and poly(methyl methacrylate), (d) dielectric solutions at different concentrations, (e) digital image of the capacitor, (f) OFET devices (BGTC) with and without PMMA layer.

Solution-processed polymer-nanoparticle dielectric layers were deposited by the spin-coating method. Al/Polymer-ZrO_2/Al MIM capacitors were fabricated, their physical characteristics were investigated, and electrical measurements were followed up. X-ray diffraction pattern demonstrated that nanocomposite dielectrics are amorphous and suitable to be used in capacitors. Areal C_i increased sharply to 91.86 ± 6.1 nF/cm^2 for 10 wt % ZrO_2 in PVDF-HFP. Similarly, the areal capacitance was 76 ± 3.03 nF/cm^2 at 1 kHz for 10 wt % ZrO_2 in CEC, respectively. Although leakage current density climbed with the increased amount of NPs, all samples gave <1.75x10^{-6} leakage current density (A/cm^2) at 2 V which is in sensor devices. We suggest that these blended nanocomposite dielectric layers are promising to have an impressive impact on OFET sensor applications.

3.3 Experimental Section

3.3.1 Chemicals and materials of MIM capacitors

Microscope glass slides (ISOLAB, Microscope Slides) were used as substrates. Acetone and isopropyl alcohol (IPA) (Sigma Aldrich) were the solvents used sequentially in the cleaning process. Aluminium wire was used as the source material in thermal evaporation for electrodes. Poly(vinylidene fluoride-co-hexafluoropropylene) ($(-CH_2CF_2-)_x[-CF_2CF(CF_3)-]_y$, pellets, d = 1.78 g / mL) and cyanoethyl cellulose ($C_{36}H_{46}N_8O_{11}$, M_w = 766.8 g/mol) (Figure 3.1d) were purchased from Sigma Aldrich. The solvent of the dielectric polymers was N, N-dimethylformamide (DMF) ($HCON(CH_3)_2$, M_w = 73.09 g/mol, Sigma Aldrich). Zirconium oxide nanopowder (ZrO_2, purity > 99.95 %, size = 30 nm) was from Nanografi Nano Technology. Poly(methyl methacrylate) (PMMA) ($[CH_2C(CH_3)(CO_2CH_3)]_n$, d = 1.18 g / mol, Alfa Aesar) as a passivation layer was dissolved in anisole solvent (Sigma Aldrich). Pre-patterned OFET's source and drain shadow masks (Channel length (L), 30 μm / width (W), 1000 μm) were purchased from Ossila Ltd.

3.3.2 Fabrication of MIM capacitors

Glass substrates (2 cm x 2 cm) had a two-stage solvent cleaning process. Solvents clean oils, dirt, and organic residues on glass and other base substrates. However, solvents can leave their residues, hence a two-stage solvent cleaning method is necessary. Glass substrates were placed in a beaker filled with solvents and rinsed in an ultrasonic bath for 10 minutes. Acetone and IPA were the solvents used sequentially in the cleaning process. At the end of each cycle, substrates were dried out by blowing N_2 gas and then put in the beaker which was filled with the next solvent. After completion of the cleaning process, samples were put on the hot plate at 80 °C for 10 minutes to dry off any remaining solvent (residue) and/or moisture. To make a metal/ insulator/metal (MIM) capacitor, Aluminium (Al) (~ 90 nm thickness) was deposited as the bottom electrode using thermal evaporation which is one of the methods of physical vapour deposition technique (PVD). PVDF-HFP (5 wt %) and CEC (5 wt %) were dissolved in DMF and stirred at 60 °C for 25 minutes and then filtered through a 0.45 μm PTFE filter [78,79]. Then PVDF-HFP and CEC were spin-coated on Al-coated glass substrates at 1000 rpm for 1 minute and 3500 rpm for 2 minutes, respectively. Samples were annealed at 90 °C for 90 minutes on the hot plate to evaporate residues. To observe the effect of the passivating layer, PMMA in anisole (1 wt %) was spin-coated at 2500 rpm for 1 minute on the CEC and PVDF-HFP coated samples and annealed at 90 °C for 1 hour. For nanocomposite samples, ZrO_2 nanopowder was added into CEC and PVDF-HFP dielectric solutions at different concentrations (1, 1.5, 5, 10 wt %) (Table 3.1). To obtain a uniform layer, solutions were stirred for at least 3 hours and ultrasonicated for 1 hour just before spin-coating. To complete the MIM capacitor, Al was evaporated using the mask as the top electrode of the capacitor.

Table 3.1 : Solution concentrations of the composition of MIM capacitors at different contents were given with their code names.

Sample	Content of polymer / nanoparticle in the solution (wt %)	Code
CEC	5	C
CEC / PMMA	5 / 1	CPMMA
CEC + ZrO_2 (1 wt %)	5 / 1	CZ1
CEC + ZrO_2 (1.5 wt %)	5 / 1.5	CZ1.5
CEC + ZrO_2 (5 wt %)	5 / 5	CZ5
CEC + ZrO_2 (10 wt %)	5 / 10	CZ10
PVDF-HFP	5	P
PVDF-HFP / PMMA	5 / 1	PPMMA
PVDF-HFP + ZrO_2 (1 wt %)	5 / 1	PZ1
PVDF-HFP + ZrO_2 (1.5 wt %)	5 / 1.5	PZ1.5
PVDF-HFP + ZrO_2 (5 wt %)	5 / 5	PZ5
PVDF-HFP + ZrO_2 (10 wt %)	5 / 10	PZ10

3.3.3 Characterization of MIM capacitors

The thickness of the obtained thin films was measured with a Bruker Dektak XT Stylus profilometer. X-ray diffraction analysis of the dielectric layers of samples was conducted using Powder diffractometer D8 Advance - Brucker X-ray diffraction spectrometer with Cu Kα radiation source and fast PSD detector (Lynxeye) at a wavelength of 1.5406Å at 40 kV voltage. The hydrophilicity of the dielectric layers of samples was examined using a Biolin Scientific Attension Theta Flex contact angle device. The areal capacitance values and dissipation factor of MIM samples were measured using an Agilent E4980A Precision LCR Meter (20 Hz – 2 MHz) under 100 mV DC voltage and 50 Hz – 1 MHz frequency range. Electrical measurements were carried out using a Probe station: Agilent Technologies E5270B 8 Slot Precision Measurement set.

3.4 Results and Discussion

3.4.1 X-ray diffraction and surface wettability (hydrophilicity)

X-ray diffraction patterns of dielectric layers (Figure 3.2a and b) presented with indices that at 2θ > 20° all dielectric layers exhibited an amorphous structure.

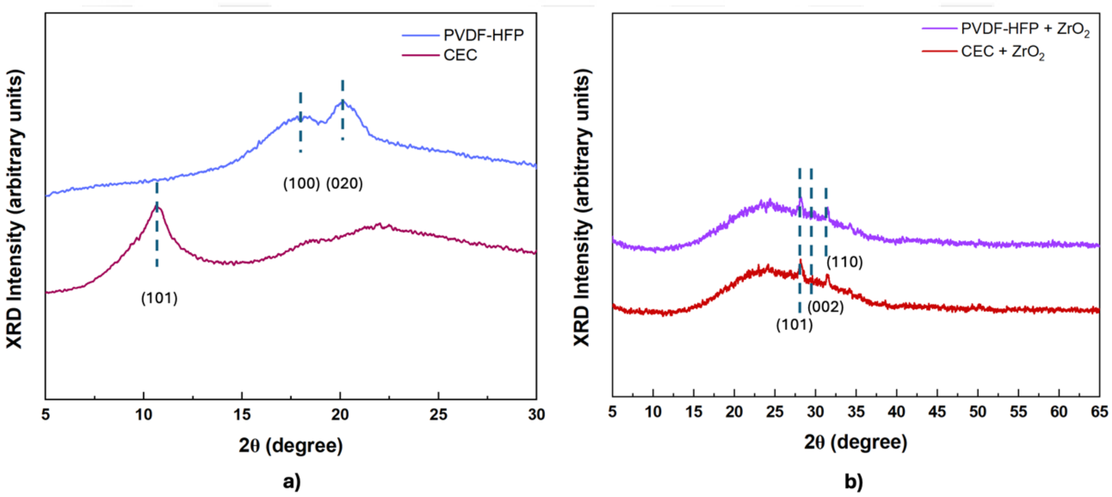

Figure 3.2 : (a) XRD pattern of pristine CEC and PDF-HFP dielectric layers, (b) XRD spectrum of nanocomposite dielectric layers.

Cyanoethyl cellulose peaked at 2θ = 10.7° (101) plane and PVDF-HFP at 2θ = 17.83° (100) and 20.25° and (020) planes, meaning they had slight crystalline regions rather than other degrees. Nanocomposite dielectric layers (PVDF-HFP + ZrO_2, PZ and CEC + ZrO_2, CZ) demonstrated the amorphous structure. They were in the tetragonal phases at (101), (002) and (110) indices as shown in the graph. The crystal structure of dielectric layers has a critical meaning in an OFET performance [265,266]. Dielectric material should be smooth, and the crystal structure of the layer should be as near as possible amorphous to eliminate undesired leakage current. In terms of designing the transistor structure, the connection of the dielectric layer to the channel layer through grain boundaries is not allowed. The dielectric layer is designed to create a separate layer from OSC to achieve a successful electrical performance, so there is no current flow to the gate electrode. If there is a tendency to charge the semiconductor layer from the dielectric layer, it gives a high off current in the off state of the transistor [185,249,267]. Additionally, surface roughness is a significant feature for organic semiconductor growth in transistor design. Low surface roughness and larger grains are the perfect match for the growth of the organic semiconductor layer. The existence of small grains means that there are lots of grain boundaries on the OSC surface which can cause a low charge mobility [267–269].

The surface energy and polarity are generally determined by surface wettability. Examining the surface wettability of the dielectric layers under dropped distilled water reported in this work, demonstrated hydrophobic surfaces with contact angles < 90° (Figure 3.3) for all the dielectric layers (Table 3.2). The surface energies of dielectric layers were calculated using the Owens-Wendt equation, by equation 3.1 and typical nonpolar liquid diiodomethane (DM) was assumed for calculation [59,60].

$$\gamma_l(1 + \cos\theta_l) = 2\left(\sqrt{\gamma_l^d \gamma_s^d} + \sqrt{\gamma_l^p \gamma_s^p}\right) \tag{3.1}$$

Where γ_l is the surface tension of the liquid, θ_l is the contact angle between the water droplet and the dielectric layer, γ_l^d and γ_s^d are the dispersive component of liquid and solid, respectively, γ_l^p and γ_s^p are polar component of liquid and solid, respectively.

Table 3.2 : Contact angle measurements and calculated surface energies of dielectric layers were given.

Dielectric	Contact angle (θ)	Surface energy, (γ_s) (mJ/m^2)	γ_s^p, (mJ/m^2)	γ_s^d, (mJ/m^2)	Surface roughness, (R_a, μm)
P	93.05° ± 1.15°	44.45	0.245	44.2	0.21 ± 0.07
PZ1	88.55° ± 0.64°	44.98	0.78	44.2	0.73 ± 0.25
PZ5	89.21° ± 1.92°	44.89	0.69	44.2	1.22 ± 0.5
C	63.79° ± 1.25°	53.13	8.93	44.2	0.52 ± 0.19
CZ1	51.9° ± 1.54°	59.63	15.43	44.2	0.19 ± 0.08
CZ5	39.93° ± 1.82°	65.95	21.75	44.2	0.4 ± 0.12

The surface wettability of dielectric materials was examined (Figure 3.3) and as expected the hydrophilic surfaces came from CEC (63.79° ± 1.25°) and its NC derivatives.

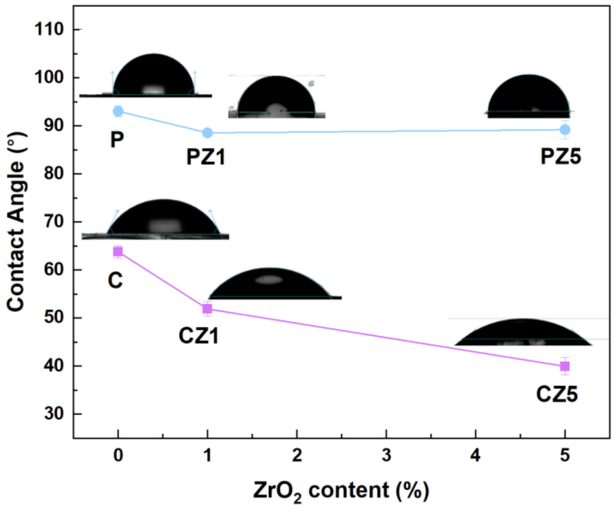

Figure 3.3 : Contact angle results of nanocomposite dielectric polymers.

CZ1 (51.9° ± 1.54°) and CZ5 (39.93° ± 1.82°) showed hydrophilic surfaces with a contact angle < 90° and the contact angle demonstrated a sharp decline as given in Figure 3.3. Besides, PVDF-HFP and PVDF-HFP-based NCs showed hydrophobic behaviour. The most hydrophobic surface belonged to the pristine PVDF-HFP (93.05° ± 1.15°) due to containing fluorine atoms in the chemical skeleton. The introduction of ZrO_2 nanoparticles didn't provide a notable effect on PZ1 (88.55° ± 0.64°) and PZ5 (89.21° ± 1.92°). However, NPs decreased the contact angle and contributed to the hydrophilicity of the CEC-based dielectrics. As the content of the ZrO_2 increased from 1 wt % to 5 wt %, the hydrophilicity of the layer enhanced gradually. A smooth and hydrophobic dielectric layer with low surface energy and growth of OSC in the form of larger grains offers low leakage current and exhibits low hysteresis with low trap density. The interface between the semiconductor and the dielectric is a critical factor in determining charge carrier mobility in OFET devices [268,270]. Hydrophilic surfaces generally act as charge carrier traps, especially when solution-based organic semiconductors are deposited upon organic dielectric in organic field-effect transistors. Hydrophilic dielectrics can absorb moisture and degrade. As a result, device stability can be degraded. Apart from that, a high surface energy dielectric surface can lead to the formation of a larger grain size of the OSC layer. It can cause low-charge carrier mobility due to the decreased interconnectivity of the grains. In most of these cases, the gate dielectrics require some surface passivation treatment to enhance the performance of the device. Some strategies are developed to achieve high mobility and a high on/off ratio. Solutions can be compiled as blending the hydrophilic polymer with a low k material, and surface treatment of the dielectric layer with octadecyltrichlorosilane (OTS) to decrease the surface energy [251,271]. On the other hand, for the bottom-gate designs, it is necessary to grow an OSC layer on top of the dielectric layer, or for the top-gate configurations, a passivation layer needs to be applied [255,270]. Therefore, a hydrophilic surface of the dielectric material can satisfy these requirements. Faraji et. al. established a DPPTTT/PMMA blend as an OSC layer on the natural cashew gum dielectric, without applying any additional surface treatment [185]. The hydrophilicity of the cashew gum ($\theta = 46°$ at $t = 30$ s) allowed PMMA to go down, below the DPPDTT. So, they facilitated a smooth, modified dielectric layer surface.

The surface roughness values (R_a) of the dielectric layers were investigated by an optical profilometer and given in Table 3.2. For PVDF-HFP samples, it was observed that introducing NPs made the surface of dielectric films less smooth, with PZ5 thin films being the roughest of all. Introducing nanoparticles into a polymer matrix creates peaks and valleys in the thin film. CEC-based nanocomposite layers had less rough surface compared to their PVDF-HFP-based counterparts. This is in line with the increased surface wettability and hydrophobicity of CEC-nanocomposite dielectric layers for higher NP loadings. For CEC samples, addition of 1 wt% ZrO_2 reduced surface roughness compared to pristine CZ sample. However, as expected CZ5 had a rougher surface than CZ1. It appears that the choice of polymer base can impact the uniformity and surface roughness of the deposited thin films.

One possible explanation for reduced roughness for CZ1 compared to CZ could be that the latter has a crystalline structure which contributes to higher surface roughness, while addition of NPs results in reduced crystallinity and surface roughness in the former. Further increase in NP content would inevitably increase roughness due to denser packing and creation of cluster of nanoparticles. Some agglomeration of nanoparticles and non-homogeneity in nanocomposite suspension may cause non-uniformity and high surface roughness of the thin layer. Therefore, optimisation of nanocomposite preparation, such as longer stirring duration, filtration and nanoparticles' surface modification should be considered to minimise the non-uniformity of deposited thin films.

SEM images of nanocomposite dielectric thin films are shown in Figure 3.4. It was indicated clearly that 1 wt % and 5 wt % ZrO_2 nanoparticles were blended successfully in polymer matrixes CEC and PVDF-HFP.

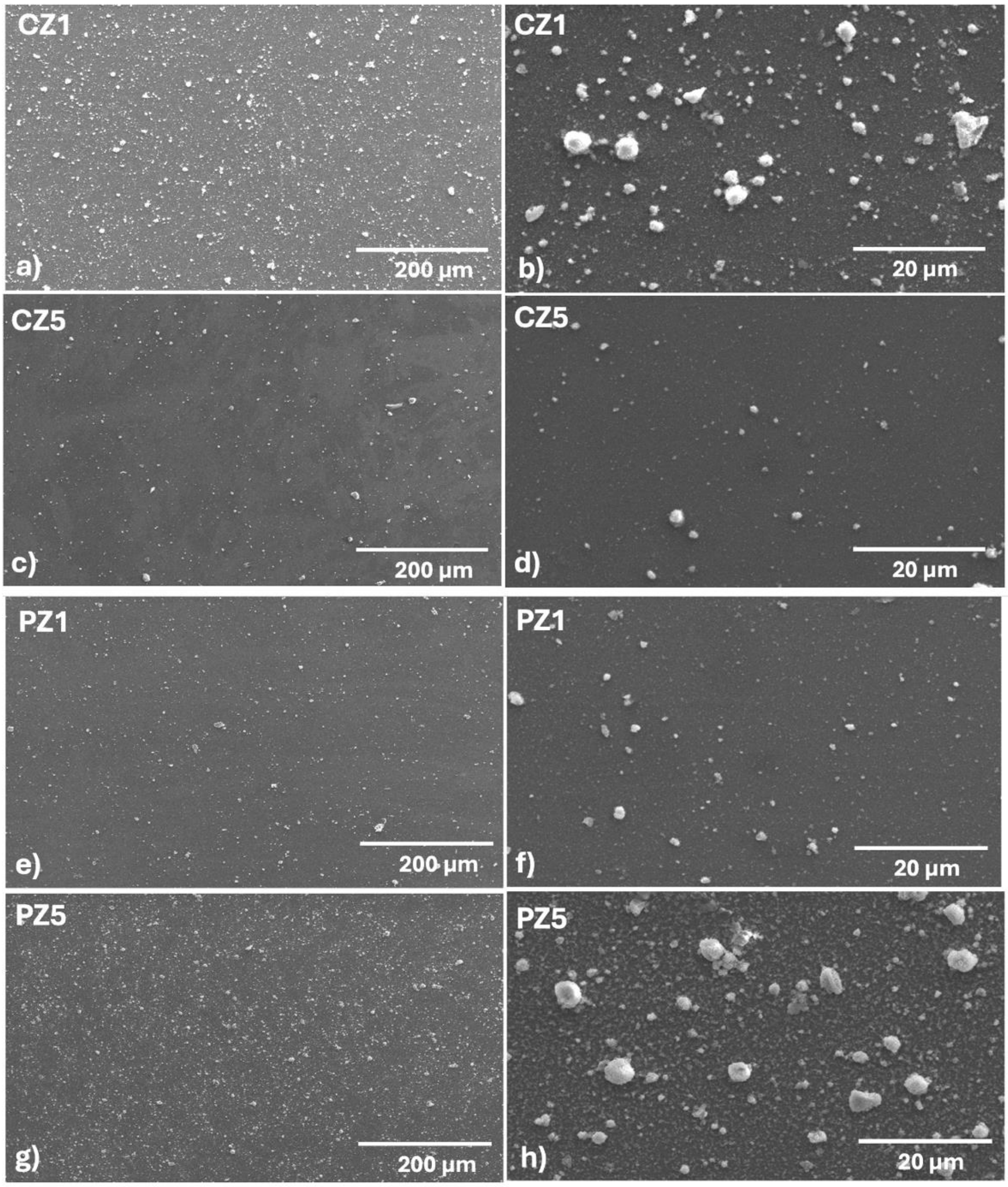

Figure 3.4 : SEM images of nanocomposite dielectric thin films with varying ZrO_2 concentrations (1 wt % (CZ1 and PZ1) and 5 wt % (CZ5 and PZ5)) in CEC and PVDF-HFP matrixes, respectively.

3.4.2 Electrical characterizations of MIM capacitors

MIM capacitors were fabricated and the areal capacitance values of capacitor samples as a function of the frequency range are shown in Figure 3.5 and b.

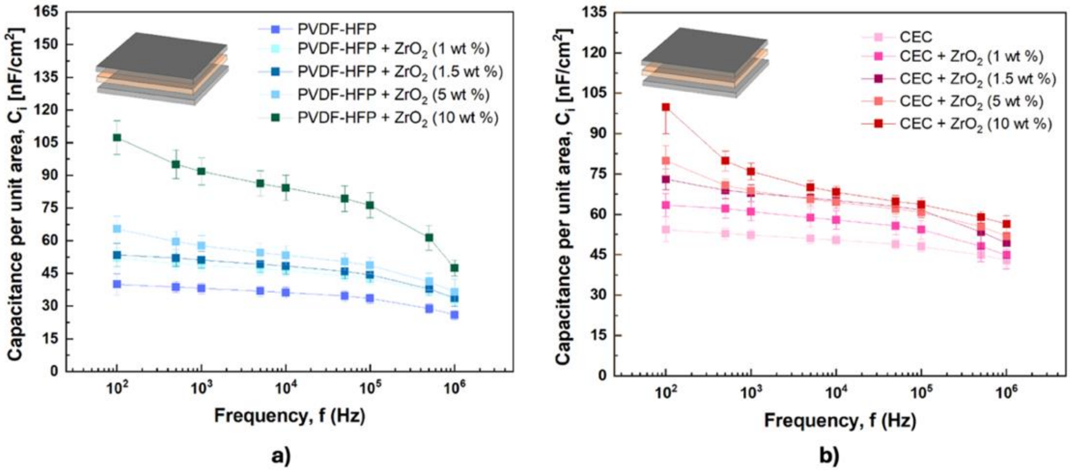

Figure 3.5 : Comparative graphs of areal capacitance values (C_i, nF/cm^2) versus frequency (Hz) of (a) CEC-ZrO_2 and (b) PVDF-HFP-ZrO_2 nanocomposite capacitors at different ZrO_2 concentrations.

Pristine polymers for both PVDF-HFP and CEC illustrated the lowest capacitance values than that of the nanocomposite forms of polymeric matrixes. While the ZrO_2 nanoparticles were induced at different concentrations up to 10 wt %, capacitance values showed a dramatic increase from 38.2 ± 2.47 nF/cm^2 to 91.86 ± 6.1 nF/cm^2 at 1 kHz for P and PZ10 (Figure 3.5a), respectively and from 52.36 ± 2.04 nF/cm^2 to 76 ± 3.03 nF/cm^2 at 1 kHz for C and CZ10 (Figure 3.5b), respectively. 1 wt % and 10 wt % ZrO_2 concentrations were examined for the consideration of the extreme points. ZrO_2 at 1.5 wt % concentration in the MIM capacitor didn't make a remarkable difference in the capacitance results (51.23 ± 3.87 nF/cm^2 PZ1.5 and 66.4 ± 2.61 nF/cm^2 CZ1.5 at 1 kHz) when compared to capacitance values at 1 wt % concentration of ZrO_2 for PZ1 (48.91 ± 2.97 nF/cm^2 at 1 kHz) and 5 wt % concentration of ZrO_2 for CZ5 (68.85 ± 2.16 nF/cm^2 at 1 kHz). A slight increase in the nanoparticle amount from 1 wt % to 1.5 wt % didn't have a huge impact on capacitance values in the PVDF-HFP matrix as expected. It shows this matrix was in line with the direct proportion of nanoparticle amount. One of the extreme points, PZ10 included 10 wt % ZrO_2 and demonstrated a sharp rise after PZ5 (57.79 ± 4.65 nF/cm^2 at 1 kHz) which was the highest result. CEC-derivative samples presented a similar trend and gave a direct proportional response to the nanoparticle amount. After introducing nanoparticles, the lowest value belonged to the pristine polymer (C) and capacitance values went up. Surprisingly, CZ1.5 and CZ5 showed nearly the same results. This can be attributed to the nature of the CEC polymer and the non-dispersion feature of the NPs. An undesirable aggregation of some ZrO_2 particles can cause a non-uniform NC layer.

Probing the capacitor by touching the points of that layer can give higher results than expected. Therefore, a negligible difference of CZ5 and CZ1.5 capacitance values was observed. The areal capacitance values for all samples decreased gradually throughout the increased frequency. C_i values at low frequencies were higher than those at high frequencies (> 10^4 Hz). At high-frequency levels, capacitors can't have enough time to polarise fully and can't align with the electrical field. Consequently, the capacitance values drop moderately. Another explanation for high C_i values at low frequencies can be the interfacial polarization mechanism at the 10^2 – 10^3 Hz frequency range that arises from the partially mobile charge carriers under the applied electrical field [184,185]. The dissipation factors (DF) of the MIM devices are given in Figure 3.6a and b. DF factor is the power loss of the capacitor when the voltage is applied to the capacitor [272]. It should be close to zero showing the electrical stability of the device. It is seen from the graphs that the DF factor for all samples wasn't zero which means it is not an ideal electrical behaviour.

However, it can be said that DF values followed a steady regime from 100 Hz to 10^5 Hz frequency range, around 0.04 ± 0.003, nearly zero at 1 kHz frequency, and finally reached 0.31 ± 0.08 at 1 MHz for PZ5. CZ samples displayed reverse behaviour at low frequency (< 10^3 Hz). First, they had high DF, then showed a reduction from 0.30 ± 0.08 and remained stable around 0.15 ± 0.02 at 1 kHz for CZ5.

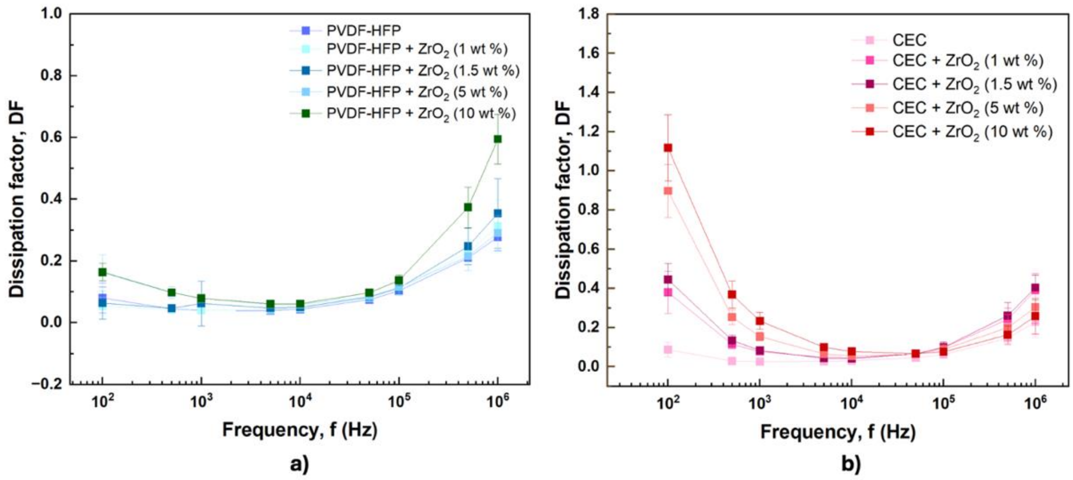

Figure 3.6 : Comparative graphs of dissipation factor (DF) values versus frequency (Hz) of (a) CEC-ZrO_2 and (b) PVDF-HFP-ZrO_2 nanocomposite capacitors at different ZrO_2 concentrations.

Capacitance values should be stable when the voltage is applied. Figure 3.7a and b depict measured areal capacitance values at 1 kHz frequency versus applied voltage at a specific range for PVDF-HFP-based nanocomposite capacitors and CEC-based nanocomposite capacitors. When the bias voltage was applied from – 3 V to 3 V (interval 0.5 V), C_i values remained stable for all samples. This behaviour ensures the reliability of a capacitor for an OFET device [273].

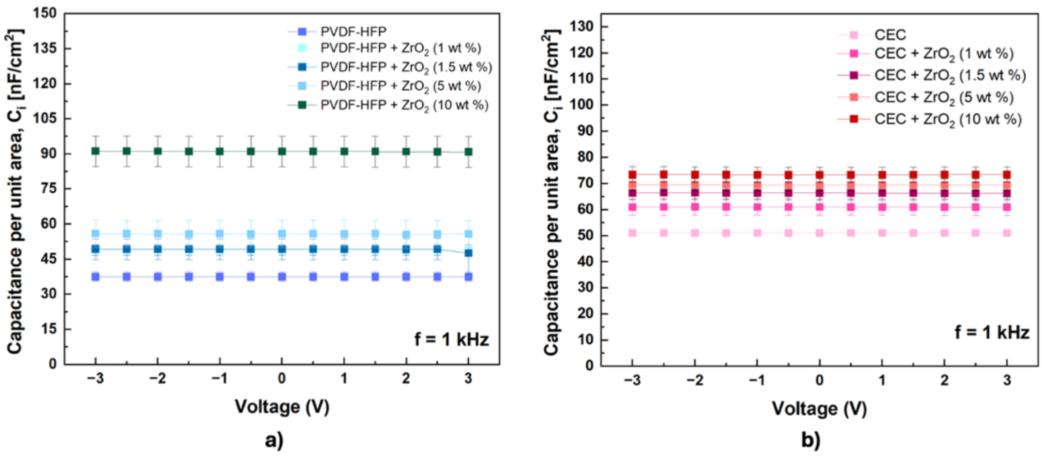

Figure 3.7 : Comparative graphs of areal capacitance values (C_i, nF/cm^2) versus voltage (V) of (a) CEC-ZrO_2 and (b) PVDF-HFP-ZrO_2 nanocomposite capacitors at different ZrO_2 concentrations at 1 kHz frequency.

PMMA was coated as a passivating layer to hinder the high dielectric leakage current of the MIM structures. PPMMA and CPMMA-based MIM capacitors were electrically examined to evaluate the impact of the PMMA capping layer on the all-over performance of capacitors. The C_i and DF values as a function of frequency and C_i versus applied voltage measured on PMMA-capped pristine PVDF-HFP and CEC are displayed. The obtained electrical measurement data of the corresponding devices are plotted in Figure 3.8a, b and c. Comparative results of the areal capacitance of samples are displayed in Figure 3.9b.

PPMMA (32.85 ± 1.17 nF/cm^2 at 1 kHz) and CPMMA (48.81 ± 1.53 nF/cm^2 at 1 kHz) capacitors had lower areal capacitance due to an additional layer in the dielectric. Interestingly, their leakage currents didn't go down (PPMMA, 8.96x10^{-7} A/cm^2 and CPMMA, 3.8x10^{-7} A/cm^2 at 2 V) even after applying the PMMA layer on top of the polymeric dielectric layer. A possible reason can be attributed to the unsuccessful physical crosslinking between polymers and the PMMA layer. Different molar concentrations can be applied to develop an optimal result [274].

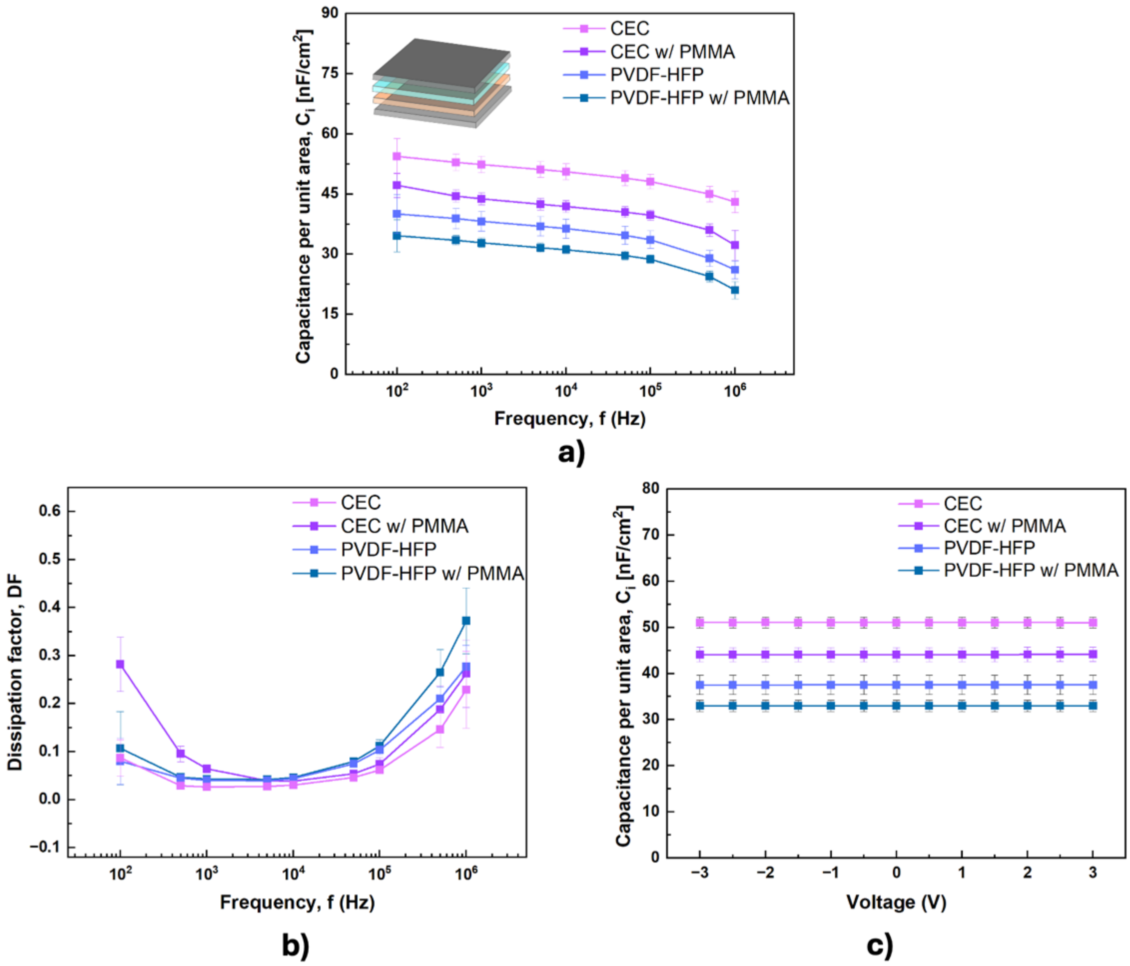

Figure 3.8 : Comparative graphs of (a) areal capacitance values (C_i, nF/cm^2) versus frequency (Hz), (b) dissipation factor (DF) values versus frequency (Hz), (c) areal capacitance values (C_i, nF/cm^2) versus voltage (V) of CEC and CEC with PMMA and PVDF-HFP and PVDF-HFP PMMA capacitors.

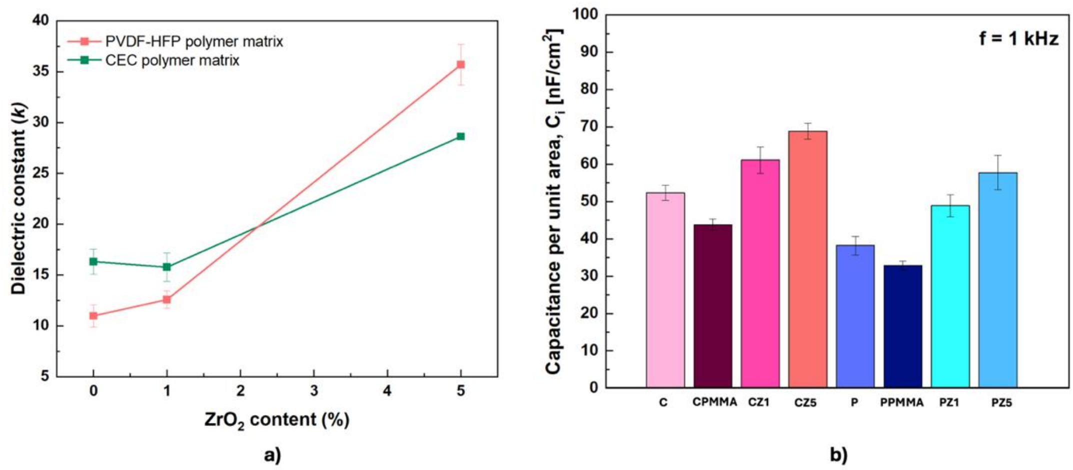

Figure 3.9 : (a) Calculated dielectric constants (k) of C, CZ1, CZ5 in green, P, PZ1, PZ5 in orange versus ZrO_2 concentrations (wt %), (b) Comparative graph of areal capacitance values of nanocomposite dielectrics at 1 kHz frequency.

Table 3.3 summarises the areal capacitance values of samples with leakage current densities and calculated k values of the NC layers. The dielectric constant (*k*) (Table 3.3, Figure 3.9a) climbed from 16.31 ± 1.22 (CEC) to 28.61 ± 0.1 (CZ5), considerably. Similarly, P5 presented an increased trend significantly from 10.98 ± 1.09 (P) to 35.68 ± 1.99 (PZ5). 5 wt % ZrO_2 improved *k* value three times higher than that of pristine PVDF-HFP capacitor.

Table 3.3 : Areal capacitance values with leakage current densities, thicknesses of films and k values were shown for each nanocomposite dielectric layer.

Sample code	**Areal capacitance value (C_i, nF/cm^2) at 1 kHz**	**Leakage current density, J (A/cm^2) at 2 V**	**Thickness, d (nm)**	**Permittivity value, k**
C	52.36 ± 2.04	3.12 x 10^{-7}	276.32 ± 6.76	16.31 ± 1.22
CZ1	61.11 ± 3.51	2.62 x 10^{-6}	228.31 ± 6.45	15.76 ± 1.38
CZ5	68.85 ± 2.16	9.58 x 10^{-8}	367.85 ± 1.41	28.61 ± 0.1
P	38.2 ± 2.47	1.98 x 10^{-8}	254.47 ± 5.39	10.98 ± 1.09
PZ1	48.91 ± 2.97	2.66 x 10^{-7}	227.57 ± 5.54	12.57 ± 0.85
PZ5	57.79 ± 4.65	2.05 x 10^{-6}	546.43 ± 15.5	35.68 ± 1.99

Even in an ideal device, a small leakage current flows through the dielectric related to the applied electrical field, hence dielectric material and characterisation of the capacitors are significant for evaluating the quality of the device [270]. Typically, < 10^{-6} A/cm^2 leakage current density for capacitors can be acceptable for an application in a semiconductor device. It is known that thin dielectric layers can cause a high leakage current density. Apart from that, the high roughness of the NC surface can lead to a leakage current. Although the high amount of nanoparticles led to increased capacitance value, due to the non-disperse nature of the particles it is not simple to obtain a homogenous solution. That causes a high leakage current density and decreases the performance of the capacitors [259]. Asymmetry leakage current curves (Figure 3.10) of the samples were due to different interfaces of the NC dielectric layers. PZ10 and CZ10, including the highest ZrO_2 content capacitors as shown in Figure 3.10 showed the highest leakage current densities, 5.53x10^{-6} A/cm^2 and 1.75x10^{-6} A/cm^2, respectively. CZ5 MIM capacitor had the lowest leakage current density (9.58x10^{-8}) at 2 V. It can be attributed to the physical crosslinking between residual hydroxyl groups (−OH) of CEC and metal oxides. Residual hydroxyl groups are the dominant factor of the leakage current in the device. They create trap sites for charge carriers inside and on the surface of the dielectric layer. Hence, the physical crosslinking in the nanocomposite MIM capacitors improves the electrical performance of the devices [259].

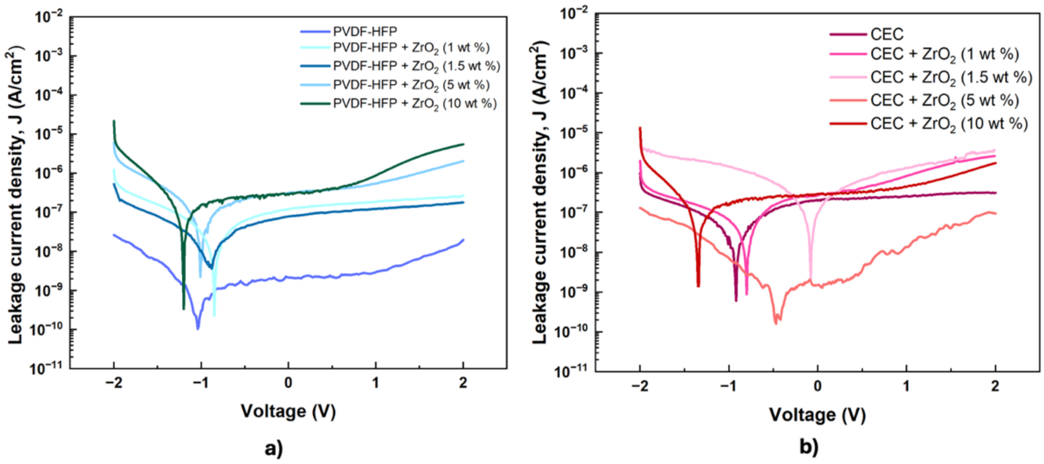

Figure 3.10 : Comparative graphs of leakage current density values (J, A/cm^2) versus voltage (V) of (a) CEC-ZrO_2 and (b) PVDF-HFP-ZrO_2 nanocomposite capacitors at different ZrO_2 concentrations.

Leakage current values were comparable to those reported in the literature [253,258,261,275]. However, these studies achieved low leakage current densities (< 10^{-6} A/cm^2) at high-temperature (> 300°) annealing conditions or by UV treatment. In this study, solution-processed, low-temperature annealed, spin-coated NC dielectric layers in a polymer matrix at room temperature offer a novelty and an advantage over other studies.

3.5 Conclusion

In this study, polymer-nanoparticle dielectric design in a MIM capacitor at varying concentrations (1, 1.5, 5, and 10 wt %) was investigated using metal oxide ZrO_2 nanoparticles (size = 30 nm) and two different polymeric matrixes; one is synthetic copolymer PVDF-HFP and the other one is a cellulose-based polymer (CEC). The XRD pattern showed nanocomposite dielectric layers had an amorphous structure and contact angle results presented that CEC-based nanocomposite dielectrics (CEC (63.79° ± 1.25°) and its NC derivatives CZ1 (51.9° ± 1.54°) and CZ5 (39.93° ± 1.82°)) were inclined to be more hydrophilic as the nanoparticle concentration increased. In contrast, PVDF-HFP-based dielectrics continued to be hydrophobic (93.05° ± 1.15° and 89.21° ± 1.92° for pristine PVDF-HFP and PZ5, respectively) without any remarkable change while inducing nanoparticles. Areal capacitance values displayed that nanocomposite design improved the performance of the capacitor rather than pristine dielectric layers. As the concentration of the nanoparticles increased in the polymeric matrix, capacitance values arose. However, the leakage current increased due to the roughness of the nanocomposite layer, it was an acceptable range that the highest leakage current density was 1.75×10^{-6} A/cm^2 from CZ10. Results indicated that PVDF-HFP is more suitable because of its high C_i value and hydrophobic structure compared to the CEC polymeric matrix. 5 % wt ZrO_2 can be the optimum content for two dielectrics, C_i of CZ5 is 68.85 ± 2.16 nF/cm^2 and PZ5 is 57.79 ± 4.65 nF/cm^2 at 1 kHz. The dielectric constants (*k*) were 28.61 ± 0.1 and 35.68 ± 1.99 for CEC + ZrO_2 (5 wt %) and PVDF-HFP + ZrO_2 (5 wt %), respectively. In conclusion, this study sheds light on novel dielectric studies with cost-effective, solution-processed techniques at low-temperature fabrication without applying high annealing temperatures. NC dielectric layers in the form of polymer – nanoparticle using metal oxide ceramics will soon create a new page on the studies of low-operate voltage OFETs.

4. NATURAL DIELECTRIC-BASED MIM CAPACITORS AND OFET DEVICES

4.1 Abstract

Eco-friendly solutions using natural, bioorganic materials to design electronic sensors provide a new chapter for electronic devices in our green future. Natural, biocompatible, biodegradable materials with low-cost fabrication techniques such as solution processes have been utilised in organic field-effect transistors (OFETs). In this chapter mango sap and cactus sap materials were examined as natural dielectric materials in metal/insulator/metal (MIM) structures. They were in sap form and applied directly without using solvent or distilled water. Dielectrics were spin-coted at different spin speeds; 2500 rpm and 2000 rpm were applied for mango sap, 1000 rpm was for cactus sap and 3000 rpm was for aloe vera. Organic semiconductors were spin-coated on the top of the dielectric layers under N_2. Bottom gate – top contact (BGTC) configuration was designed in OFET devices. It was seen that mango sap dielectric thicknesses influenced the areal capacitance (C_i) values of the MIM capacitors that the thinner layer (spin speed = 2500 rpm) had a 30 % higher value (42.56 ± 5.29 nF/cm^2 at 1 kHz). Leakage current densities were 3.64x10^{-7} A/cm^2 at 2 V for mango sap coated at 2500 rpm, and 6.88x10^{-7} A/cm^2 at 2 V for mango sap coated at 2000 rpm. Cactus sap was used as a dielectric layer with a PMMA passivating layer and gave 93.53 ± 8.23 nF/cm^2 areal capacitance at 1 kHz with < 10^{-6} A/cm^2 leakage current densities. BTz-based-OFET devices couldn't demonstrate OFET device properties. DPP-DTT:PMMA-based OFET devices showed ~ 10 on/off ratios for mango sap-based devices and 3.5x10^3 on/off ratios for aloe vera-based devices. Aloe vera dielectric-based devices demonstrated low leakage current densities (< 10^{-8} A/cm^2 at 2 V) with high mobilities (μ_{sat}=0.6 ± 0.1 cm^2 /Vs of aloe vera + PMMA-based devices).

4.2 Introduction

Organic field-effect transistors (OFETs) are attractive designs for sensor applications. Their three-electrode structure gives them a huge advantage over other electronic devices due to their ability to decrease noise and amplify the signal [29,30]. The urge for the sustainability of nature using OFET sensors has led to the creation of eco-friendly resolutions. Natural dielectrics and solution-processed organic semiconductors with biodegradable substrates provide reasonable solutions for electronic sensors. Hence, natural, biocompatible, biodegradable materials and low-cost fabrication techniques such as solution processes have been preferred [186,249]. A variety of natural materials like aloe vera, deoxyribonucleic acid (DNA), silk, cellulose derivatives, paper, and resins can be compiled as green materials for electronic sensors. Aloe vera is one of the significant and distinguished candidates in bioorganic materials for sensor devices. It has been used in the medicine and the food industry for a long time due to its antimicrobial activity. The most excellent point is that biopolymer dielectrics do not dissolve in toxic solvents, and they can be used directly in a gum or sap form after cropping them. In general, these materials are in sap form, and some of them are dissolved in distilled water such as cashew gum, almond gum and khaya gum [184,185,251]. They can be deposited via solution-processed techniques which are cost-friendly ways to coat and can be carried out even at room temperature without any complex equipment. For instance, biomedical sensors require long wavelengths to reach cells in the vein. Otherwise, this light can be scattered before collecting enough data from the tissue. Biopolymers have brought new insight into the biomedical field in terms of making biodegradable sensors for in vivo implant applications. Energy harvesting and security areas benefit from OFET-based sensors, too. A variety range of application areas show the importance of developing more nature-friendly sensors to contribute to our green future.

The chemical functionality of organic semiconductors allows scientists to make different bandgaps that can be special for the usage aim. Adjusting the band gap for the aim of the study, tailoring the HOMO – LUMO level and improving the chemical structure via modifying with functional groups and/or side chains can be compiled as excellent features over the conventional semiconductors. Donor and acceptor organic polymers can be used together to facilitate molecular planarity, $\pi - \pi$ stacking, and arranging the HOMO – LUMO level and band gap. Side-chain engineering is the essential case; by introducing alkyl chains, the solubility of the polymer increases which in turn is an amazing feature for solution-processed OSCs [276–278]. By inducing H bonding, dipole – dipole interactions, and Van der Walls forces between donor and acceptor units, molecular planarity can be facilitated [229,233,276,279]. Benzotriazole-based polymers are generally preferred acceptor units [280,281] because they allow three different positions for adding electronegative atoms where two of them are in the bottom of the ring, and another one can be added instead of the H atom which is bonded to the N atom. Thiophene is an excellent π-conjugated aromatic molecule for designing donor units and allows alkyl chain addition into its skeleton [279,282,283]. Although this design of OSC is attractive, it is required to study with a suitable solvent and anneal this kind of OSC polymers at low temperatures to hinder any possible degradation of the polymeric dielectric layers.

Herein, we report the physical and electrical properties of natural materials-based MIM capacitors and OFET devices (Figure 4.1). Mango sap, cactus sap and aloe vera were examined as dielectric materials, and they were used in MIM capacitors. All dielectrics and OSCs were spin-coated and metal electrodes (Al and Au) were deposited using thermal evaporation. Capacitors with mango sap dielectric coated at 2500 rpm showed 42.56 ± 5.29 nF/cm^2 areal capacitance at 1 kHz, a 30 % more value (29.7 ± 2.99 nF/cm^2 at 1 kHz) than that of coated at 2000 rpm. Capacitors with cactus sap dielectric with PMMA passivating layer presented 93.53 ± 8.23 nF/cm^2 areal capacitance value with < 10^{-6} A/cm^2 leakage current densities. The best capacitor and OFET results were from aloe vera dielectric-based devices. 85.72 ± 1.46 nF/cm^2 areal capacitance value**,** 0.6 ± 0.1 cm^2/Vs charge carrier mobility (μ_{sat}) and – 1.05 threshold voltage (V_{th}) were observed for aloe vera + PMMA-based devices.

DPP-DTT (1 wt %) and BTz-based OSCs (1 wt %) were spin-coated on the dielectric layer for OFET devices. Their output and transfer characteristics were evaluated. BTz-based-OFET devices regardless of the dielectric layer couldn't demonstrate OFET device requirements. DPP-DTT:PMMA-based OFET devices achieved ~ 10, 2.7x10^3 and 3.5x10^3 on/off ratios for natural mango sap dielectric-based devices, aloe vera dielectric-based devices and aloe vera-coated PMMA dielectrsFieldd1 devices, respectively.

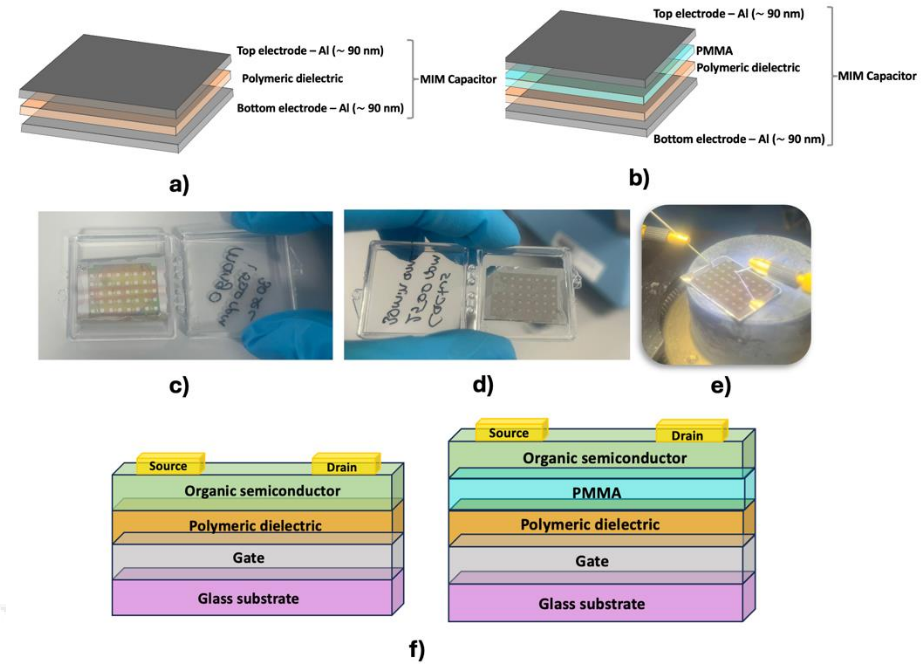

Figure 4.1 : Schematic of (a) and (b) MIM capacitor and PMMA coated MIM capacitor, respectively, (c) fabricated mango-based MIM capacitor, (d) fabricated cactus-based MIM capacitor, (e) capacitance measurement using probes, (f) OFET devices (BGTC) with and without PMMA layer.

4.3 Experimental Section

4.3.1 Chemicals and materials of MIM capacitors and OFET devices

Microscope glass slides (ISOLAB, Microscope Slides) were used as substrates. Acetone and isopropyl alcohol (IPA) (Sigma Aldrich) were the solvents used sequentially in the cleaning process. Aluminium wire was used as the source material in thermal evaporation for electrodes. As natural dielectric materials, mango sap and cactus sap were extracted directly from trees in Senegal. Aloe Vera gel obtained from the Aloe barbadensis Miller plant was diluted in deionised water and filtered to form a homogenous 1 % w/v solution. Poly(methyl methacrylate) (PMMA) ($[CH_2C(CH_3)(CO_2CH_3)]_n$, d = 1.18 g/mol, Alfa Aesar) as a passivation layer was dissolved in anisole solvent (Sigma Aldrich). As organic semiconductors, PP(C14)DTBTz(HD) and PP(C14)DTFBTz(HD) were synthesized and dissolved in chloroform solvent. The commercial one, Poly[2,5-(2-octyldodecyl)-3,6-diketopyrrolopyrrole-alt-5,5-(2,5-di(thien-2-yl)thieno [3,2-b]thiophene)] (DPP-DTT, Ossila) was dissolved in chloroform. Pre-patterned OFET's source and drain shadow masks (Channel length (L), 30 µm / width (W), 1000 µm) were purchased from Ossila Ltd.

4.3.2 Fabrication of MIM capacitors and OFET devices

Glass substrates (2 cm x 2 cm) had a two-stage solvent cleaning process. Solvents clean oils, dirt, and organic residues on glass and other base substrates. However, solvents can leave their residues, hence a two-stage solvent cleaning method is necessary. Glass substrates were placed in a beaker filled with solvents and rinsed in an ultrasonic bath for 10 minutes. Acetone and IPA were the solvents used sequentially in the cleaning process. At the end of each cycle, substrates were dried out by blowing N_2 gas and then put in the beaker which was filled with the next solvent. After completion of the cleaning process, samples were put on the hot plate at 80 °C for 10 minutes to dry off any remaining solvent (residue) and/or moisture. To make a metal/ insulator/metal (MIM) capacitor, Aluminium (Al) (~ 90 nm thickness) was deposited as the bottom electrode using thermal evaporation which is one of the methods of physical vapour deposition technique (PVD). Mango sap was spin-coated at 2000 rpm and 2500 rpm for 1 minute on Al-coated glass substrates. Cactus sap was spin-coated at 1000 rpm for 1 minute on Al-coated glass substrates. Aloe vera was spin-coated at 3000 rpm for 30 seconds on Al-coated glass substrates. Mango sap dielectric-based samples were annealed at 100 °C for 15 minutes, cactus sap dielectric-based samples were annealed at 100 °C for 35 minutes and aloe vera dielectric-based samples were annealed at 80 °C for 30 minutes on the hot plate under ambient conditions. To make a passivating layer, PMMA in anisole (1 wt %) was spin-coated at 2500 rpm for 1 minute on the cactus sap dielectric samples and annealed at 90 °C for 1 hour. To complete the MIM capacitor, Al was evaporated using the mask as the top electrode of the capacitor. To make BGTC OFET devices, DPP-DTT:PMMA (1 wt %) semiconductor layer was prepared at a 7:3 volume ratio in chloroform. PP(C14)DTBTz(HD) and PP(C14)DTFBTz(HD) OSCs (1 wt %) were dissolved in chloroform and stirred for 15 minutes at 40 °C. Organic semiconductors were spin-coated on the dielectric layer at 2000 rpm for 2 minutes and annealed at 90 °C for 2 hours under N_2. Following that gold (Au) metal (~ 40 nm thickness) was evaporated on the organic semiconductor layer using a source and drain mask under thermal evaporation.

4.3.3 Characterization of MIM capacitors and OFET devices

The optical properties of organic semiconductor polymers were detected using Agilent Cary Eclipse UV-Vis spectrometer device. X-ray diffraction analysis of the BTz-based organic semiconductors was conducted using Powder diffractometer D8 Advance - Brucker X-ray diffraction spectrometer with Cu Kα radiation source and fast PSD detector (Lynxeye) at a wavelength of 1.5406Å at 40 kV voltage. The areal capacitance values and dissipation factor of MIM samples were measured using an Agilent E4980A Precision LCR Meter (20 Hz – 2 MHz) under 100 mV DC voltage and 50 Hz – 1 MHz frequency range. Electrical measurements for I-V curves of OFET devices were carried out using a Probe station: Agilent Technologies E5270B 8 Slot Precision Measurement set. All electrical characterizations were performed in ambient conditions.

4.4 Results and Discussion

4.4.1 Electrical characterizations of MIM capacitors

Areal capacitance values (C_i) of the capacitors versus frequency are given in Figure 4.2. Mango sap dielectric materials were tested at two different coating speeds (2000 rpm and 2500 rpm). Capacitors exhibited reasonable capacitance values regarding coating speeds (Figure 4.2a). As the coating speed rises, the thickness of the coated material decreases. C is reversely proportional to the thickness, which means the thinner layer gives higher capacitance values. Capacitors with mango sap dielectric coated at 2500 rpm showed 42.56 ± 5.29 nF/cm^2 areal capacitance at 1 kHz, a 30 % more value (29.7 ± 2.99 nF/cm^2 at 1 kHz) than that of coated at 2000 rpm. Capacitors with cactus sap dielectric with PMMA passivating layer presented 93.53 ± 8.23 nF/cm^2 areal capacitance (Figure 4.2b) at 1 kHz. Thinner cactus sap layers couldn’t provide stable capacitance values at varying frequency ranges. However, capacitors with cactus sap dielectric coated at 1000 rpm had approximately two times higher (54.49 %) C_i values than that of mango sap dielectric coated at 2500 rpm. Areal capacitance values of aloe vera single layer and bilayer dielectric-based MIM capacitors are given in Figure 4.2c. It is seen clearly that capacitors using aloe vera layers displayed higher values than that of mango-based capacitor values.

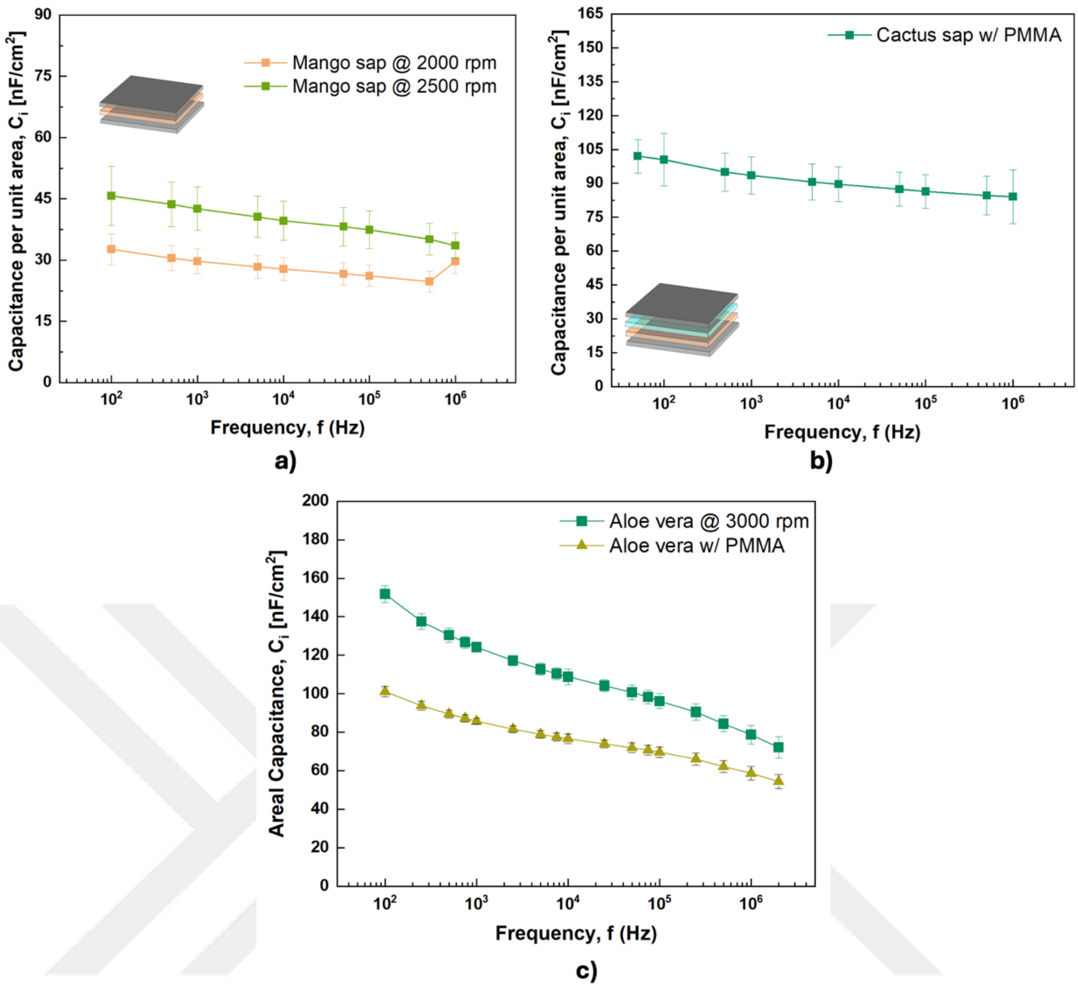

Figure 4.2 : Comparative graphs of areal capacitance values (C_i, nF / cm^2) versus frequency (Hz) of (a) mango sap, (b) cactus sap with PMMA and (c) aloe vera (with and without PMMA layer) based-MIM capacitors.

Bilayer capacitors of aloe vera gave a bit lower areal capacitance (85.72 ± 1.46 nF / cm^2 at 1 kHz) than cactus dielectric capacitors (93.53 ± 8.23 nF/cm^2 at 1 kHz). Single-layer aloe vera had the highest areal capacitance value (124.17 ± 2.36 nF/cm^2 at 1 kHz). Single-layer aloe vera showed a 65. 72 % increase and bilayer aloe vera showed a 50.34 % increase in areal capacitances than that of mango dielectric (coated at 2500 rpm)-based MIM capacitors. C_i values at low frequencies were higher than those at high frequencies (> 10^4 Hz). At high-frequency levels, capacitors can’t have enough time to polarise fully and can’t align with the electrical field. Consequently, the capacitance values drop moderately. Another explanation for high C_i values at low frequencies can be the interfacial polarization mechanism at the $10^2 – 10^3$ Hz frequency range that arises from the partially mobile charge carriers under the applied electrical field [184,185].

The dissipation factors (DF) of the mango sap-based and cactus sap-based MIM devices are given in Figure 4.3a and b. DF factor is the power loss of the capacitor when the voltage is applied to the capacitor [272]. It should be close to zero showing the electrical stability of the device. It is seen from the graphs that the DF factor for all samples wasn't zero which means it is not an ideal electrical behaviour. However, it can be said that DF values followed a steady regime from 10^3 Hz to 10^5 Hz frequency range, around, nearly zero at frequency, and finally reached 0.226 ± 0.8 for cactus sap. Mango sap-based samples displayed similar behaviour at low frequency. First, they had low DF, then showed an increase. The lowest and highest DF values were observed at 0.048 ± 0.003 at $5x10^3$ frequency and 0.167 ± 0.07 at 1 MHz frequency for the mango sap dielectric-based MIM capacitors (coating speed = 2500 rpm).

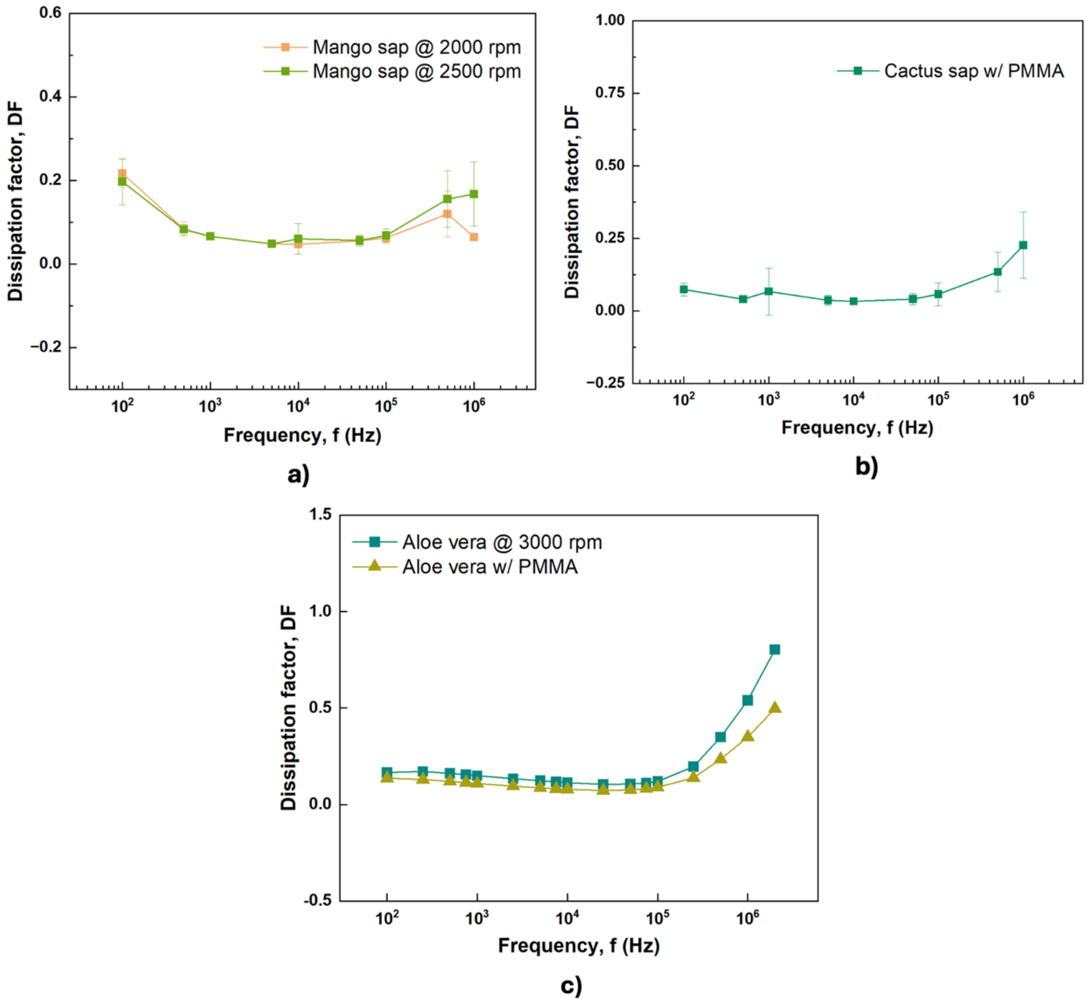

Figure 4.3 : Comparative graphs of dissipation factor (DF) values versus frequency (Hz) of (a) mango sap, (b) cactus sap with PMMA and (c) aloe vera (with and without PMMA layer) based-MIM capacitors.

Mango sap dielectric-based MIM capacitors coated at 2000 rpm showed the highest value at 0.06 ± 0.004 and 0.047 ± 0.002 at 1 MHz and 10^4 Hz frequencies, respectively. Cactus sap dielectric-based MIM capacitors gave the lowest DF value at 0.032 ± 0.008 at 10^4 Hz, and the highest DF value 0.226 ± 0.8 was seen at 1 MHz. Aloe vera single layers and bilayers showed a similar trend. Single-layer (0.14 DF) and bilayer samples (0.1 DF) followed a stable route between 10^2 – 10^5 Hz. Capacitance values should be stable when the voltage is applied. Figure 4.4a and b depict measured areal capacitance values at 1 kHz frequency versus applied voltage at a specific range for mango sap-based and cactus sap-based samples. When the bias voltage was applied from – 3 V to 3 V (interval 0.5 V), C_i values remained stable for all samples. This behaviour ensures the reliability of a capacitor for an OFET device [273].

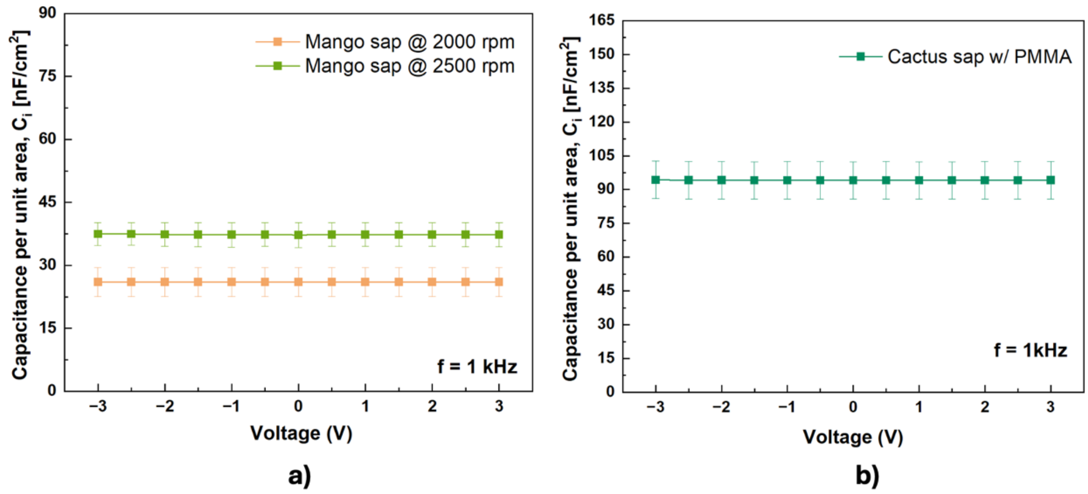

Figure 4.4 : Comparative graphs of areal capacitance values (C_i, nF/cm^2) versus voltage (V) of (a) mango sap and (b) cactus sap + PMMA based-MIM at 1 kHz frequency.

Table 4.1 summarises the C_i values and leakage current densities of two natural dielectric-based capacitors. Both natural products are hydrophilic and have low viscosity, making it hard to coat them homogeneously. They have susceptible surfaces to moisture that can lead to high leakage currents on the device.

The leakage current densities of mango sap and cactus sap-based capacitors are depicted in Figure 4.5. In particular, cactus sap dielectric materials showed a relatively higher leakage current (9.76x10^{-7} A/cm^2 at 2 V) than mango sap dielectric even though they were coated with a passivating PMMA layer. Cactus sap material was spin-coated at 1000 rpm to obtain a thicker layer. Thus, it was planned to see a lower leakage current. It was achieved by observing < 10^{-6} A/cm^2 leakage current density.

Table 4.1 : Areal capacitance values with leakage current densities for each natural dielectric layer.

Sample	C_i (nF/cm^2) at 1 kHz	Leakage current density (A/cm^2) at 2 V
Mango sap@2500 rpm	42.56 ± 5.29	3.64×10^{-7}
Mango sap@2000 rpm	29.7 ± 2.99	6.88×10^{-7}
Cactus sap w/PMMA	93.53 ± 8.23	9.76×10^{-7}
Aloe vera	124 ± 2.36	7.14×10^{-9}
Aloe vera w/PMMA	85.72 ± 1.46	9.48×10^{-10}

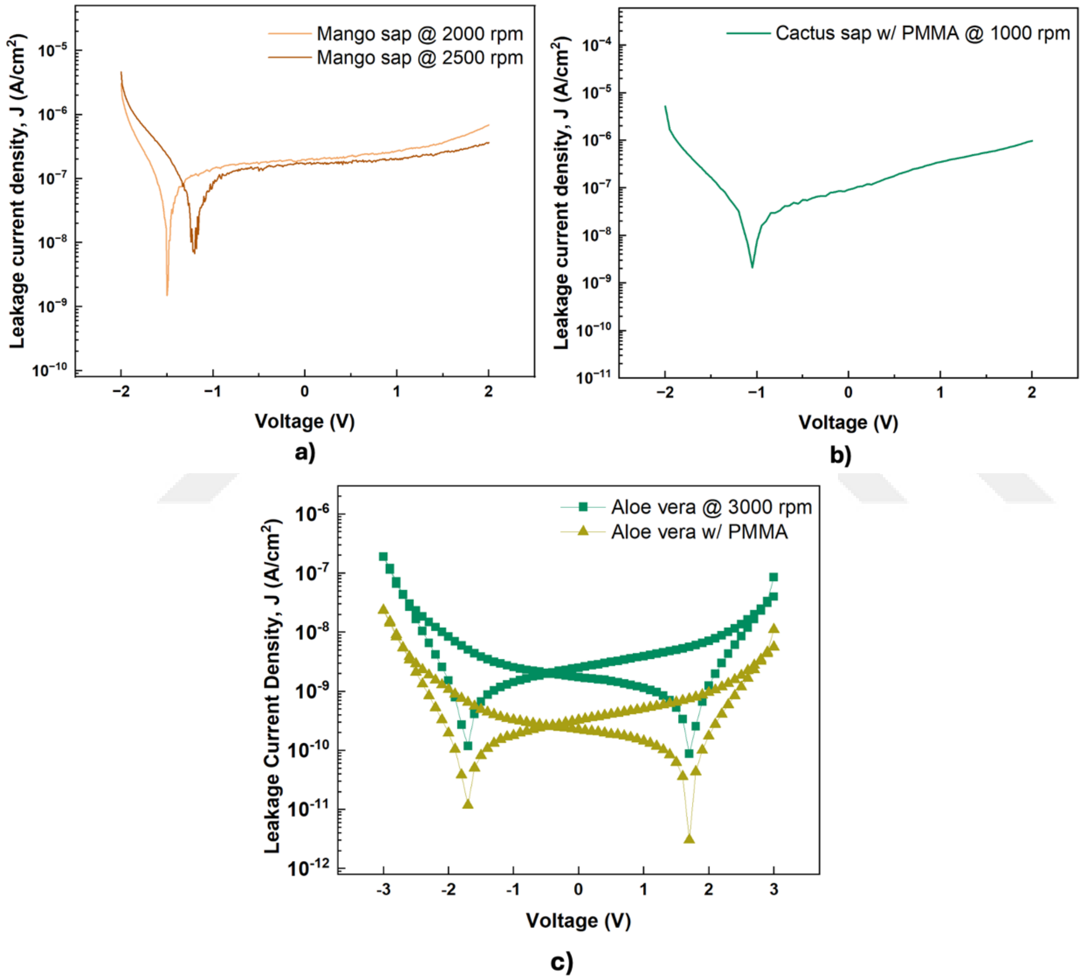

Figure 4.5 : Comparative graphs of leakage current density values (J, A/cm^2) versus voltage (V) of (a) mango sap**,** (b) cactus sap with PMMA and (c) aloe vera (with and without PMMA layer) based-MIM capacitors.

Mango sap dielectrics had lower leakage current densities; 3.64×10^{-7} A/cm^2 at 2 V for mango sap coated at 2500 rpm, 6.88×10^{-7} A/cm^2 at 2 V for mango sap coated at 2000 rpm (Figure 4.5b). The low viscosity of the material can increase the possibility of distribution of the sap material on the surface.

Hence, the unstable results can be attributed to the nature of these materials. These all remark that mango sap and cactus sap natural materials require optimisation to reach high performance. However, aloe vera single-layer-based devices and bilayer-based devices (Figure 4.5c) presented the lowest leakage densities; $7.14\text{x}10^{-9}$ A/cm^2 at 2 V for the aloe vera dielectric layer and $9.48\text{x}10^{-10}$ A/cm^2 at 2 V for the aloe vera with PMMA dielectric layer.

4.4.2 Photophysical properties of organic semiconductors

The chemical structures of organic semiconductors are given in Figure 4.6. The optical properties of organic semiconductors were characterised using UV-Vis spectrometry. The normalized absorption spectra showed strong absorption peaks at 535 nm and 575 nm. It illustrates (Figure 4.7) that OSCs are in the visible range. The optical band gap energies were calculated to be 1.98 eV from their onset absorption wavelengths.

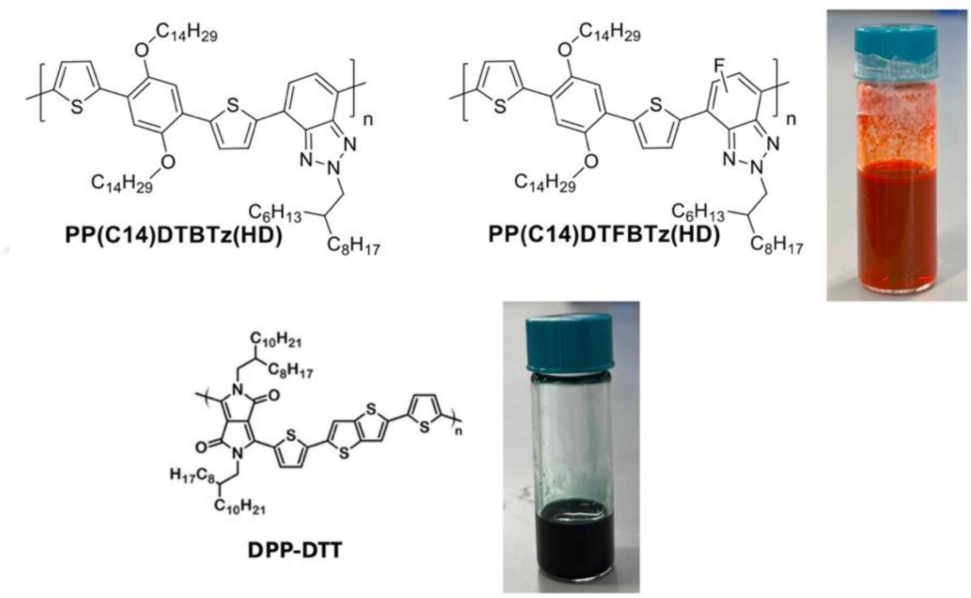

Figure 4.6 : The chemical structure of organic semiconductors and their solution forms in chloroform were shown.

Two polymers showed similar absorption spectra due to the strong intramolecular charge transfer interactions from thiophene to the BTz moieties [281]. Interconnected grains in crystal OSCs increase the charge carrier mobility in the device [284]. Figure 4.7a shows that OSC polymers are in the amorph region at room temperature. It is known from the literature that under elevated temperatures organic semiconductors begin to show high-order crystal structure [233,280,281].

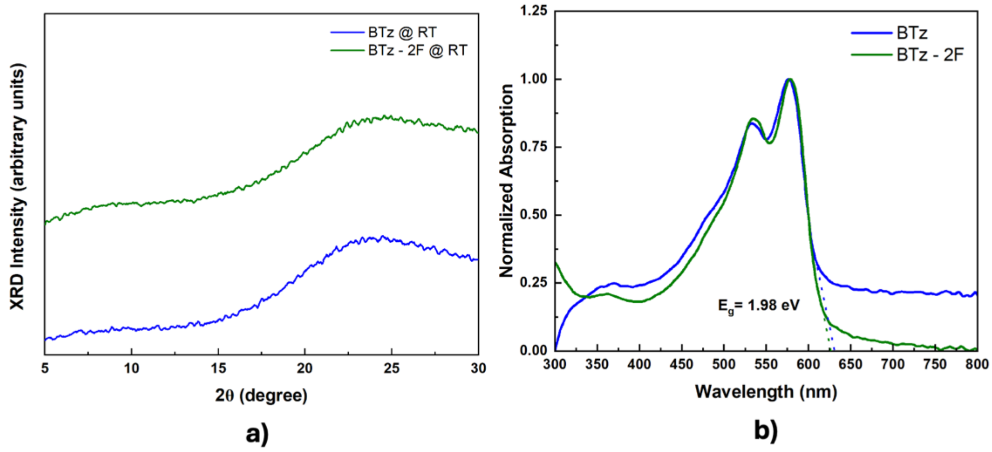

Figure 4.7 : XRD pattern and UV-Vis spectroscopy of organic semiconductors BTz and BT-2F by giving normalised absorbance vs wavelength (nm). E_g was calculated using $E_g = hc/\lambda$ formula.

On the other hand, small grains can cause a decrease in the charge carrier mobility because of lots of grain boundaries. They can act as traps or barriers for charge carriers [267,285]. A controversial situation exists in there which needs more research on it.

4.4.3 Electrical characterizations of OFET devices

BTz-based-OFET devices regardless of the dielectric layer couldn't demonstrate OFET device requirements (Figure 4.8). They gave high leakage currents and short-circuited. This was attributed to the necessity of the BTz-based OSCs for high-temperature annealing. However, it was impossible to anneal them at > 100 °C because of the low T_g values of the dielectric materials. So, OSCs couldn't be formed as a semiconducting layer in the device, and it caused a short circuit.

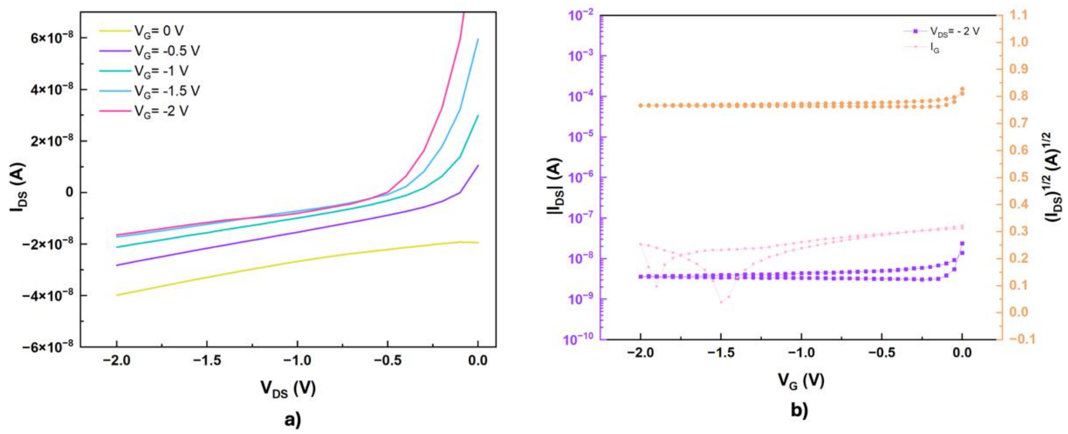

Figure 4.8 : (a) Output and (b) transfer curves of OFET device with CEC dielectric layer and PP(C14)DTBTz(HD) OSC layer.

Figure 4.9 shows a CEC dielectric-based OFET device using DPP-DTT:PMMA (solution 7:3 ratio) active layer. On the contrary the BTz-based OFETs, this commercial one achieved to give OFET characteristics and operated accumulation mode. This fabricated sample presented a typical p-type transistor behaviour [31,32]. Figure 4.9a and b illustrate the output curve and transfer curve of the device. The fabricated transistors didn't display low hysteresis which can be attributed to the charge-trapping effect at the semiconductor/dielectric interface, in the gate dielectric or active layer [286]. Because CEC consists of hydroxyl groups which can act as traps for charge carriers. Moreover, these functional groups make the device more susceptible to moisture. So, dielectric can degrade, and this issue hits the electrical performance negatively. To achieve the best electrical performance of an OFET device, a high-quality interface is necessary. Coating bilayer OSC:dielectric like DPP-DTT on the top and PMMA at the bottom, the PMMA layer can behave as a buffer layer [185]. This strategy in the current section improved the performance and hindered the negative results.

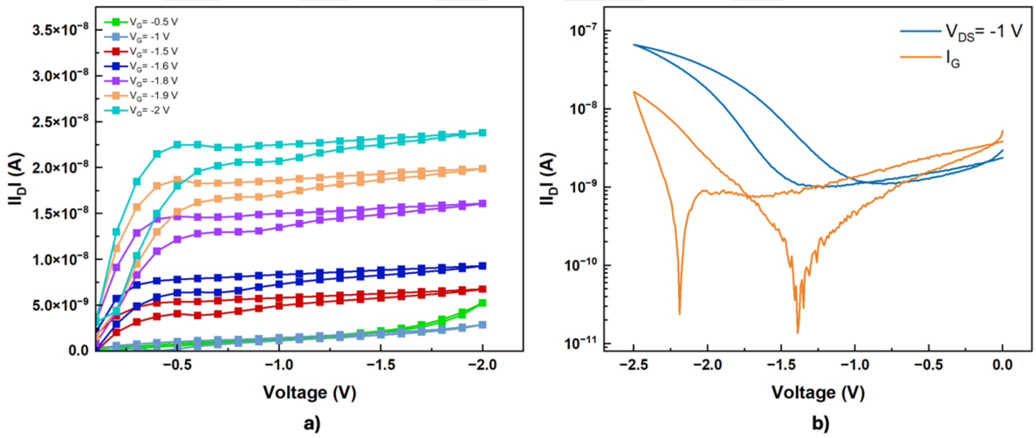

Figure 4.9 : (a) Output and (b) transfer curves of OFET device with CEC dielectric layer and DPP-DTT:PMMA OSC layer.

The gate dielectric leakage current was < 10^{-7} A at – 2.5 V. An optimum OFET device has a > 10^5 on/off current ratio to work as a sensor. However, the on/off ratio was around ~ 30 and did not provide a suitable value. It is probably because of the leakage current or doping of the active layer. Off current is a combination of leakage current and bulk current. A high dielectric current can distract the off current and this causes a low on/off ratio. One possible way to increase the on/off current ratio and reduce the leakage current of the gate dielectric is to minimise the device dimension and pattern of the OSC [185].

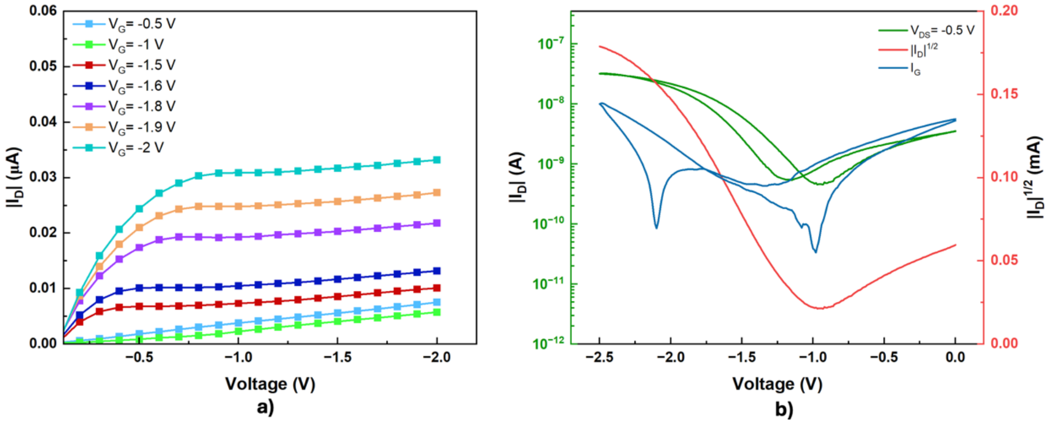

Figure 4.10 : (a) Output and (b) transfer curves of OFET devices with mango sap dielectric layer and DPP-DTT:PMMA OSC layer.

Mango sap @ 2500 rpm (Figure 4.10) and cactus sap + PMMA dielectrics (Figure 4.11) were examined in a transistor device with a commercial DPP-DTT semiconductor as an active layer. Apart from the mango sap and CEC, cactus sap was studied using PMMA as a bilayer dielectric layer. Hence, OSC was coated without a buffer layer. All samples operated in accumulation mode and showed p-type features. Transfer curves were obtained at – 0.5 V and – 1 V source – drain voltage (V_{DS}) for mango sap and cactus sap dielectric-based devices, respectively. The transistor with mango sap dielectric turned on at – 0.75 V threshold voltage (V_{th}) and had a low on/off current ratio (~ 180) with 0.32 cm^2/Vs mobility due to a high gate dielectric leakage current (~ 10^{-8} A at – 2.5 V). This can be explained by the nature of mango sap and its unstable characteristics in transistor devices. Its sap form made the coating of the material hard, and its hydrophilic structure could dope the OSC or create traps at the interface [286].

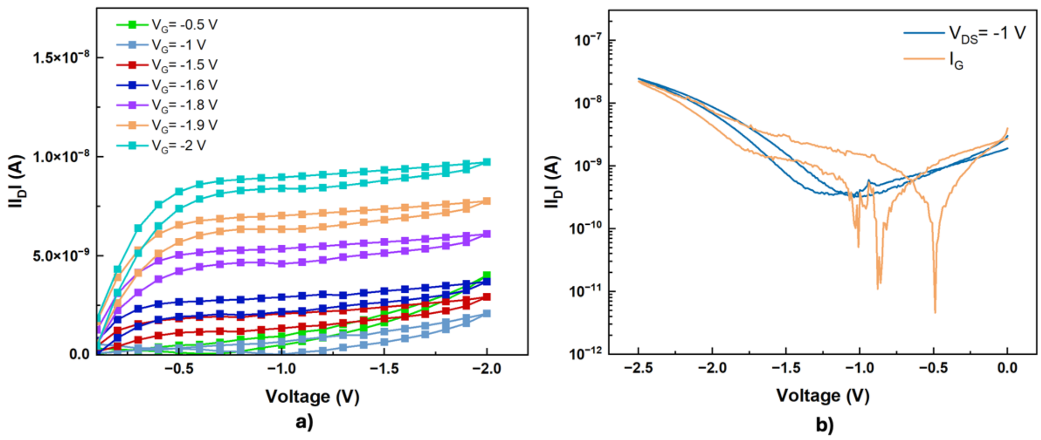

Figure 4.11 : (a) Output and (b) transfer curves of OFET devices with cactus sap + PMMA dielectric layer and DPP-DTT OSC layer.

It was seen that cactus sap dielectric wasn't a good choice for OFET devices due to its unstable characteristics. It is needed to research the chemical and physical properties of cactus sap materials to get an optimized OFET device. All samples of aloe vera dielectric-based devices (Figure 4.12 and Figure 4.13) operated in accumulation mode and showed p-type features. DPP-DTT was applied as an organic semiconductor layer. Transfer curves were obtained at – 2 V source – drain voltage (V_{DS}). Aloe vera-based device samples presented acceptable and desirable electrical performances with μ_{sat} = 0.35 ± 0.05 cm^2/Vs and 2.7 x 10^3 on/off ratio. The gate dielectric leakage current was $9x10^{-9}$ A at –2 V for single-layer aloe vera.

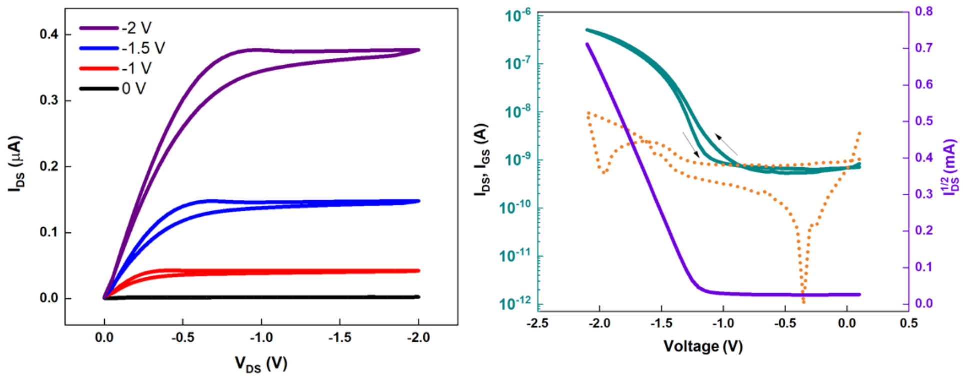

Figure 4.12 : (a) Output and (b) transfer curves of OFET devices with aloe vera dielectric layer and DPP-DTT OSC layer.

PMMA-coated samples improved the performance, with a 2-fold increase in charge carrier mobility (μ_{sat} = 0.6 ± 0.1 cm^2/Vs) and a higher on/off ratio ($3.5x10^3$) with a lower subthreshold swing (SS) (decreased from 210 ± 20 mV/dec to 160 ± 25 mV/dec) value. The threshold voltage (V_{th}) shifted from – 1.2 V to – 1.05 V. The gate dielectric current was $1.36x10^{-9}$ A for PMMA coated one.

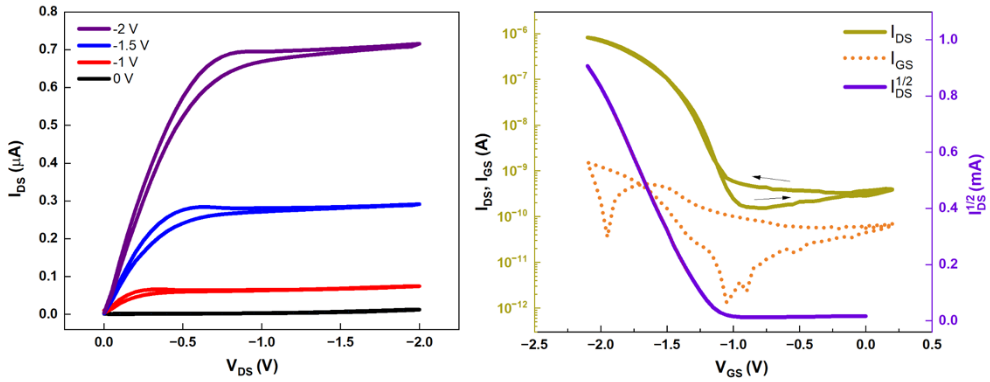

Figure 4.13 : (a) Output and (b) transfer curves of OFET devices with aloe vera + PMMA dielectric layer and DPP-DTT OSC layer.

Statistical analysis of saturated charge carrier mobilities is given in Figure 4.14. At least 20 OFETs for each single and bilayer dielectrics of aloe vera were fabricated and characterised to verify reproducibility and provide statistical analysis.

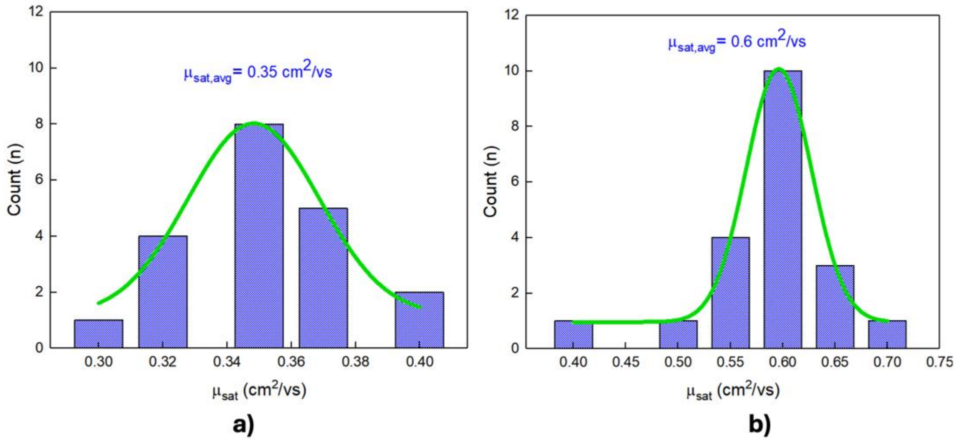

Figure 4.14 : Saturated charge carrier mobility statistics obtained from at least 20 OFETs using (a) aloe vera (b) aloe vera capped with PMMA as dielectric layers.

As seen from the graph (Figure 4.14b), half of the contacts of the aloe vera bilayer (with PMMA) displayed the highest mobility which showed the improved quality and reproducibility of the device.

4.5 Conclusion

In this chapter, solution-processed, natural, bioorganic dielectric designs in MIM capacitors and OFETs were investigated. Mango sap and cactus sap were the dielectric materials and were spin-coated directly without solvent. The synthesized polymers PP(C14)DTBTz(HD), PP(C14)DTFBTz(HD) and commercial DPP-DTT were cast as organic semiconductors. The XRD pattern showed organic semiconductors had an amorphous structure. The areal capacitance value of the thinner layer of mango sap dielectric (42.56 ± 5.29 nF/cm^2) exhibited improvement in comparison to the thicker layer of mango sap dielectric (29.7 ± 2.99 nF/cm^2). The areal capacitance of the MIM capacitor with cactus sap + PMMA exhibited a high value, 93.53 ± 8.23 nF/cm^2 at 1 kHz. Surprisingly, the leakage current density at 2 V of MIM capacitors with thinner mango sap dielectric had lower leakage current density, 3.64x10^{-7} A/cm^2, and thicker mango sap dielectric was measured 6.88x10^{-7} A/cm^2. Although cactus sap brought difficulties to the coating step in terms of catching uniformity, its double-layer form with PMMA showed an acceptable low leakage current density of 9.76x10^{-7} A/cm^2.

Aloe vera layer illustrated promising areal capacitance values with both single-layer use (124.17 ± 2.36 nF/cm^2) and bilayer use (85.72 ± 1.46 nF/cm^2). Their low leakage current densities (9.48×10^{-10} A/cm^2 for the aloe vera with PMMA layer) led to achieving high electrical performance for OFET operation. OFET devices using a DPP-DTT active layer with a PMMA buffer layer demonstrated a typical p-type transistor behaviour in an accumulation mode. Unfortunately, fabricated transistors with CEC and mango sap dielectric layers presented low on/off ratios and high gate dielectric currents. It can be attributed to the hydroxyl groups in the dielectric layers and charge traps at the interface. In conclusion, this study sheds light on natural, biodegradable mango sap, cactus sap and aloe vera dielectric materials for simple, cost-effective, solution-processed fabrication techniques at low temperatures. These natural, bioorganic dielectric layers could soon replace the conventional dielectrics for high-performance, low voltage operating OFET and sensor devices.

5. CONCLUSIONS

5.1 Conclusions

In this dissertation, solution-processed, low-cost organic field-effect transistors, organic phototransistors, and MIM capacitors were investigated and presented including literature examples. The focus was developing OFET devices and capacitors for home-assisted, low-cost, easy-to-use sensors by applying solution-processable materials.

The first chapter was based on a published review article on solution-processed OFET and OPT devices, and their operation principles and device configurations were illustrated with equations and figures. Applications of solution-processed OPT devices were given from the literature. Solution-processed FET devices provide a cost-effective way to fabricate high-throughput technological sensors. Organic semiconductors due to their functionality feature make devices gain adjusted bandgap, improved solubility, and flexibility over traditional semiconductors. The choice of using natural dielectrics has the advantage of having high-*k* constant and solution-processability In addition, they offer biocompatibility and degradation which in turn gives a new perspective to be applied to in vivo implementation. Nanocomposite dielectrics can supply high-*k* constant and improve the properties of polymeric matrixes by just blending them with small-diameter nanoparticles. Apart from that, using a biodegradable substrate such as glass and paper or flexible ones like PEN has the potential to increase the applications of these in sports and medical areas. Three-electrode structures and four different configurations of the OPTs enhance the quality of the sensors regarding amplifying the signal and light illumination side, respectively.

The second chapter included a published study on OPTs and their applications as artificial synapses. Already published literature examples were given as examples of the artificial synapses based on OPT structure. Artificial synapses can be designed using a three-electrode structure and mimic the biological synapses successfully. OPT devices have the potential to operate under low voltages (< 3 V) which makes them effective sensor devices compared to conventional systems. A FET structure has a memory and processing unit at the same location. OPT devices can receive light. Hence, they can mimic retinal functions, as well. Artificial synapses based on OPTs are on the rise due to their low energy consumption and fast response. On the other hand, research on mimicking the human brain enables the storage of information and memory functions, such as learning/forgetting. OPTs paving the way towards potential. They are promising devices for sensing visual activity.

The third and fourth chapters shed light on different dielectric materials of capacitors for OFET applications. Figure 5.1 shows the comparison between the dielectric materials in the literature versus areal capacitance values. Arrows remark the dielectric materials in this study.

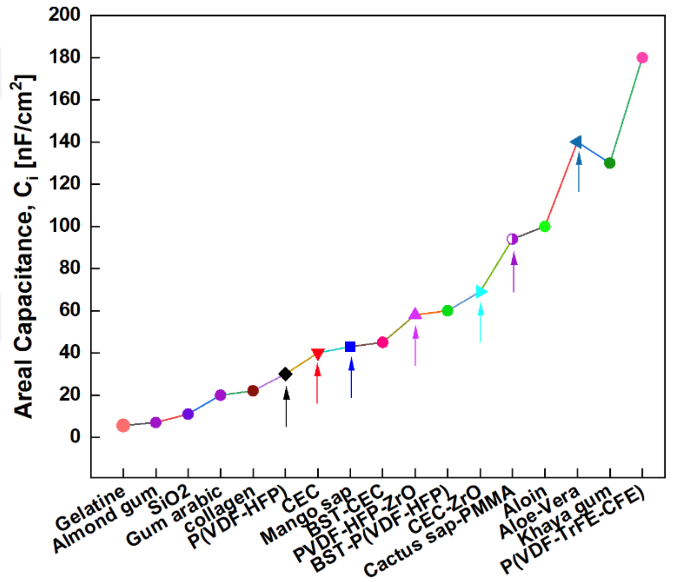

Figure 5.1 : The graph compares the areal capacitance values of different dielectric materials in this study (remarked with arrows) and in the literature.

The third chapter aimed to show an experimental study of nanocomposite MIM capacitors using two different polymeric matrixes for OFET applications. This study has been submitted to the Materials Science in Semiconductor Processing journal and is under review now. The effects of varying nanoparticle concentrations and polymeric matrixes were investigated on MIM capacitors. Fabricated devices were evaluated in terms of their electrical properties and physical properties. It was shown that the nanoparticle amount (1 wt %, 1.5 wt %, 5 wt %, and 10 wt %) directly impacted the areal capacitance values of capacitors. As the number of nanoparticles increased, the areal capacitance values (C_i) and *k* values increased with acceptable low leakage current densities. The leakage current increased due to the roughness of the nanocomposite layer, it was an acceptable range that the highest leakage current density was $1.75x10^{-6}$ A/cm^2 from CZ10. Results indicated that PVDF-HFP is more suitable because of its high C_i value and hydrophobic structure compared to the CEC polymeric matrix. 5 % wt ZrO_2 can be the optimum content for two dielectrics, C_i of CZ5 is 68.85 ± 2.16 nF/cm^2 and PZ5 is 57.79 ± 4.65 nF/cm^2 at 1 kHz. The dielectric constants (*k*) were 28.61 ± 0.1 and 35.68 ± 1.99 for CEC + ZrO_2 (5 wt %) and PVDF-HFP + ZrO_2 (5 wt %), respectively. In conclusion, this study sheds light on novel dielectric studies with cost-effective, solution-processed techniques at low-temperature fabrication without applying high annealing temperatures. NC dielectric layers in the form of polymer – nanoparticle using metal oxide ceramics will soon create a new page on the studies of low-operate voltage OFETs.

The fourth chapter included experimental studies on natural dielectrics, mango sap, cactus sap, and aloe vera-based MIM capacitors and fabricated OFET devices. DPP-DTT commercial OSC was studied for OFET devices. These natural materials demonstrated high areal capacitance values and electrical stability. However, due to high gate currents, mango sap and cactus sap-based OFET device performance couldn't give high on/off ratios. This can be attributed to the high hydrophilicity of the natural materials. Interestingly, aloe vera single layer and bilayer showed promising OFET performances. The areal capacitance value of the thinner layer of mango sap dielectric (42.56 ± 5.29 nF/cm^2) improved compared to the thicker layer of mango sap dielectric (29.7 ± 2.99 nF/cm^2). The areal capacitance of the MIM capacitor with cactus sap + PMMA exhibited a high value, 93.53 ± 8.23 nF/cm^2 at 1 kHz. Surprisingly, the leakage current density at 2 V of MIM capacitors with thinner mango sap dielectric had lower leakage current density, $3.64x10^{-7}$ A/cm^2, and thicker mango sap dielectric was measured $6.88x10^{-7}$ A/cm^2. Although cactus sap brought difficulties to the coating step in terms of catching uniformity, its double-layer form with PMMA showed an acceptable low leakage current density of $9.76x10^{-7}$ A/cm^2. Aloe vera layer illustrated promising areal capacitance values with both single-layer use (124.17 ± 2.36 nF/cm^2) and bilayer use (85.72 ± 1.46 nF/cm^2). Their low leakage current densities ($9.48x10^{-10}$ A/cm^2 for the aloe vera with PMMA layer) led to achieving high electrical performance for OFET operation. These natural, bioorganic dielectric layers could soon replace the conventional dielectrics for high-performance, low voltage operating OFET and sensor devices.

5.2 Recommendations for Future Work

Regarding the third chapter, OFET applications of nanocomposite dielectrics and their VOC and OPT applications will be searched. OPT devices under varying light intensities should be tested to observe the artificial synapse properties of the OPT device. VOC sensing of OFET devices with synthesized novel OSCs is crucial and should be done in future electronic nose applications. Apart from the ZrO_2, graphene oxide nanoparticles can be tested, as well. So, they can be compared in terms of their electrical performance on the MIM structure.

Related to the fourth chapter, it is necessary to focus on the physical characteristics of mango sap and cactus sap. Then, the required optimizations can be done to improve the device's performance. Thickness measurements should be done to calculate the k values. Leakage current densities should be decreased using suitable passivating layers with an optimum concentration. They can be improved by blending with nanoparticles like TiO_2 or graphene oxide.

Changing the substrate to paper or other flexible polymeric ones can be discussed and considered. Improving devices to use in vivo applications and combining them with hydrogels. In vitro tests such as antibacterial, cell proliferation and biocompatibility tests should be done to make sure that these devices can be used in vivo applications.

REFERENCES

[1] **Wakayama, Y., Hayakawa, R. and Seo, H.S.** (2014) Recent progress in photoactive organic field-effect transistors. *Science and Technology of Advanced Materials*, IOP Publishing. *15*. https://doi.org/10.1088/1468-6996/15/2/024202

[2] **Wang, C., Zhang, X. and Hu, W.** (2020) Organic photodiodes and phototransistors toward infrared detection: Materials, devices, and applications. *Chemical Society Reviews*, Royal Society of Chemistry. *49*, 653–70. https://doi.org/10.1039/c9cs00431a

[3] **Baeg, K.J., Binda, M., Natali, D., Caironi, M. and Noh, Y.Y.** (2013) Organic light detectors: Photodiodes and phototransistors. *Advanced Materials*, *25*, 4267–95. https://doi.org/10.1002/adma.201204979

[4] **Xie, C., Liu, C.K., Loi, H.L. and Yan, F.** (2020) Perovskite-Based Phototransistors and Hybrid Photodetectors. *Advanced Functional Materials*, *30*, 1–28. https://doi.org/10.1002/adfm.201903907

[5] **Wu, Z., Zhai, Y., Kim, H., Azoulay, J.D. and Ng, T.N.** (2018) Emerging Design and Characterization Guidelines for Polymer-Based Infrared Photodetectors. *Accounts of Chemical Research*, American Chemical Society. *51*, 3144–53. https://doi.org/10.1021/acs.accounts.8b00446

[6] **Chow, P.C.Y. and Someya, T.** (2020) Organic Photodetectors for Next-Generation Wearable Electronics. *Advanced Materials*, *32*, 1–26. https://doi.org/10.1002/adma.201902045

[7] **Zaumseil, J. and Sirringhaus, H.** (2007) Electron and ambipolar transport in organic field-effect transistors. *Chemical Reviews*, *107*, 1296–323. https://doi.org/10.1021/cr0501543

[8] **Öberg, P.Å.** (2008) Optical Sensors in Medical Care. *Sensors Applications*, *3*, 15–43. https://doi.org/10.1002/9783527619252.ch2h

[9] **Xu, H., Li, J., Leung, B.H.K., Poon, C.C.Y., Ong, B.S., Zhang, Y. et al.** (2013) A high-sensitivity near-infrared phototransistor based on an organic bulk heterojunction. *Nanoscale*, *5*, 11850–5. https://doi.org/10.1039/c3nr03989g

[10] **Rim, Y.S., Yang, Y., Bae, S.H., Chen, H., Li, C., Goorsky, M.S. et al.** (2015) Ultrahigh and Broad Spectral Photodetectivity of an Organic-Inorganic Hybrid Phototransistor for Flexible Electronics. *Advanced Materials*, *27*, 6885–91. https://doi.org/10.1002/adma.201502996

[11] **García De Arquer, F.P., Armin, A., Meredith, P. and Sargent, E.H.** (2017) Solution-processed semiconductors for next-generation photodetectors. *Nature Reviews Materials*, *2*. https://doi.org/10.1038/natrevmats.2016.100

[12] **Liu, J., Wang, Y., Wen, H., Bao, Q., Shen, L. and Ding, L.** (2020) Organic Photodetectors: Materials, Structures, and Challenges. *Solar RRL*, *4*, 1–8. https://doi.org/10.1002/solr.202000139

[13] **Kurz, W., Yetisen, A.K., Kaito, M.V., Fuchter, M.J., Jakobi, M., Elsner, M. et al.** (2020) UV-Sensitive Wearable Devices for Colorimetric Monitoring of UV Exposure. *Advanced Optical Materials*, *8*. https://doi.org/10.1002/adom.201901969

[14] **Nasiri, N., Bo, R., Wang, F., Fu, L. and Tricoli, A.** (2015) Ultraporous Electron-Depleted ZnO Nanoparticle Networks for Highly Sensitive Portable Visible-Blind UV Photodetectors. *Advanced Materials*, *27*, 4336–43. https://doi.org/10.1002/adma.201501517

[15] **Xu, H., Liu, J., Zhang, J., Zhou, G., Luo, N. and Zhao, N.** (2017) Flexible Organic/Inorganic Hybrid Near-Infrared Photoplethysmogram Sensor for Cardiovascular Monitoring. *Advanced Materials*, *29*, 1–6. https://doi.org/10.1002/adma.201700975

[16] **Li, N., Lan, Z., Lau, Y.S., Xie, J., Zhao, D. and Zhu, F.** (2020) SWIR Photodetection and Visualization Realized by Incorporating an Organic SWIR Sensitive Bulk Heterojunction. *Advanced Science*, *2000444*, 1–8. https://doi.org/10.1002/advs.202000444

[17] **Lee, Y.H., Jang, M., Lee, M.Y., Kweon, O.Y. and Oh, J.H.** (2017) Flexible Field-Effect Transistor-Type Sensors Based on Conjugated Molecules. *Chem*, Elsevier Inc. *3*, 724–63. https://doi.org/10.1016/j.chempr.2017.10.005

[18] **Gu, P., Yao, Y., Feng, L., Niu, S. and Dong, H.** (2015) Recent advances in polymer phototransistors. *Polymer Chemistry*, *6*, 7933–44. https://doi.org/10.1039/c5py01373a

[19] **Dou, L., Liu, Y., Hong, Z., Li, G. and Yang, Y.** (2015) Low-Bandgap Near-IR Conjugated Polymers/Molecules for Organic Electronics. *Chemical Reviews*, *115*, 12633–65. https://doi.org/10.1021/acs.chemrev.5b00165

[20] **Mei, J., Diao, Y., Appleton, A.L., Fang, L. and Bao, Z.** (2013) Integrated materials design of organic semiconductors for field-effect transistors. *Journal of the American Chemical Society*, *135*, 6724–46. https://doi.org/10.1021/ja400881n

[21] **Guo, Y., Yu, G. and Liu, Y.** (2010) Functional organic field-effect transistors. *Advanced Materials*, *22*, 4427–47. https://doi.org/10.1002/adma.201000740

[22] **Chortos, A., Liu, J. and Bao, Z.** (2016) Pursuing prosthetic electronic skin. *Nature Materials*, Nature Publishing Group. *15*, 937–50. https://doi.org/10.1038/nmat4671

[23] **Serdar Sariciftci, N.** (2004) Plastic photovoltaic devices. *Materials Today*, *7*, 36–40. https://doi.org/10.1016/S1369-7021(04)00400-6

[24] **Liu, J., Jiang, L., Shi, J., Li, C., Shi, Y., Tan, J. et al.** (2020) Relieving the Photosensitivity of Organic Field-Effect Transistors. *Advanced Materials*, *32*, 1–8. https://doi.org/10.1002/adma.201906122

[25] **Park, H.L., Kim, M.H. and Kim, H.** (2020) Improvement of photoresponse in organic phototransistors through bulk effect of photoresponsive gate insulators. *Materials*, *13*. https://doi.org/10.3390/ma13071565

[26] **Huang, X., Ji, D., Fuchs, H., Hu, W. and Li, T.** (2020) Recent Progress in Organic Phototransistors: Semiconductor Materials, Device Structures and Optoelectronic Applications. *ChemPhotoChem*, *4*, 9–38. https://doi.org/10.1002/cptc.201900198

[27] **Yang, S.Y., Shin, K. and Park, C.E.** (2005) The effect of gate-dielectric surface energy on pentacene morphology and organic field-effect transistor characteristics. *Advanced Functional Materials*, *15*, 1806–14. https://doi.org/10.1002/adfm.200400486

[28] **Ren, X., Yang, F., Gao, X., Cheng, S., Zhang, X., Dong, H. et al.** (2018) Organic Field-Effect Transistor for Energy-Related Applications: Low-Power-Consumption Devices, Near-Infrared Phototransistors, and Organic Thermoelectric Devices. *Advanced Energy Materials*, *8*, 1–27. https://doi.org/10.1002/aenm.201801003

[29] **Sirringhaus, H.** (2005) Device physics of solution-processed organic field-effect transistors. *Advanced Materials*, *17*, 2411–25. https://doi.org/10.1002/adma.200501152

[30] **Sirringhaus, H.** (2014) 25th anniversary article: Organic field-effect transistors: The path beyond amorphous silicon. *Advanced Materials*, *26*, 1319–35. https://doi.org/10.1002/adma.201304346

[31] **Horowitz, B.G.** (1998) Organic Field-Effect Transistors. *Advanced Materials*, 365–77.

[32] **Braga, D. and Horowitz, G.** (2009) High-Performance organic field-effect transistors. *Advanced Materials*, *21*, 1473–86. https://doi.org/10.1002/adma.200802733

[33] **Huang, J., Du, J., Cevher, Z., Ren, Y., Wu, X. and Chu, Y.** (2017) Printable and Flexible Phototransistors Based on Blend of Organic Semiconductor and Biopolymer. *Advanced Functional Materials*, *27*, 1–8. https://doi.org/10.1002/adfm.201604163

[34] **Han, H., Lee, C., Kim, H. and Kim, Y.** (2018) Flexible Near-Infrared Plastic Phototransistors with Conjugated Polymer Gate-Sensing Layers. *Advanced Functional Materials*, *28*, 1–8. https://doi.org/10.1002/adfm.201800704

[35] **Lei, Y., Li, N., Chan, W.K.E., Ong, B.S. and Zhu, F.** (2017) Highly sensitive near infrared organic phototransistors based on conjugated polymer nanowire networks. *Organic Electronics*, *48*, 12–8. https://doi.org/10.1016/j.orgel.2017.05.029

[36] **Lee, G.H., Moon, H., Kim, H., Lee, G.H., Kwon, W., Yoo, S. et al.** (2020) Multifunctional materials for implantable and wearable photonic healthcare devices. *Nature Reviews Materials*, Springer US. *5*, 149–65. https://doi.org/10.1038/s41578-019-0167-3

[37] **Li, N., Lei, Y., Chan, W.K.E. and Zhu, F.** (2019) Broadband phototransistors realised by incorporating a bi-layer perovskite/NIR light absorbing polymer channel. *Journal of Materials Chemistry C*, *7*, 4808–16. https://doi.org/10.1039/c8tc06229c

[38] **Xia, Y., Wang, L., Deng, X., Li, D., Zhu, X. and Cao, Y.** (2006) Photocurrent response wavelength up to 1.1 μm from photovoltaic cells based on narrow-band-gap conjugated polymer and fullerene derivative. *Applied Physics Letters*, *89*, 89–92. https://doi.org/10.1063/1.2338017

[39] **Li, F., Chen, Y., Ma, C., Buttner, U., Leo, K. and Wu, T.** (2017) High-Performance Near-Infrared Phototransistor Based on n-Type Small-Molecular Organic Semiconductor. *Advanced Electronic Materials*, *3*. https://doi.org/10.1002/aelm.201600430

[40] **Li, D., Du, J., Tang, Y., Liang, K., Wang, Y., Ren, H. et al.** (2021) Flexible and Air-Stable Near-Infrared Sensors Based on Solution-Processed Inorganic–Organic Hybrid Phototransistors. *Advanced Functional Materials*, *31*, 1–10. https://doi.org/10.1002/adfm.202105887

[41] **Zhu, Z., Guo, Y. and Liu, Y. (**2020) Application of organic field-effect transistors in memory. *Materials Chemistry Frontiers*, Royal Society of Chemistry. *4*, 2845–62. https://doi.org/10.1039/d0qm00330a

[42] **Ling, Y., An, T., Yap, L.W., Zhu, B., Gong, S. and Cheng, W.** (2020) Disruptive, Soft, Wearable Sensors. *Advanced Materials*, John Wiley & Sons, Ltd. *32*, 1904664. https://doi.org/https://doi.org/10.1002/adma.201904664

[43] **Ebisawa, F., Kurokawa, T. and Nara, S.** (1983) Electrical properties of polyacetylene/polysiloxane interface. *Journal of Applied Physics*, *54*, 3255–9. https://doi.org/10.1063/1.332488

[44] **Wang, C., Dong, H., Hu, W., Liu, Y. and Zhu, D.** (2012) Semiconducting π-Conjugated Systems in Field-Effect Transistors. *Chemical Reviews*, *112*, 2208–67.

[45] **Fratini, S., Nikolka, M., Salleo, A., Schweicher, G. and Sirringhaus, H.** (2020) Charge transport in high-mobility conjugated polymers and molecular semiconductors. *Nature Materials*, *19*, 491–502. https://doi.org/10.1038/s41563-020-0647-2

[46] **Shi, L., Liang, Q., Wang, W., Zhang, Y., Li, G., Ji, T. et al.** (2018) Research progress in organic photomultiplication photodetectors. *Nanomaterials*, *8*, 17–9. https://doi.org/10.3390/nano8090713

[47] **Xie, W., Menke, S.M., Frisbie, C.D. and Holmes, R.J.** (2016) Experimental Characterization of Charge and Exciton Transport in Organic Semiconductors. *The WSPC Reference on Organic Electronics: Organic Semiconductors*, *1*, 231–91. https://doi.org/10.1142/9678

[48] **Forrest, S.R. and Thompson, M.E.** (2007) Introduction: Organic electronics and optoelectronics. *Chemical Reviews*, *107*, 923–5. https://doi.org/10.1021/cr0501590

[49] **Rivnay, J., Inal, S., Salleo, A., Owens, R.M., Berggren, M. and Malliaras, G.G.** (2018) Organic electrochemical transistors. *Nature Reviews Materials*, *3*, 17086. https://doi.org/10.1038/natrevmats.2017.86

[50] **Russ, B., Glaudell, A., Urban, J.J., Chabinyc, M.L. and Segalman, R.A.** (2016) Organic thermoelectric materials for energy harvesting and temperature control. *Nature Reviews Materials*, *1*, 16050. https://doi.org/10.1038/natrevmats.2016.50

[51] **van de Burgt, Y., Melianas, A., Keene, S.T., Malliaras, G. and Salleo, A.** (2018) Organic electronics for neuromorphic computing. *Nature Electronics*, *1*, 386–97. https://doi.org/10.1038/s41928-018-0103-3

[52] **Schlesinger, R.** (2017) Chapter 2 Fundamentals. *Energy-Level Control at Hybrid Inorganic/Organic Semiconductor Interfaces, 1st Ed*, 1st ed. Springer International Publishing AG, Springer Theses. p. 7–45. https://doi.org/10.1007/978-3-319-46624-8

[53] **Nunzi, J.-M.** (2002) Organic Materials and Devices for Photovoltaic Applicaitons. *Photovoltaic and Photoactive Materials- Propeerties, Technology and Applicaitons, Kluwer Academic Publishers*, 197–224.

[54] **Kalyani, N.T., Swart, H. and Dhoble, S.J.** (2017) Luminescence in Organic Semiconductors. *Principles and Applications of Organic Light Emitting Diodes (OLEDs)*, p. 39–64. https://doi.org/10.1016/b978-0-08-101213-0.00002-3

[55] **Sturge, M.D.** (2020) Electrons and Holes in Semiconductors. *Statistical and Thermal Physics*, 269–90. https://doi.org/10.1201/9781315275529-19

[56] **Brütting, W.** (2006) Physics of Organic Semiconductors. 1st ed. Physics of Organic Semiconductors. Wiley-VCH Verlag GmbH & Co. KGaA, Weinheim, Germany. https://doi.org/10.1002/3527606637

[57] **Zhu, M., Lv, S., Wang, Q., Zhang, G., Lu, H. and Qiu, L.** (2016) Enhanced near-infrared photoresponse of organic phototransistors based on single-component donor-acceptor conjugated polymer nanowires. *Nanoscale*, *8*, 7738–48. https://doi.org/10.1039/c5nr09003b

[58] **Nam, S., Han, H., Seo, J., Song, M., Kim, H., Anthopoulos, T.D. et al.** (2016) Ambipolar Organic Phototransistors with p-Type/n-Type Conjugated Polymer Bulk Heterojunction Light-Sensing Layers. *Advanced Electronic Materials, 2*, 1–8. https://doi.org/10.1002/aelm.201600264

[59] **Rao, M.C. and Shekhawat, M.S.** (2013) a Brief Survey on Basic Properties of Thin Films for Device Application. *International Journal of Modern Physics: Conference Series*, *22*, 576–82. https://doi.org/10.1142/s2010194513010696

[60] **Huang, W., Feng, L., Wang, G. and Reichmanis, E.** (2020) Wearable Organic Nano-sensors. *Flexible and Wearable Electronics for Smart Clothing*, 1–27. https://doi.org/10.1002/9783527818556.ch1

[61] **Ong, B.S., Wu, Y., Liu, P. and Gardner, S.** (2004) High-Performance Semiconducting Polythiophenes for Organic Thin-Film Transistors. *Journal of the American Chemical Society*, *126*, 3378–9. https://doi.org/10.1021/ja039772w

[62] **Zhang, F., Qu, G., Mohammadi, E., Mei, J. and Diao, Y.** (2017) Solution-Processed Nanoporous Organic Semiconductor Thin Films: Toward Health and Environmental Monitoring of Volatile Markers. *Advanced Functional Materials*, *27*, 17–20. https://doi.org/10.1002/adfm.201701117

[63] **Li, H., Shi, W., Dailey, J., Jang, H.-J., Song, J., Yu, J. et al.** (2019) Vapor sensing using organic, polymer, and nanomaterial field-effect transistors. 2nd ed. Handbook of Organic Materials for Electronic and Photonic Devices. Elsevier Ltd. https://doi.org/10.1016/b978-0-08-102284-9.00024-3

[64] **Park, S.J., Lee, S.H., Yang, H., Park, C.S., Lee, C.S., Kwon, O.S. et al.** (2016) Human Dopamine Receptor-Conjugated Multidimensional Conducting Polymer Nanofiber Membrane for Dopamine Detection. *ACS Applied Materials and Interfaces*, *8*, 28897–903. https://doi.org/10.1021/acsami.6b10437

[65] **Hu, J., Wei, W., Ke, S., Zeng, X. and Lin, P.** (2019) A novel and sensitive sarcosine biosensor based on organic electrochemical transistor. *Electrochimica Acta*, Elsevier Ltd. 307, 100–6. https://doi.org/10.1016/j.electacta.2019.03.180

[66] **Guo, Y., Yu, G. and Liu, Y.** (2010) Functional organic field-effect transistors. Advanced Materials. https://doi.org/10.1002/adma.201000740

[67] **Zhu, H., Luo, W., Ciesielski, P.N., Fang, Z., Zhu, J.Y., Henriksson, G. et al.** (2016) Wood-Derived Materials for Green Electronics, Biological Devices, and Energy Applications. *Chemical Reviews*, *116*, 9305–74. https://doi.org/10.1021/acs.chemrev.6b00225

[68] **Huang, J., Zhu, H., Chen, Y., Preston, C., Rohrbach, K., Cumings, J. et al.** (2013) Highly transparent and flexible nanopaper transistors. *ACS Nano*, *7*, 2106–13. https://doi.org/10.1021/nn304407r

[69] **Tobjörk, D. and Österbacka, R.** (2011) Paper electronics. *Advanced Materials*, *23*, 1935–61. https://doi.org/10.1002/adma.201004692

[70] **Qian, C., Sun, J., Yang, J. and Gao, Y.** (2015) Flexible organic field-effect transistors on biodegradable cellulose paper with efficient reusable ion gel dielectrics. *RSC Advances*, *5*, 14567–74. https://doi.org/10.1039/c4ra13240h

[71] **Torsi, L., Magliulo, M., Manoli, K. and Palazzo, G.** (2013) Organic field-effect transistor sensors: A tutorial review. *Chemical Society Reviews*, *42*, 8612–28. https://doi.org/10.1039/c3cs60127g

[72] **Kleemann, H., Krechan, K., Fischer, A. and Leo, K.** (2020) A Review of Vertical Organic Transistors. *Advanced Functional Materials*, *30*. https://doi.org/10.1002/adfm.201907113

[73] **Mohammadian, N., Faraji, S., Sagar, S., Das, B.C., Turner, M.L. and Majewski, L.A.** (2019) One-volt, solution-processed organic transistors with self-assembled monolayer-Ta2O5 gate dielectrics. *Materials*, *12*. https://doi.org/10.3390/ma12162563

[74] **Seck, M., Mohammadian, N., Diallo, A.K., Faraji, S., Saadi, M., Erouel, M. et al.** (2020) Low voltage organic transistors with water-processed gum arabic dielectric. *Synthetic Metals*, Elsevier. *267*, 116447. https://doi.org/10.1016/J.SYNTHMET.2020.116447

[75] **Lucas, B., Trigaud, T. and Videlot-Ackermann, C.** (2012) Organic transistors and phototransistors based on small molecules. *Polymer International*, *61*, 374–89. https://doi.org/10.1002/pi.3213

[76] **Ortiz, R.P., Facchetti, A. and Marks, T.J.** (2010) High-k organic, inorganic, and hybrid dielectrics for low-voltage organic field-effect transistors. *Chemical Reviews*, *110*, 205–39. https://doi.org/10.1021/cr9001275

[77] **Chen, X., Zhang, H., Zhang, Y., Guan, X., Zhang, Z. and Chen, D.** (2020) Low-power flexible organic field-effect transistors with solution-processable polymer-ceramic nanoparticle composite dielectrics. *Nanomaterials*, *10*, 1–9. https://doi.org/10.3390/nano10030518

[78] **Faraji, S., Danesh, E., Tate, D.J., Turner, M.L. and Majewski, L.A.** (2016) Cyanoethyl cellulose-based nanocomposite dielectric for low-voltage, solution-processed organic field-effect transistors (OFETs). *Journal of Physics D: Applied Physics*, IOP Publishing. *49*. https://doi.org/10.1088/0022-3727/49/18/185102

[79] **Faraji, S., Hashimoto, T., Turner, M.L. and Majewski, L.A.** (2015) Solution-processed nanocomposite dielectrics for low voltage operated OFETs. *Organic Electronics*, Elsevier B.V. *17*, 178–83. https://doi.org/10.1016/j.orgel.2014.12.010

[80] **Lee, Y.H., Jang, M., Lee, M.Y., Kweon, O.Y. and Oh, J.H.** (2017) Flexible Field-Effect Transistor-Type Sensors Based on Conjugated Molecules. *Chem*, Elsevier Inc. *3*, 724–63. https://doi.org/10.1016/j.chempr.2017.10.005

[81] **Gao, Y., Yi, Y., Wang, X., Meng, H., Lei, D., Yu, X.F. et al.** (2019) A Novel Hybrid-Layered Organic Phototransistor Enables Efficient Intermolecular Charge Transfer and Carrier Transport for Ultrasensitive Photodetection. *Advanced Materials*, *31*, 1–9. https://doi.org/10.1002/adma.201900763

[82] **Carr, J.A. and Chaudhary, S.** (2013) The identification, characterization and mitigation of defect states in organic photovoltaic devices: A review and outlook. *Energy and Environmental Science*, *6*, 3414–38. https://doi.org/10.1039/c3ee41860j

[83] **Lee, H., Ahn, J., Im, S., Kim, J. and Choi, W.** (2018) High-Responsivity Multilayer MoSe2 Phototransistors with Fast Response Time. *Scientific Reports*, *8*, 1–8. https://doi.org/10.1038/s41598-018-29942-1

[84] **Pesavento, P. V., Chesterfield, R.J., Newman, C.R. and Frisble, C.D.** (2004) Gated four-probe measurements on pentacene thin-film transistors: Contact resistance as a function of gate voltage and temperature. *Journal of Applied Physics*, *96*, 7312–24. https://doi.org/10.1063/1.1806533

[85] **Kymissis, I., Dimitrakopoulos, C.D. and Purushothaman, S.** (2001) High-Performance Bottom Electrode Organic. *IEEE Transactions on Electron Devices*, *48*, 1060–4.

[86] **Eggers, H., Schackmar, F., Abzieher, T., Sun, Q., Lemmer, U., Vaynzof, Y. et al.** (2020) Inkjet-Printed Micrometer-Thick Perovskite Solar Cells with Large Columnar Grains. *Advanced Energy Materials*, John Wiley & Sons, Ltd. *10*, 1903184. https://doi.org/https://doi.org/10.1002/aenm.201903184

[87] **Corzo, D., Almasabi, K., Bihar, E., Macphee, S., Rosas-Villalva, D., Gasparini, N. et al.** (2019) Digital Inkjet Printing of High-Efficiency Large-Area Nonfullerene Organic Solar Cells. *Advanced Materials Technologies*, John Wiley & Sons, Ltd. *4*, 1900040. https://doi.org/https://doi.org/10.1002/admt.201900040

[88] **Tang, W., Huang, Y., Han, L., Liu, R., Su, Y., Guo, X. et al.** (2019) Recent progress in printable organic field effect transistors. *Journal of Materials Chemistry C*, The Royal Society of Chemistry. *7*, 790–808. https://doi.org/10.1039/C8TC05485A

[89] **Feng, L., Jiang, C., Ma, H., Guo, X. and Nathan, A.** (2016) All ink-jet printed low-voltage organic field-effect transistors on flexible substrate. *Organic Electronics*, *38*, 186–92. https://doi.org/https://doi.org/10.1016/j.orgel.2016.08.019

[90] **Perinot, A., Passarella, B., Giorgio, M. and Caironi, M.** (2020) Walking the Route to GHz Solution-Processed Organic Electronics: A HEROIC Exploration. *Advanced Functional Materials*, John Wiley & Sons, Ltd. *30*, 1907641. https://doi.org/https://doi.org/10.1002/adfm.201907641

[91] **Yokota, T., Sekitani, T., Kato, yu, Kuribara, K., Zschieschang, U., Klauk, H. et al.** (2011) Low-voltage organic transistor with subfemtoliter inkjet source–drain contacts. *MRS Communications*, *1*, 3–6. https://doi.org/10.1557/mrc.2011.4

[92] **Sele, C.W., von Werne, T., Friend, R.H. and Sirringhaus, H.** (2005) Lithography-Free, Self-Aligned Inkjet Printing with Sub-Hundred-Nanometer Resolution. *Advanced Materials*, John Wiley & Sons, Ltd. *17*, 997–1001. https://doi.org/https://doi.org/10.1002/adma.200401285

[93] **Huang, Y., Tang, W., Chen, S., Han, L., Hou, X. and Guo, X.** (2019) Scalable Processing of Low Voltage Organic Field Effect Transistors With a Facile Soft-Contact Coating Approach. *IEEE Electron Device Letters*, *40*, 1945–8. https://doi.org/10.1109/LED.2019.2950345

[94] **Duan, S., Wang, T., Geng, B., Gao, X., Li, C., Zhang, J. et al.** (2020) Solution-Processed Centimeter-Scale Highly Aligned Organic Crystalline Arrays for High-Performance Organic Field-Effect Transistors. *Advanced Materials*, *32*, 1–8. https://doi.org/10.1002/adma.201908388

[95] **Yao, Y., Zhang, L., Leydecker, T. and Samorì, P.** (2018) Direct Photolithography on Molecular Crystals for High Performance Organic Optoelectronic Devices. *Journal of the American Chemical Society*, American Chemical Society. *140*, 6984–90. https://doi.org/10.1021/jacs.8b03526

[96] **Zhang, Z., Peng, B., Ji, X., Pei, K. and Chan, P.K.L.** (2017) Marangoni-Effect-Assisted Bar-Coating Method for High-Quality Organic Crystals with Compressive and Tensile Strains. *Advanced Functional Materials*, John Wiley & Sons, Ltd. *27*, 1703443. https://doi.org/https://doi.org/10.1002/adfm.201703443

[97] **Barrier, F.O.F., Processes, C.T., Of, M., Height, B., Structures, D. and Contact, O.** (1942) Physics of Semiconductor Devices, 3rd Edition by S . M. Sze and Kwok K. Ng Copyright 0 John Wiley & Sons, Inc. 3. *Physics*, 134–96.

[98] **Bansal, A.K., Hou, S., Kulyk, O., Bowman, E.M. and Samuel, I.D.W.** (2015) Wearable Organic Optoelectronic Sensors for Medicine. *Advanced Materials*,. https://doi.org/10.1002/adma.201403560

[99] **Wu, Z., Zhai, Y., Yao, W., Eedugurala, N., Zhang, S., Huang, L. et al.** (2018) The Role of Dielectric Screening in Organic Shortwave Infrared Photodiodes for Spectroscopic Image Sensing. *Advanced Functional Materials*,. https://doi.org/10.1002/adfm.201805738

[100] **Choi, C.S., Kang, H.S., Choi, W.Y., Kim, H.J., Choi, W.J., Kim, D.H. et al.** (2003) High optical responsivity of InAlAs-InGaAs metamorphic high-electron mobility transistor on GaAs substrate with composite channels. *IEEE Photonics Technology Letters*, *15*, 846–8. https://doi.org/10.1109/LPT.2003.811339

[101] **Mok, S.M., Yan, F. and Chan, H.L.W.** (2008) Organic phototransistor based on poly(3-hexylthiophene)/ TiO2 nanoparticle composite. *Applied Physics Letters*, *93*, 2–4. https://doi.org/10.1063/1.2957981

[102] **Liu, X., Dong, G., Duan, L., Wang, L. and Qiu, Y.** (2012) High performance low-voltage organic phototransistors: Interface modification and the tuning of electrical, photosensitive and memory properties. *Journal of Materials Chemistry*, *22*, 11836–42. https://doi.org/10.1039/c2jm31404e

[103] **Park, H.L., Kim, M.H. and Kim, H.** (2020) Organic phototransistor by adopting photo-responsive polymer in hybrid gate-insulator configuration. *Polymers*, *12*. https://doi.org/10.3390/polym12030527

[104] **Trujillo Herrera, C., Hong, M.J. and Labram, J.G.** (2020) Role of the Blend Ratio in Polymer:Fullerene Phototransistors. *ACS Applied Electronic Materials*, *2*, 2257–64. https://doi.org/10.1021/acsaelm.0c00445

[105] **Yang, Y., Rim, Y.S., Ok, K.C., Yang, Y.M., Chen, H., Bae, S.H. et al.** (2016) Boosting Responsivity of Organic-Metal Oxynitride Hybrid Heterointerface Phototransistor. *ACS Applied Materials and Interfaces*, *8*, 14665–70. https://doi.org/10.1021/acsami.6b02814

[106] **Zhang, X., Hou, L. and Samorì, P.** (2016) Coupling carbon nanomaterials with photochromic molecules for the generation of optically responsive materials. *Nature Communications*, *7*. https://doi.org/10.1038/ncomms11118

[107] **Wakayama, Y., Hayakawa, R., Higashiguchi, K. and Matsuda, K.** (2020) Photochromism for optically functionalized organic field-effect transistors: A comprehensive review. *Journal of Materials Chemistry C*, Royal Society of Chemistry. *8*, 10956–74. https://doi.org/10.1039/d0tc02683b

[108] **Fu, L.N., Leng, B., Li, Y.S. and Gao, X.K.** (2016) Photoresponsive organic field-effect transistors involving photochromic molecules. *Chinese Chemical Letters*, *27*, 1319–29. https://doi.org/10.1016/j.cclet.2016.06.045

[109] **Shen, Q., Wang, L., Liu, S., Cao, Y., Gan, L., Guo, X. et al.** (2010) Photoactive gate dielectrics. *Advanced Materials*, *22*, 3282–7. https://doi.org/10.1002/adma.201000471

[110] **Kang, M., Cha, A.N., Lee, S.A., Lee, S.K., Bae, S., Jeon, D.Y. et al.** (2019) Light-sensitive charge storage medium with spironaphthooxazine molecule-polymer blends for dual-functional organic phototransistor memory. *Organic Electronics*, Elsevier B.V. 105554. https://doi.org/10.1016/j.orgel.2019.105554

[111] **Ishiguro, Y., Hayakawa, R., Yasuda, T., Chikyow, T. and Wakayama, Y.** (2013) Unique device operations by combining optical-memory effect and electrical-gate modulation in a photochromism-based dual-gate transistor. *ACS Applied Materials and Interfaces*, *5*, 9726–31. https://doi.org/10.1021/am402833k

[112] **Hayakawa, R., Higashiguchi, K., Matsuda, K., Chikyow, T. and Wakayama, Y.** (2013) Optically and electrically driven organic thin film transistors with diarylethene photochromic channel layers. *ACS Applied Materials and Interfaces*, *5*, 3625–30. https://doi.org/10.1021/am400030z

[113] **Osaka, I. and Takimiya, K.** (2015) Backbone orientation in semiconducting polymers. *Polymer*, Elsevier Ltd. *59*, A1–15. https://doi.org/10.1016/j.polymer.2014.12.066

[114] **Xu, T. and Yu, L.** (2014) How to design low bandgap polymers for highly efficient organic solar cells. *Materials Today*, Elsevier Ltd. *17*, 11–5. https://doi.org/10.1016/j.mattod.2013.12.005

[115] **Isci, R., Gunturkun, D., Yalin, A.S. and Ozturk, T.** (2021) Copolymers of 4-thieno[3,2-b]thiophen-3-ylbenzonitrile with anthracene and biphenyl; synthesis, characterization, electronic, optical, and thermal properties. *Journal of Polymer Science*, John Wiley & Sons, Ltd. *59*, 117–23. https://doi.org/https://doi.org/10.1002/pol.20200635

[116] **Bronstein, H., Chen, Z., Ashraf, R.S., Zhang, W., Du, J., Durrant, J.R. et al.** (2011) Thieno[3,2- b]thiophene-diketopyrrolopyrrole-containing polymers for high-performance organic field-effect transistors and organic photovoltaic devices. *Journal of the American Chemical Society*, *133*, 3272–5. https://doi.org/10.1021/ja110619k

[117] **Cho, M.Y., Kim, S.J., Han, Y.D., Park, D.H., Kim, K.H., Choi, D.H. et al.** (2008) Highly sensitive, photocontrolled, organic thin-film transistors using soluble star-shaped conjugated molecules. *Advanced Functional Materials*, *18*, 2905–12. https://doi.org/10.1002/adfm.200800358

[118] **Han, S.T., Zhou, Y., Yang, Q.D., Lee, C.S. and Roy, V.A.L.** (2013) Poly(3-hexylthiophene)/gold nanoparticle hybrid system with an enhanced photoresponse for light-controlled electronic devices. *Particle and Particle Systems Characterization*, *30*, 599–605. https://doi.org/10.1002/ppsc.201300005

[119] **Han, S.T., Zhou, Y., Xu, Z.X. and Roy, V.A.L.** (2012) Controllable threshold voltage shifts of polymer transistors and inverters by utilizing gold nanoparticles. *Applied Physics Letters*,. https://doi.org/10.1063/1.4737422

[120] **Nam, S., Seo, J., Park, S., Lee, S., Jeong, J., Lee, H. et al.** (2013) Hybrid phototransistors based on bulk heterojunction films of poly(3-hexylthiophene) and zinc oxide nanoparticle. *ACS Applied Materials and Interfaces*, *5*, 1385–92. https://doi.org/10.1021/am302765a

[121] **Lim, D.H., Lim, D.H., Kang, M., Jang, S.Y., Hwang, K., Kim, I.B. et al.** (2020) Unsymmetrical Small Molecules for Broad-Band Photoresponse and Efficient Charge Transport in Organic Phototransistors. *ACS Applied Materials and Interfaces*, *12*, 25066–74. https://doi.org/10.1021/acsami.0c02229

[122] **Park, J., Kim, H., Kim, T., Lee, C., Song, D.I. and Kim, Y.** (2019) Effect of top channel thickness in near infrared organic phototransistors with conjugated polymer gate-sensing layers. *Electronics (Switzerland)*, *8*. https://doi.org/10.3390/electronics8121493

[123] **Li, F., Chen, Y., Ma, C., Buttner, U., Leo, K. and Wu, T.** (2017) High-Performance Near-Infrared Phototransistor Based on n-Type Small-Molecular Organic Semiconductor. *Advanced Electronic Materials*, *3*. https://doi.org/10.1002/aelm.201600430

[124] **Vella, J.H., Huang, L., Eedugurala, N., Mayer, K.S., Ng, T.N. and Azoulay, J.D.** (2021) Broadband infrared photodetection using a narrow bandgap conjugated polymer. *Science Advances*, *7*, 1–7. https://doi.org/10.1126/sciadv.abg2418

[125] **Lin, Y.-H., Huang, W., Pattanasattayavong, P., Lim, J., Li, R., Sakai, N. et al.** (2019) Deciphering photocarrier dynamics for tuneable high-performance perovskite-organic semiconductor heterojunction phototransistors. *Nature Communications*, *10*, 4475. https://doi.org/10.1038/s41467-019-12481-2

[126] **Isci, R., Tekin, E., Kaya, K., Piravadili Mucur, S., Gorkem, S.F. and Ozturk, T.** (2020) Tetraphenylethylene substituted thienothiophene and dithienothiophene derivatives: synthesis, optical properties and OLED applications. *Journal of Materials Chemistry C*, The Royal Society of Chemistry. *8*, 7908–15. https://doi.org/10.1039/D0TC01715A

[127] **Kim, S., Lee, D., Lee, J., Cho, Y., Kang, S.-H., Choi, W. et al.** (2021) Diazapentalene-Containing Ultralow-Band-Gap Copolymers for High-Performance Near-Infrared Organic Phototransistors. *Chemistry of Materials*, American Chemical Society. *33*, 7499–508. https://doi.org/10.1021/acs.chemmater.1c02409

[128] **Singh, A.K., Chourasia, N.K., Pal, B.N., Pandey, A. and Chakrabarti, P.** (2020) Low Operating Voltage Solution Processed (Li_2ZnO_2) Dielectric and (SnO_2) Channel-Based Medium Wave UV-B Phototransistor for Application in Phototherapy. *IEEE Transactions on Electron Devices*, *67*, 2028–34. https://doi.org/10.1109/TED.2020.2978536

[129] **Santiago, I.** (2020) Trends and Innovations in Biosensors for COVID-19 Mass Testing. *ChemBioChem*, *21*, 2880–9. https://doi.org/10.1002/cbic.202000250

[130] **Choi, J.R.** (2020) Development of Point-of-Care Biosensors for COVID-19. *Frontiers in Chemistry*, *8*. https://doi.org/10.3389/fchem.2020.00517

[131] **Asif, M., Ajmal, M., Ashraf, G., Muhammad, N., Aziz, A., Iftikhar, T. et al.** (2020) The role of biosensors in coronavirus disease-2019 outbreak. *Current Opinion in Electrochemistry*, Elsevier Ltd. *23*, 174–84. https://doi.org/10.1016/j.coelec.2020.08.011

[132] **Şahin, S., Ünlü, C. and Trabzon, L.** (2021) Affinity biosensors developed with quantum dots in microfluidic systems. *Emergent Materials*, 1–23. https://doi.org/10.1007/s42247-021-00195-5

[133] **Lee, I., Park, N., Lee, H., Hwang, C., Kim, J.H. and Park, S.** (2021) Systematic review on human skin-compatible wearable photoplethysmography sensors. *Applied Sciences (Switzerland)*, *11*, 1–21. https://doi.org/10.3390/app11052313

[134] **Parak, J. and Korhonen, I.** (2014) Evaluation of wearable consumer heart rate monitors based on photopletysmography. *2014 36th Annual International Conference of the IEEE Engineering in Medicine and Biology Society, EMBC 2014*, 3670–3. https://doi.org/10.1109/EMBC.2014.6944419

[135] **Rozi, R.M., Usman, S., Mohd Ali, M.A. and Reaz, M.B.I.** (2012) Second derivatives of photoplethysmography (PPG) for estimating vascular aging of atherosclerotic patients. *2012 IEEE-EMBS Conference on Biomedical Engineering and Sciences, IECBES 2012*, 256–9. https://doi.org/10.1109/IECBES.2012.6498064

[136] **Beachey, W.** (2007) Respiratory Care Anatomy and Physiology: Foundations for Clinical Practice. 2nd edition. St Louis: Mosby Elsevier.

[137] **Lee, H., Ko, H. and Lee, J.** (2016) Reflectance pulse oximetry: Practical issues and limitations. *ICT Express*, Elsevier B.V. *2*, 195–8. https://doi.org/10.1016/j.icte.2016.10.004

[138] **Lauterbach, C.J., Romano, P.A., Greisler, L.A., Brindle, R.A., Ford, K.R. and Kuennen, M.R.** (2020) Accuracy and Reliability of Commercial Wrist-Worn Pulse Oximeter During Normobaric Hypoxia Exposure Under Resting Conditions. *Research Quarterly for Exercise and Sport*, Routledge. *00*, 1–10. https://doi.org/10.1080/02701367.2020.1759768

[139] **Nitzan, M., Romem, A. and Koppel, R.** (2014) Pulse oximetry: Fundamentals and technology update. *Medical Devices: Evidence and Research*, ***7***, 231–9. https://doi.org/10.2147/MDER.S47319

[140] **Tao, J., Liu, D., Qin, Z., Shao, B., Jing, J., Li, H. et al.** (2020) Organic UV-Sensitive Phototransistors Based on Distriphenylamineethynylpyrene Derivatives with Ultra-High Detectivity Approaching 1018. *Advanced Materials*, *32*, 1–9. https://doi.org/10.1002/adma.201907791

[141] **Jiang, C.Y., Tsai, C.H., Tzou, C.Y., Hsu, F.C. and Chen, Y.F.** (2020) Magnetically controllable and flexible phototransistor for artificial intelligent skin with additional perception. *Organic Electronics*, Elsevier B.V. *85*, 105849. https://doi.org/10.1016/j.orgel.2020.105849

[142] **Zhong, J., Wu, X., Lan, S., Fang, Y., Chen, H. and Guo, T.** (2018) High Performance Flexible Organic Phototransistors with Ultrashort Channel Length. *ACS Photonics*, *5*, 3712–22. https://doi.org/10.1021/acsphotonics.8b00729

[143] **Liu, X., Lee, E.K., Kim, D.Y., Yu, H. and Oh, J.H.** (2016) Flexible Organic Phototransistor Array with Enhanced Responsivity via Metal-Ligand Charge Transfer. *ACS Applied Materials and Interfaces*, *8*, 7291–9. https://doi.org/10.1021/acsami.5b11523

[144] **Lee, C., Kim, H. and Kim, Y.** (2021) Short-wave infrared organic phototransistors with strong infrared-absorbing polytriarylamine by electron-transfer doping. *Npj Flexible Electronics*, Springer US. *5*, 1–9. https://doi.org/10.1038/s41528-021-00105-z

[145] **Li, Q., Ran, Y., Shi, W., Qin, M., Sun, Y., Kuang, J. et al.** (2021) High-performance near-infrared polymeric phototransistors realized by combining cross-linked polymeric semiconductors and bulk heterojunction bilayer structures. *Applied Materials Today*, Elsevier Ltd. *22*, 100899. https://doi.org/10.1016/j.apmt.2020.100899

[146] **Yu, Y., Ma, Q., Ling, H., Li, W., Ju, R., Bian, L. et al.** (2019) Small-Molecule-Based Organic Field-Effect Transistor for Nonvolatile Memory and Artificial Synapse. *Advanced Functional Materials*, *29*, 1–31. https://doi.org/10.1002/adfm.201904602

[147] **Gao, S., Yi, X., Shang, J., Liu, G. and Li, R.-W.** (2019) Organic and hybrid resistive switching materials and devices. *Chemical Society Reviews*, The Royal Society of Chemistry. *48*, 1531–65. https://doi.org/10.1039/C8CS00614H

[148] **Wang, H., Zhao, Q., Ni, Z., Li, Q., Liu, H., Yang, Y. et al.** (2018) A Ferroelectric/Electrochemical Modulated Organic Synapse for Ultraflexible, Artificial Visual-Perception System. *Advanced Materials (Deerfield Beach, Fla)*, Germany. *30*, e1803961. https://doi.org/10.1002/adma.201803961

[149] **Wang, Z., Zhang, S.-R., Zhou, L., Mao, J.-Y., Han, S.-T., Ren, Y. et al.** (2019) Functional Non-Volatile Memory Devices: From Fundamentals to Photo-Tunable Properties. *Physica Status Solidi (RRL) – Rapid Research Letters*, John Wiley & Sons, Ltd. *13*, 1800644. https://doi.org/https://doi.org/10.1002/pssr.201800644

[150] **Zhao, Q., Wang, H., Jiang, L., Zhen, Y., Dong, H. and Hu, W.** (2017) Solution-Processed Flexible Organic Ferroelectric Phototransistor. *ACS Applied Materials and Interfaces*, *9*, 43880–5. https://doi.org/10.1021/acsami.7b13709

[151] **Chiang, Y.C., Hung, C.C., Lin, Y.C., Chiu, Y.C., Isono, T., Satoh, T. et al.** (2020) High-Performance Nonvolatile Organic Photonic Transistor Memory Devices using Conjugated Rod–Coil Materials as a Floating Gate. *Advanced Materials*, *32*, 1–8. https://doi.org/10.1002/adma.202002638

[152] **Xu, X., Deng, W., Zhang, X., Huang, L., Wang, W., Jia, R. et al.** (2019) Dual-Band, High-Performance Phototransistors from Hybrid Perovskite and Organic Crystal Array for Secure Communication Applications. *ACS Nano*, *13*, 5910–9. https://doi.org/10.1021/acsnano.9b01734

[153] **Huang, T.Y., Chen, C.H., Lin, C.C., Lee, Y.J., Liu, C.L. and Liou, G.S.** (2019) UV-sensing organic phototransistor memory devices with a doped organic polymer electret composed of triphenylamine-based aggregation-induced emission luminogens. *Journal of Materials Chemistry C*, *7*, 11014–21. https://doi.org/10.1039/c9tc03607e

[154] **Medintz, I.L., Uyeda, H.T., Goldman, E.R. and Mattoussi, H.** (2005) Quantum dot bioconjugates for imaging, labelling and sensing. *Nature Materials*, *4*, 435–46. https://doi.org/10.1038/nmat1390

[155] **Hu, J., Odom, T.W. and Lieber, C.M.** (1999) Chemistry and Physics in One Dimension: Synthesis and Properties of Nanowires and Nanotubes. *Accounts of Chemical Research*, American Chemical Society. *32*, 435–45. https://doi.org/10.1021/ar9700365

[156] **Novoselov, K.S., Jiang, D., Schedin, F., Booth, T.J., Khotkevich, V. V, Morozov, S. V et al.** (2005) Two-dimensional atomic crystals. *Proceedings of the National Academy of Sciences of the United States of America*, *102*, 10451 LP – 10453. https://doi.org/10.1073/pnas.0502848102

[157] **Fang, H. and Hu, W.** (2017) Photogating in Low Dimensional Photodetectors. *Advanced Science*, John Wiley & Sons, Ltd. *4*, 1700323. https://doi.org/https://doi.org/10.1002/advs.201700323

[158] **He, Z., Han, J., Du, X., Cao, L., Wang, J., Zheng, C. et al.** (2021) Photomemory and Pulse Monitoring Featured Solution-Processed Near-Infrared Graphene/Organic Phototransistor with Detectivity of 2.4 × 1013 Jones. *Advanced Functional Materials*, *31*, 1–8. https://doi.org/10.1002/adfm.202103988

[159] **Ljubic, D., Liu, W., González-Espinoza, C.E., Hu, N.-X., Wu, Y. and Zhu, S.** (2017) Binary Blends of Polyimide and Benzothienobenzothiophene for High-Performance Solution-Processed Organic Phototransistors. *Advanced Electronic Materials*, John Wiley & Sons, Ltd. *3*, 1700284. https://doi.org/https://doi.org/10.1002/aelm.201700284

[160] **Wang, C., Zhang, X. and Hu, W.** (2020) Organic photodiodes and phototransistors toward infrared detection: Materials, devices, and applications. *Chemical Society Reviews*, Royal Society of Chemistry. *49*, 653–70. https://doi.org/10.1039/c9cs00431a

[161] **Xie, C., Liu, C.K., Loi, H.L. and Yan, F.** (2020) Perovskite-Based Phototransistors and Hybrid Photodetectors. *Advanced Functional Materials*, *30*, 1–28. https://doi.org/10.1002/adfm.201903907

[162] **Liu, J., Wang, Y., Wen, H., Bao, Q., Shen, L. and Ding, L.** (2020) Organic Photodetectors: Materials, Structures, and Challenges. *Solar RRL*, *4*, 1–8. https://doi.org/10.1002/solr.202000139

[163] **Tavasli, A., Gurunlu, B., Gunturkun, D., Isci, R. and Faraji, S.** (2022) A Review on Solution-Processed Organic Phototransistors and Their Recent Developments. *Electronics*, *11*, 316. https://doi.org/10.3390/electronics11030316

[164] **Dou, L., Liu, Y., Hong, Z., Li, G. and Yang, Y.** (2015) Low-Bandgap Near-IR Conjugated Polymers/Molecules for Organic Electronics. *Chemical Reviews*, *115*, 12633–65. https://doi.org/10.1021/acs.chemrev.5b00165

[165] **Xu, H., Liu, J., Zhang, J., Zhou, G., Luo, N. and Zhao, N.** (2017) Flexible Organic/Inorganic Hybrid Near-Infrared Photoplethysmogram Sensor for Cardiovascular Monitoring. *Advanced Materials*, *29*, 1–6. https://doi.org/10.1002/adma.201700975

[166] **Kim, M.-K. and Lee, J.-S.** (2019) Ferroelectric Analog Synaptic Transistors. *Nano Letters*, American Chemical Society. *19*, 2044–50. https://doi.org/10.1021/acs.nanolett.9b00180

[167] **Lin, Y.-C., Yang, W.-C., Chiang, Y.-C. and Chen, W.-C.** (2022) Recent Advances in Organic Phototransistors: Nonvolatile Memory, Artificial Synapses, and Photodetectors. *Small Science*, *2100109*, 2100109. https://doi.org/10.1002/smsc.202100109

[168] **Li, J., Fu, W.H., Li, L.K., Jiang, D.L., He, L.C., Zhu, W.Q. et al.** (2021) Recent advances in solid electrolytes for synaptic transistors. *Organic Electronics*, Elsevier B.V. *95*, 106196. https://doi.org/10.1016/j.orgel.2021.106196

[169] **Lu, K., Li, X., Sun, Q., Pang, X., Chen, J., Minari, T. et al.** (2021) Solution-processed electronics for artificial synapses. *Materials Horizons*, The Royal Society of Chemistry. *8*, 447–70. https://doi.org/10.1039/D0MH01520B

[170] **Yu, Y., Ma, Q., Ling, H., Li, W., Ju, R., Bian, L. et al.** (2019) Small-Molecule-Based Organic Field-Effect Transistor for Nonvolatile Memory and Artificial Synapse. *Advanced Functional Materials*, *29*, 1–31. https://doi.org/10.1002/adfm.201904602

[171] **Xie, W., Menke, S.M., Frisbie, C.D. and Holmes, R.J.** (2016) Experimental Characterization of Charge and Exciton Transport in Organic Semiconductors. *The WSPC Reference on Organic Electronics: Organic Semiconductors*, *1*, 231–91. https://doi.org/10.1142/9678

[172] **Katz, H.E., Johnson, J., Lovinger, A.J. and Li, W.** (2000) Naphthalenetetracarboxylic Diimide-Based n-Channel Transistor Semiconductors: Structural Variation and Thiol-Enhanced Gold Contacts. *Journal of the American Chemical Society*, American Chemical Society. *122*, 7787–92. https://doi.org/10.1021/ja000870g

[173] **Facchetti, A.** (2009) Electroactive Oligothiophenes and Polythiophenes for Organic Field Effect Transistors. *Handbook of Thiophene-Based Materials*, 1st ed. John Wiley & Sons Ltd, The Atrium, Southern Gate, Chichester, West Sussex, PO19 8SQ, United Kingdom. p. 595–646. https://doi.org/https://doi.org/10.1002/9780470745533.ch16

[174] **Li, E., Gao, C., Yu, R., Wang, X., He, L., Hu, Y. et al.** (2022) MXene based saturation organic vertical photoelectric transistors with low subthreshold swing. *Nature Communications*, *13*, 2898. https://doi.org/10.1038/s41467-022-30527-w

[175**] Feng, G., Jiang, J., Li, Y., Xie, D., Tian, B. and Wan, Q.** (2021) Flexible Vertical Photogating Transistor Network with an Ultrashort Channel for In-Sensor Visual Nociceptor. *Advanced Functional Materials*, John Wiley and Sons Inc. *31*. https://doi.org/10.1002/adfm.202104327

[176] **Pesavento, P. V., Chesterfield, R.J., Newman, C.R. and Frisble, C.D.** (2004) Gated four-probe measurements on pentacene thin-film transistors: Contact resistance as a function of gate voltage and temperature. *Journal of Applied Physics*, *96*, 7312–24. https://doi.org/10.1063/1.1806533

[177] **Ren, X., Yang, F., Gao, X., Cheng, S., Zhang, X., Dong, H. et al.** (2018) Organic Field-Effect Transistor for Energy-Related Applications: Low-Power-Consumption Devices, Near-Infrared Phototransistors, and Organic Thermoelectric Devices. *Advanced Energy Materials, 8*, 1–27. https://doi.org/10.1002/aenm.201801003

[178] **Cavallari, M.R., Pastrana, L.M., Sosa, C.D.F., Marquina, A.M.R., Izquierdo, J.E.E., Fonseca, F.J. et al.** (2021) Organic thin-film transistors as gas sensors: A review. *Materials*, *14*, 1–32. https://doi.org/10.3390/ma14010003

[179] **Mohammadian, N. and Majewski, L.A.** (2020) High Capacitance Dielectrics for Low Voltage Operated OFETs. In: Hoyos LAME-KHYE-JJS, editor. *Integrated Circuits/Microchips*, IntechOpen, Rijeka. p. Ch. 5. https://doi.org/10.5772/intechopen.91772

[180] **Ireneusz, G., Jung, J., Wiosna–Salyga, G., Chapran, M., Luczak, A., Dupont, B.G.R. et al.** (2017) Role of Charge – carrier Trapping in Organic. *Display and Imaging*, *2*, 279–319.

[181] **Feriancová, L., Kmentová, I., Micjan, M., Pavúk, M., Weis, M. and Putala, M.** (2021) Synthesis and effect of the structure of bithienyl-terminated surfactants for dielectric layer modification in organic transistor. *Materials*, *14*. https://doi.org/10.3390/ma14216345

[182] **Kymissis, I.** (2009) Organic field effect transistors: Theory, Fabrication and Characterization. 1st ed. Chandrakasan A, editor. Springer. Springer, Boston, MA, 233 Spring Street, New York, NY 10013, USA. https://doi.org/10.1007/978-0-387-92134-1

[183] **Seck, M., Mohammadian, N., Diallo, A.K., Faraji, S., Erouel, M., Bouguila, N. et al.** (2020) Organic FETs using biodegradable almond gum as gate dielectric: A promising way towards green electronics. *Organic Electronics*, North-Holland. *83*, 105735. https://doi.org/10.1016/J.ORGEL.2020.105735

[184] **Tall, A., Faraji, S., Diallo, A.K., Mohammadian, N., Erouel, M., Seck, M. et al.** (2022) Khaya gum – a natural and eco-friendly biopolymer dielectric for low-cost organic field-effect transistors (OFETs). *Journal of Materials Science: Materials in Electronics*, Springer. *33*, 15283–95. https://doi.org/10.1007/s10854-022-08388-2

[185] **Faraji, S., Tall, A., Mohammadian, N., Seck, M., Saadi, M., Tavasli, A. et al.** (2023) Towards sustainable, solution-processed organic field-effect transistors using cashew gum as the gate dielectric. *Frontiers in Materials*, *10*. https://doi.org/10.3389/fmats.2023.1280543

[186] **Stephen, M., Nawaz, A., Lee, S.Y., Sonar, P. and Leong, W.L.** (2023) Biodegradable Materials for Transient Organic Transistors. Adv Funct Mater. John Wiley and Sons Inc. https://doi.org/10.1002/adfm.202208521

[187] **Kim, J., Cho, S., Kim, Y.H. and Park, S.K.** (2014) Highly-sensitive solution-processed 2,8-difluoro-5,11- bis(triethylsilylethynyl) anthradithiophene (diF-TESADT) phototransistors for optical sensing applications. *Organic Electronics*, Elsevier B.V. *15*, 2099–106. https://doi.org/10.1016/j.orgel.2014.06.007

[188] **Chen, X., Zhang, H., Zhang, Y., Guan, X., Zhang, Z. and Chen, D.** (2020) Low-power flexible organic field-effect transistors with solution-processable polymer-ceramic nanoparticle composite dielectrics. *Nanomaterials*, *10*, 1–9. https://doi.org/10.3390/nano10030518

[189] **Carr, J.A. and Chaudhary, S.** (2013) The identification, characterization and mitigation of defect states in organic photovoltaic devices: A review and outlook. *Energy and Environmental Science*, *6*, 3414–38. https://doi.org/10.1039/c3ee41860j

[190] **Sze, S. and Ng, K.K.** (2006) Photodetectors and Solar Cells. *Physics of Semiconductor Devices*, 3rd ed. John Wiley and Sons, Hoboken, New Jersey, USA. p. 663–742. https://doi.org/https://doi.org/10.1002/9780470068328.ch13

[191] **Lee, H., Ahn, J., Im, S., Kim, J. and Choi, W.** (2018) High-Responsivity Multilayer MoSe2 Phototransistors with Fast Response Time. *Scientific Reports*, *8*, 1–8. https://doi.org/10.1038/s41598-018-29942-1

[192] **Chu, Y., Wu, X., Lu, J., Liu, D., Du, J., Zhang, G. et al.** (2016) Photosensitive and Flexible Organic Field-Effect Transistors Based on Interface Trapping Effect and Their Application in 2D Imaging Array. *Advanced Science*, *3*, 1–6. https://doi.org/10.1002/advs.201500435

[193] **Zhu, M., Lv, S., Wang, Q., Zhang, G., Lu, H. and Qiu, L.** (2016) Enhanced near-infrared photoresponse of organic phototransistors based on single-component donor-acceptor conjugated polymer nanowires. *Nanoscale*, *8*, 7738–48. https://doi.org/10.1039/c5nr09003b

[194] **Chou, Y.H., Takasugi, S., Goseki, R., Ishizone, T. and Chen, W.C.** (2014) Nonvolatile organic field-effect transistor memory devices using polymer electrets with different thiophene chain lengths. *Polymer Chemistry*, *5*, 1063–71. https://doi.org/10.1039/c3py01124k

[195] **Shou, M., Zhang, Q., Li, H., Xiong, S., Hu, B., Zhou, J. et al.** (2021) Ultrahigh Detectivity in Spatially Separated Hole/Electron Dual Traps Based Near-Infrared Organic Phototransistor. *Advanced Optical Materials*, *9*, 1–8. https://doi.org/10.1002/adom.202002031

[196] **Lai, S., Casula, G., Ricci, P.C., Cosseddu, P. and Bonfiglio, A.** (2020) All-organic, low voltage, transparent and compliant organic field-effect transistor fabricated by means of large-area, cost-effective techniques. *Applied Sciences (Switzerland)*, *10*. https://doi.org/10.3390/APP10196656

[197] **Vaynzof, Y.** (2020) The Future of Perovskite Photovoltaics—Thermal Evaporation or Solution Processing? *Advanced Energy Materials*, John Wiley & Sons, Ltd. *10*, 2003073. https://doi.org/https://doi.org/10.1002/aenm.202003073

[198] **Wang, Z., Huang, L., Zhu, X., Zhou, X. and Chi, L.** (2017) An Ultrasensitive Organic Semiconductor NO2 Sensor Based on Crystalline TIPS-Pentacene Films. *Advanced Materials*, John Wiley & Sons, Ltd. *29*, 1703192. https://doi.org/https://doi.org/10.1002/adma.201703192

[199] **Zhang, Q., Jin, T., Ye, X., Geng, D., Chen, W. and Hu, W.** (2021) Organic Field Effect Transistor-Based Photonic Synapses: Materials, Devices, and Applications. *Advanced Functional Materials*, John Wiley & Sons, Ltd. *31*, 2106151. https://doi.org/https://doi.org/10.1002/adfm.202106151

[200] **Wang, Y., Zhang, J., Zhang, S. and Huang, J.** (2021) OFET chemical sensors: Chemical sensors based on ultrathin organic field-effect transistors. *Polymer International*, John Wiley & Sons, Ltd. *70*, 414–25. https://doi.org/https://doi.org/10.1002/pi.6095

[201] **Dai, S., Wu, X., Liu, D., Chu, Y., Wang, K., Yang, B. et al.** (2018) Light-Stimulated Synaptic Devices Utilizing Interfacial Effect of Organic Field-Effect Transistors. *ACS Applied Materials & Interfaces*, American Chemical Society. *10*, 21472–80. https://doi.org/10.1021/acsami.8b05036

[202] **Ma, L., Li, Z., Chen, B., Xue, P., Wang, Z., Wu, Y. et al.** (2022) The Impact of Benzothiadiazole on the Optoelectronic Performance of Polymer/PC71BM Blend Films and Their Application in NIR Phototransistors. *Advanced Electronic Materials*, John Wiley & Sons, Ltd., 2101297. https://doi.org/https://doi.org/10.1002/aelm.202101297

[203] **Mei, J., Diao, Y., Appleton, A.L., Fang, L. and Bao, Z.** (2013) Integrated materials design of organic semiconductors for field-effect transistors. *Journal of the American Chemical Society*, 135, 6724–46. https://doi.org/10.1021/ja400881n

[204] **Yunus, Y., Mahadzir, N.A., Ansari, M.N.M., Aziz, T.H.T.A., Afdzaluddin, A.M., Anwar, H. et al.** (2022) Review of the Common Deposition Methods of Thin-Film Pentacene, Its Derivatives, and Their Performance. *Polymers*, *14*. https://doi.org/10.3390/polym14061112

[205] **Szulczewski, G., Sanvito, S. and Coey, M.** (2009) A spin of their own. *Nature Materials*, Nature Publishing Group. *8*, 693–5. https://doi.org/10.1038/nmat2518

[206] **Schlesinger, R.** (2017) Chapter 2 Fundamentals. *Energy-Level Control at Hybrid Inorganic/Organic Semiconductor Interfaces, 1st Ed*, 1st ed. Springer International Publishing AG, Springer Theses. p. 7–45. https://doi.org/10.1007/978-3-319-46624-8

[207] **Kertesz, M., Yang, S., Tian, Y., Ho, H.-A. and Leclerc, M.** (2009) Energy Gaps and their Control in Thiophene-Based Polymers and Oligomers. *Handbook of Thiophene-Based Materials*, p. 341–64. https://doi.org/https://doi.org/10.1002/9780470745533.ch7

[208] **Hu, J., Wei, W., Ke, S., Zeng, X. and Lin, P.** (2019) A novel and sensitive sarcosine biosensor based on organic electrochemical transistor. *Electrochimica Acta*, Elsevier Ltd. *307*, 100–6. https://doi.org/10.1016/j.electacta.2019.03.180

[209] **Quirós-Solano, W.F., Gaio, N., Silvestri, C., Pandraud, G. and Sarro, P.M.** (2016) PEDOT:PSS: A Conductive and Flexible Polymer for Sensor Integration in Organ-on-Chip Platforms. *Procedia Engineering*, *168*, 1184–7. https://doi.org/https://doi.org/10.1016/j.proeng.2016.11.401

[210] **Liu, K., Ouyang, B., Guo, X., Guo, Y. and Liu, Y.** (2022) Advances in flexible organic field-effect transistors and their applications for flexible electronics. *Npj Flexible Electronics*, Springer US. *6*. https://doi.org/10.1038/s41528-022-00133-3

[211] **Lin, C.-C., Velusamy, A., Tung, S.-H., Osaka, I., Chen, M.-C. and Liu, C.-L.** (2022) Tunable Photoelectric Properties of n-Type Semiconducting Polymer:Small Molecule Blends for Red Light Sensing Phototransistors. *Advanced Optical Materials*, John Wiley & Sons, Ltd., 2102650. https://doi.org/https://doi.org/10.1002/adom.202102650

[212] **Calvi, S., Rapisarda, M., Valletta, A., Scagliotti, M., De Rosa, S., Tortora, L. et al.** (2022) Highly sensitive organic phototransistor for flexible optical detector arrays. *Organic Electronics*, Elsevier B.V. *102*, 106452. https://doi.org/10.1016/j.orgel.2022.106452

[213] **Tang, C.G., Hou, K. and Leong, W.L.** (2024) The Quest for Air Stability in Organic Semiconductors. *Chemistry of Materials*, American Chemical Society. *36*, 28–53. https://doi.org/10.1021/acs.chemmater.3c02093

[214] **Li, F., Chen, Y., Ma, C., Buttner, U., Leo, K. and Wu, T.** (2017) High-Performance Near-Infrared Phototransistor Based on n-Type Small-Molecular Organic Semiconductor. *Advanced Electronic Materials*, *3*. https://doi.org/10.1002/aelm.201600430

[215] **Chai, S., Wen, S.-H. and Han, K.-L.** (2011) Understanding electron-withdrawing substituent effect on structural, electronic and charge transport properties of perylene bisimide derivatives. *Organic Electronics*, *12*, 1806–14. https://doi.org/https://doi.org/10.1016/j.orgel.2011.07.008

[216] **Ling, M.-M., Erk, P., Gomez, M., Koenemann, M., Locklin, J. and Bao, Z.** (2007) Air-Stable n-Channel Organic Semiconductors Based on Perylene Diimide Derivatives without Strong Electron Withdrawing Groups. *Advanced Materials*, John Wiley & Sons, Ltd. *19*, 1123–7. https://doi.org/https://doi.org/10.1002/adma.200601705

[217] **Monalisha, P., Kumar, A.P.S., Wang, X.R. and Piramanayagam, S.N.** (2022) Emulation of Synaptic Plasticity on a Cobalt-Based Synaptic Transistor for Neuromorphic Computing. *ACS Applied Materials & Interfaces*, American Chemical Society. *14*, 11864–72. https://doi.org/10.1021/acsami.1c19916

[218] **Zhang, F., Li, C., Li, Z., Dong, L. and Zhao, J.** (2023) Recent progress in three-terminal artificial synapses based on 2D materials: from mechanisms to applications. *Microsystems & Nanoengineering*, *9*, 16. https://doi.org/10.1038/s41378-023-00487-2

[219] **Marquez, M.M. and Chacron, M.J.** (2020) Chapter 25 - Serotonin and sensory processing. In: Müller CP, and Cunningham KA, editors. *Handbook of Behavioral Neuroscience*, Elsevier. p. 449–59. https://doi.org/https://doi.org/10.1016/B978-0-444-64125-0.00025-6

[220] **Liu, X., Huang, W., Kai, C., Yin, L., Wang, Y., Liu, X. et al.** (2023) Photogated Synaptic Transistors Based on the Heterostructure of 4H-SiC and Organic Semiconductors for Neuromorphic Ultraviolet Vision. *ACS Applied Electronic Materials*, American Chemical Society. *5*, 367–74. https://doi.org/10.1021/acsaelm.2c01390

[221] **Yu, Y., Ma, Q., Ling, H., Li, W., Ju, R., Bian, L. et al.** (2019) Small-Molecule-Based Organic Field-Effect Transistor for Nonvolatile Memory and Artificial Synapse. *Advanced Functional Materials*, John Wiley & Sons, Ltd. *29*, 1904602. https://doi.org/https://doi.org/10.1002/adfm.201904602

[222] **Yu, J., Wang, Y., Qin, S., Gao, G., Xu, C., Lin Wang, Z. et al.** (2022) Bioinspired interactive neuromorphic devices. Materials Today. Elsevier B.V. p. 158–82. https://doi.org/10.1016/j.mattod.2022.09.012

[223] **Shan, L., Chen, Q., Yu, R., Gao, C., Liu, L., Guo, T. et al.** (2023) A sensory memory processing system with multi-wavelength synaptic-polychromatic light emission for multi-modal information recognition. *Nature Communications*, *14*, 2648. https://doi.org/10.1038/s41467-023-38396-7

[224] **Liu, Y., Liu, D., Gao, C., Zhang, X., Yu, R., Wang, X. et al.** (2022) Self-powered high-sensitivity all-in-one vertical tribo-transistor device for multi-sensing-memory-computing. *Nature Communications*, *13*, 7917. https://doi.org/10.1038/s41467-022-35628-0

[225] **Yu, R., He, L., Gao, C., Zhang, X., Li, E., Guo, T. et al.** (2022) Programmable ferroelectric bionic vision hardware with selective attention for high-precision image classification. *Nature Communications*, *13*, 7019. https://doi.org/10.1038/s41467-022-34565-2

[226] **Liu, G., Li, Q., Shi, W., Liu, Y., Liu, K., Yang, X. et al.** (2022) Ultralow-Power and Multisensory Artificial Synapse Based on Electrolyte-Gated Vertical Organic Transistors. *Advanced Functional Materials*, *2200959*, 1–10. https://doi.org/10.1002/adfm.202200959

[227] **Shi, J., Jie, J., Deng, W., Luo, G., Fang, X., Xiao, Y. et al.** (2022) A Fully Solution-Printed Photosynaptic Transistor Array with Ultralow Energy Consumption for Artificial-Vision Neural Networks. *Advanced Materials*, John Wiley & Sons, Ltd. ***34***, 2200380. https://doi.org/https://doi.org/10.1002/adma.202200380

[228] **Jiang, L., Xu, C., Wu, X., Zhao, X., Zhang, L., Zhang, G. et al.** (2022) Deep Ultraviolet Light Stimulated Synaptic Transistors Based on Poly(3-hexylthiophene) Ultrathin Films. *ACS Applied Materials & Interfaces*, American Chemical Society. *14*, 11718–26. https://doi.org/10.1021/acsami.1c23986

[229] **Zhu, Y., Qiao, N., Dong, S., Qu, G., Chen, Y., Lu, W. et al.** (2022) Side-Chain Engineering of Polystyrene Dielectrics Toward High-Performance Photon Memories and Artificial Synapses. *Chemistry of Materials*, American Chemical Society. *34*, 6505–17. https://doi.org/10.1021/acs.chemmater.2c01252

[230] **Wang, X., Lu, W., Wei, P., Qin, Z., Qiao, N., Qin, X. et al.** (2022) Artificial Tactile Recognition Enabled by Flexible Low-Voltage Organic Transistors and Low-Power Synaptic Electronics. *ACS Applied Materials & Interfaces*, American Chemical Society. *14*, 48948–59. https://doi.org/10.1021/acsami.2c14625

[231] **Liu, Z., Ju, Z., Ma, S., Li, W., Chen, J., Yang, B. et al.** (2023) Organic Charge-Transfer Complex based Microstructure Interfaces for Solution-Processable Organic Thin-Film Transistors toward Multifunctional Sensing. *Advanced Electronic Materials*, John Wiley & Sons, Ltd. *9*, 2300205. https://doi.org/https://doi.org/10.1002/aelm.202300205

[232] **Gao, L., Liu, C., Peng, Y., Deng, J., Hou, S., Cheng, Y. et al.** (2022) Ultrasensitive flexible NO2 gas sensors via multilayer porous polymer film. *Sensors and Actuators B: Chemical*, *368*, 132113. https://doi.org/https://doi.org/10.1016/j.snb.2022.132113

[233] **Liao, Q., Wang, Y., Uddin, M.A., Chen, J., Guo, H., Shi, S. et al.** (2018) Drastic Effects of Fluorination on Backbone Conformation of Head-to-Head Bithiophene-Based Polymer Semiconductors. *ACS Macro Letters*, American Chemical Society. *7*, 519–24. https://doi.org/10.1021/acsmacrolett.8b00032

[234] **Wang, L., Zheng, C., Fu, J., Hua, J., Chen, J., Gao, J. et al.** (2022) Influence of Molecular Weight of Polymer Electret on the Synaptic Organic Field-Effect Transistor Performance. *Advanced Electronic Materials*, John Wiley & Sons, Ltd. *8*, 2200155. https://doi.org/https://doi.org/10.1002/aelm.202200155

[235] **Tavasli, A., Atila, D.T., Faraji, S., Majewski, L.A. and Trabzon, L.** (2024) Organic phototransistors and their applications as artificial synapses. *Sensors and Actuators A: Physical*, *371*, 115311. https://doi.org/10.1016/j.sna.2024.115311

[236] **Huang, X., Ji, D., Fuchs, H., Hu, W. and Li, T.** (2020) Recent Progress in Organic Phototransistors: Semiconductor Materials, Device Structures and Optoelectronic Applications. *ChemPhotoChem*, *4*, 9–38. https://doi.org/10.1002/cptc.201900198

[237] **He, Z., Han, J., Du, X., Cao, L., Wang, J., Zheng, C. et al.** (2021) Photomemory and Pulse Monitoring Featured Solution-Processed Near-Infrared Graphene/Organic Phototransistor with Detectivity of 2.4 × 1013 Jones. *Advanced Functional Materials*, *31*, 1–8. https://doi.org/10.1002/adfm.202103988

[238] **Maria de Andrade, D., Merces, L., Nawaz, A. and Bof Bufon, C.C.** (2023) Pushing On-Chip Photosensitivity Forward Using Edge-Driven Vertical Organic Phototransistors. *ACS Applied Electronic Materials*, American Chemical Society. *5*, 3038–47. https://doi.org/10.1021/acsaelm.3c00121

[239] **Ji, D., Jiang, T., Zheng, Y., Sun, Y., Wei, Z., Li, L. et al.** (2022) Band-Like Charge Transport in Small-Molecule Thin Film toward High-Performance Organic Phototransistors at Low Temperature. *Advanced Optical Materials*, John Wiley & Sons, Ltd. *10*, 2102484. https://doi.org/https://doi.org/10.1002/adom.202102484

[240] **Yu, H., Zhao, X., Tan, M., Wang, B., Zhang, M., Wang, X. et al.** (2022) Ultraflexible and Ultrasensitive Near-Infrared Organic Phototransistors for Hemispherical Biomimetic Eyes. *Advanced Functional Materials*, John Wiley & Sons, Ltd. *32*, 2206765. https://doi.org/https://doi.org/10.1002/adfm.202206765

[241] **Shi, X., Liu, W., Xu, Y., Jin, C., Zhang, G., Shi, Y. et al.** (2023) Ultraviolet-selective organic phototransistors for low-power skin-inspired nociceptor. *Nano Energy*, Elsevier. *110*, 108372. https://doi.org/10.1016/J.NANOEN.2023.108372

[242] **Tao, J., Sun, W. and Lu, L.** (2022) Organic small molecule semiconductor materials for OFET-based biosensors. *Biosensors and Bioelectronics*, *216*, 114667. https://doi.org/https://doi.org/10.1016/j.bios.2022.114667

[243] **Zhang, Y., Sun, C., Duan, Y., Cheng, S. and Hu, W.** (2023) Carbon dots-functionalized extended gate organic field effect transistor-based biosensors for low abundance proteins. *Nanoscale*, The Royal Society of Chemistry. https://doi.org/10.1039/D3NR03405D

[244] **Niu, Y., Qin, Z., Zhang, Y., Chen, C., Liu, S. and Chen, H.** (2023) Expanding the potential of biosensors: a review on organic field effect transistor (OFET) and organic electrochemical transistor (OECT) biosensors. *Materials Futures*, *2*, 042401. https://doi.org/10.1088/2752-5724/ace3dd

[245] **Wu, Z., Yan, Y., Zhao, Y. and Liu, Y.** (2022) Recent Advances in Realizing Highly Aligned Organic Semiconductors by Solution-Processing Approaches. *Small Methods*, John Wiley & Sons, Ltd. ***6***, 2200752. https://doi.org/https://doi.org/10.1002/smtd.202200752

[246] **Kim, K., Yoo, H. and Lee, E.K.** (2022) New Opportunities for Organic Semiconducting Polymers in Biomedical Applications. Polymers (Basel). MDPI. https://doi.org/10.3390/polym14142960

[247] **Yang, D. and Ma, D.** (2019) Development of Organic Semiconductor Photodetectors: From Mechanism to Applications. *Advanced Optical Materials*, John Wiley & Sons, Ltd. *7*, 1800522. https://doi.org/https://doi.org/10.1002/adom.201800522

[248] **Guo, S., Wang, Z., Chen, X., Li, L., Li, J., Ji, D. et al.** (2022) Low-voltage polymer-dielectric-based organic field-effect transistors and applications. *Nano Select*, John Wiley & Sons, Ltd. *3*, 20–38. https://doi.org/https://doi.org/10.1002/nano.202100051

[249] **Coppola, M.E., Petritz, A., Irimia, C.V., Yumusak, C., Mayr, F., Bednorz, M. et al.** (2023) Pinaceae Pine Resins (Black Pine, Shore Pine, Rosin, and Baltic Amber) as Natural Dielectrics for Low Operating Voltage, Hysteresis-Free, Organic Field Effect Transistors. *Global Challenges*, John Wiley and Sons Inc. *7*. https://doi.org/10.1002/gch2.202300062

[250] **Wan, Y., Qiu, Z., Huang, J., Yang, J., Wang, Q., Lu, P. et al.** (2018) Natural Plant Materials as Dielectric Layer for Highly Sensitive Flexible Electronic Skin. *Small*, John Wiley & Sons, Ltd. *14*, 1801657. https://doi.org/https://doi.org/10.1002/smll.201801657

[251] **Seck, M., Diallo, A.K., Erouel, M., Saadi, M., Tiss, B., Wederni, M.A. et al.** (2021) Dielectric investigation and material properties of almond gum thin films deposited by spray pyrolysis. *Materials Chemistry and Physics*, Elsevier. *272*, 124917. https://doi.org/10.1016/J.MATCHEMPHYS.2021.124917

[252] **Shin, H., Choi, H., Lim, J., Lee, W., Mohit, K., Kim, Y. et al.** (2022) Interfacial engineering of ZrO2 metal-insulator-metal capacitor using Al2O3/TiO2 buffer layer for improved leakage properties. *Journal of Asian Ceramic Societies*, Taylor and Francis Ltd. *10*, 649–59. https://doi.org/10.1080/21870764.2022.2101216

[253] **Gong, Y., Zhao, K., He, H., Cai, W., Tang, N., Ning, H. et al.** (2018) Solution processable high quality ZrO2 dielectric films for low operation voltage and flexible organic thin film transistor applications. *Journal of Physics D: Applied Physics*, Institute of Physics Publishing. *51*. https://doi.org/10.1088/1361-6463/aaac1b

[254] **Yang, F.Y., Hsu, M.Y., Hwang, G.W. and Chang, K.J.** (2010) High-performance poly(3-hexylthiophene) top-gate transistors incorporating TiO2 nanocomposite dielectrics. *Organic Electronics*, Elsevier. *11*, 81–8. https://doi.org/10.1016/j.orgel.2009.10.002

[255] **Mullapudi, G.S.R., Velazquez-Nevarez, G.A., Avila-Avendano, C., Torres-Ochoa, J.A., Quevedo-López, M.A. and Ramírez-Bon, R.** (2019) Low-Temperature Deposition of Inorganic-Organic HfO2-PMMA Hybrid Gate Dielectric Layers for High-Mobility ZnO Thin-Film Transistors. *ACS Applied Electronic Materials*, American Chemical Society. *1*, 1003–11. https://doi.org/10.1021/acsaelm.9b00175

[256] **Tavasli, A., Navidfar, A., Inangil, D., Inangil, G., Aslan, I. and Trabzon, L.** (2024) Hydrophilic sol-gel TiO2 coating on procaine-loaded injector needle for painless clinical treatments. *Colloids and Surfaces A: Physicochemical and Engineering Aspects*, *687*, 133556. https://doi.org/10.1016/j.colsurfa.2024.133556

[257] **Kumar, A., Perinot, A., Sarkar, S.K., Gupta, D., Zorn, N.F., Zaumseil, J. et al.** (2022) Low-temperature solution-processed high-capacitance AlOx dielectrics for low-voltage carbon-based transistors. *Organic Electronics*, Elsevier B.V. *110*. https://doi.org/10.1016/j.orgel.2022.106636

[258] **Park, Y.M., Desai, A., Salleo, A. and Jimison, L.** (2013) Solution-processable zirconium oxide gate dielectrics for flexible organic field effect transistors operated at low voltages. *Chemistry of Materials*, *25*, 2571–9. https://doi.org/10.1021/cm303547a

[259] **Beaulieu, M.R., Baral, J.K., Hendricks, N.R., Tang, Y., Briseño, A.L. and Watkins, J.J.** (2013) Solution processable high dielectric constant nanocomposites based on zro2 nanoparticles for flexible organic transistors. *ACS Applied Materials and Interfaces*, *5*, 13096–103. https://doi.org/10.1021/am404129u

[260] **Lee, S., Han, G., Kim, K.H., Shim, D., Go, D. and An, J.** (2024) High-Performance TiO2/ZrO2/TiO2 Thin Film Capacitor by Plasma-Assisted Atomic Layer Annealing. *ACS Applied Materials & Interfaces*, *16*, 34419–27. https://doi.org/10.1021/acsami.4c06922

[261] **Alvarado-Beltrán, C.G., Almaral-Sánchez, J.L., Mejia, I., Quevedo-López, M.A. and Ramirez-Bon, R.** (2017) Sol-gel PMMA-ZrO2 hybrid layers as gate dielectric for low-temperature ZnO-based thin-film transistors. *ACS Omega*, American Chemical Society. *2*, 6968–74. https://doi.org/10.1021/acsomega.7b00552

[262] **He, W., Xu, W., Peng, Q., Liu, C., Zhou, G., Wu, S. et al.** (2016) Surface Modification on Solution Processable ZrO2 High-k Dielectrics for Low Voltage Operations of Organic Thin Film Transistors. *Journal of Physical Chemistry C*, American Chemical Society. *120*, 9949–57. https://doi.org/10.1021/acs.jpcc.6b03638

[263] **Nam, M., Lee, S., Jeong, H., Yoon, A., Park, J.S. and Jeon, W.** (2024) Optimizing the Crystallinity of a ZrO2 Thin Film Insulator for InGaZnO-Based Metal–Insulator–Semiconductor Capacitors. *Advanced Materials Interfaces*, John Wiley and Sons Inc. *11*. https://doi.org/10.1002/admi.202300883

[264] **Lee, A.J., Lee, S., Han, D.H., Kim, Y. and Jeon, W.** (2023) Enhancing chemisorption efficiency and thin-film characteristics via a discrete feeding method in high-k dielectric atomic layer deposition for preventing interfacial layer formation. *Journal of Materials Chemistry C*, Royal Society of Chemistry. *11*, 6894–901. https://doi.org/10.1039/d3tc00704a

[265] **Yadav, S. and Ghosh, S.** (2016) Amorphous Strontium Titanate Film as Gate Dielectric for Higher Performance and Low Voltage Operation of Transparent and Flexible Organic Field Effect Transistor. *ACS Applied Materials & Interfaces*, American Chemical Society. *8*, 10436–42. https://doi.org/10.1021/acsami.6b02847

[266] **Jiang, Y., Guo, Y. and Liu, Y.** (2017) Engineering of Amorphous Polymeric Insulators for Organic Field-Effect Transistors. *Advanced Electronic Materials*, John Wiley & Sons, Ltd. *3*, 1700157. https://doi.org/https://doi.org/10.1002/aelm.201700157

[267] **Wang, Y., Huang, X., Li, T., Li, L., Guo, X. and Jiang, P.** (2019) Polymer-Based Gate Dielectrics for Organic Field-Effect Transistors. *Chemistry of Materials*, American Chemical Society. *31*, 2212–40. https://doi.org/10.1021/acs.chemmater.8b03904

[268] **Yadav, S. and Ghosh, S.** (2016) Amorphous Strontium Titanate Film as Gate Dielectric for Higher Performance and Low Voltage Operation of Transparent and Flexible Organic Field Effect Transistor. *ACS Applied Materials and Interfaces*, American Chemical Society. *8*, 10436–42. https://doi.org/10.1021/acsami.6b02847

[269] **Patil, B.B., Takeda, Y., Singh, S., Wang, T., Singh, A., Do, T.T. et al.** (2020) Electrode and dielectric layer interface device engineering study using furan flanked diketopyrrolopyrrole–dithienothiophene polymer based organic transistors. *Scientific Reports*, Nature Research. *10*. https://doi.org/10.1038/s41598-020-76962-x

[270] **Wang, B., Huang, W., Chi, L., Al-Hashimi, M., Marks, T.J. and Facchetti, A.** (2018) High- k Gate Dielectrics for Emerging Flexible and Stretchable Electronics. Chem Rev. American Chemical Society. p. 5690–754. https://doi.org/10.1021/acs.chemrev.8b00045

[271] **Ye, H., Ryu, K.Y., Kwon, H.J., Lee, H., Wang, R., Hong, J. et al.** (2023) Amorphous Fluorinated Acrylate Polymer Dielectrics for Flexible Transistors and Logic Gates with High Operational Stability. *ACS Applied Materials and Interfaces*, American Chemical Society. *15*, 32610–20. https://doi.org/10.1021/acsami.3c02010

[272] **Ghadrdan, M., Peyghami, S., Mokhtari, H., Wang, H. and Blaabjerg, F.** (2023) Dissipation Factor as a Degradation Indicator for Electrolytic Capacitors. *IEEE Journal of Emerging and Selected Topics in Power Electronics*, Institute of Electrical and Electronics Engineers Inc. *11*, 1035–44. https://doi.org/10.1109/JESTPE.2022.3183837

[273] **Cai, W., Wilson, J., Zhang, J., Park, S., Majewski, L. and Song, A.** (2019) Low-voltage, flexible InGaZnO thin-film transistors gated with solution-processed, ultra-thin AlxOy. *IEEE Electron Device Letters*, Institute of Electrical and Electronics Engineers Inc. *40*, 36–9. https://doi.org/10.1109/LED.2018.2882464

[274] **Shin, E.Y., Cho, H.J., Jung, S., Yang, C. and Noh, Y.Y.** (2018) A High-k Fluorinated P(VDF-TrFE)-g-PMMA Gate Dielectric for High-Performance Flexible Field-Effect Transistors. *Advanced Functional Materials*, Wiley-VCH Verlag. *28*. https://doi.org/10.1002/adfm.201704780

[275] **Kumar, A., Mondal, S. and Rao, K.S.R.K.** (2016) Low temperature solution processed high-κ ZrO 2 gate dielectrics for nanoelectonics. *Applied Surface Science*, Elsevier B.V. *370*, 373–9. https://doi.org/10.1016/j.apsusc.2016.02.176

[276] **Gunturkun, D., Isci, R., Faraji, S., Sütay, B., Majewski, L.A. and Ozturk, T.** (2023) Synthesis and characterization of naphthalenediimide-thienothiophene-conjugated polymers for OFET and OPT applications. *Journal of Materials Chemistry C*, Royal Society of Chemistry (RSC). https://doi.org/10.1039/d3tc02109b

[277] **Lv, S., Li, L., Mu, Y. and Wan, X.** (2021) Side-chain engineering as a powerful tool to tune the properties of polymeric field-effect transistors. *Polymer Reviews*, Taylor & Francis. *61*, 520–52. https://doi.org/10.1080/15583724.2020.1855195

[278] **Luo, N., Ren, P., Feng, Y., Shao, X., Zhang, H.-L. and Liu, Z.** (2022) Side-Chain Engineering of Conjugated Polymers for High-Performance Organic Field-Effect Transistors. *The Journal of Physical Chemistry Letters*, American Chemical Society. *13*, 1131–46. https://doi.org/10.1021/acs.jpclett.1c03909

[279] **Ozturk, S.E., Isci, R., Faraji, S., Sütay, B., Majewski, L.A. and Ozturk, T.** (2023) Synthesis, Photophysical properties and OFET application of thienothiophene and benzothiadiazole based Donor-π-Acceptor-π (D-π -A-π) type conjugated polymers. *European Polymer Journal*, Pergamon. *191*, 112028. https://doi.org/10.1016/J.EURPOLYMJ.2023.112028

[280] **Yum, S., An, T.K., Wang, X., Uddin, M.A., Nguyen, T.L., Xu, S. et al.** (2014) Thienothiophene-benzotriazole-based semicrystalline linear copolymers for organic field effect transistors. *Pure and Applied Chemistry*, Walter de Gruyter GmbH. *86*, 1293–302. https://doi.org/10.1515/pac-2014-0205

[281] **Yum, S., An, T.K., Wang, X., Lee, W., Uddin, M.A., Kim, Y.J. et al.** (2014) Benzotriazole-containing planar conjugated polymers with noncovalent conformational locks for thermally stable and efficient polymer field-effect transistors. *Chemistry of Materials*, American Chemical Society. *26*, 2147–54. https://doi.org/10.1021/cm4042346

[282] **Isci, R., Rahimi Varzeghani, A., Kaya, K., Sütay, B., Tekin, E. and Ozturk, T.** (2022) Triphenylamine/Tetraphenylethylene Substituted 4-Thieno[3,2-b]thiophen-3-ylbenzonitriles: Synthesis, Photophysical-Electronic Properties, and Applications. *ACS Sustainable Chemistry & Engineering*, American Chemical Society. *10*, 1605–15. https://doi.org/10.1021/acssuschemeng.1c07240

[283] **Amna, B., Isci, R., Siddiqi, H.M., Majewski, L.A., Faraji, S. and Ozturk, T.** (2022) High-performance, low-voltage organic field-effect transistors using thieno[3,2-b]thiophene and benzothiadiazole co-polymers. *Journal of Materials Chemistry C*, The Royal Society of Chemistry. *10*, 8254–65. https://doi.org/10.1039/D2TC01222G

[284] **Sun, X., Di, C. an and Liu, Y.** (2010) Engineering of the dielectric-semiconductor interface in organic field-effect transistors. J Mater Chem. p. 2599–611. https://doi.org/10.1039/b921449f

[285] **Lee, W.H., Wang, C.C., Chen, W.T. and Ho, J.C.** (2008) Characteristic of organic thin film transistor with a high-k insulator of nano-TiO2 and polyimide blend. *Japanese Journal of Applied Physics*, *47*, 8955–60. https://doi.org/10.1143/JJAP.47.8955

[286] **Lee, E.K., Kim, J.Y., Chung, J.W., Lee, B.L. and Kang, Y.** (2014) Photo-crosslinkable polymer gate dielectrics for hysteresis-free organic field-effect transistors with high solvent resistance. *RSC Advances*, *4*, 293–300. https://doi.org/10.1039/c3ra43890b

CURRICULUM VITAE

Name Surname : Aybüke TAVASLI

EDUCATION :

- **B.Sc.** : 2017, Tekirdağ Namık Kemal University, Faculty of Engineering, Biomedical Engineering Department

- **M.Sc.** : 2019, İstanbul Technical University, Department of Materials Science and Engineering, Materials Science and Engineering Programme

PROFESSIONAL EXPERIENCE AND REWARDS:

- 2024, Poster award in the best poster presentation category, 18th International Nanoscience and Nanotechnology Conference, NanoTr'18, Koç University
- 2017, Runner-up award in Class of 2016 - 2017, high honor degree in 21st graduation ceremony
- 2017, Poster award in poster presentation, 6th Biomedical Engineering Symposium, Tekirdağ Namık Kemal University

PUBLICATIONS, PRESENTATIONS AND PATENTS ON THE THESIS:

- **Tavasli, A., Trabzon, T., Faraji, S.** 2024: Natural materials for organic field-effect transistor designs and their sensor applications. 18th International Nanoscience and Nanotechnology Conference, August 26-28, 2024 Koç University, İstanbul, Türkiye.
- **Tavasli, A., Atila, D. T., Faraji, S., Majewski, L. A., Trabzon, L.** 2024. Organic phototransistors and their applications as artificial synapses, *Sensors and Actuators A: Physical*, 371(115311). Doi: 10.1016/j.sna.2024.115311
- **Faraji, S., Tall, A., Mohammadian, N., Seck, M., Saadi, M., Tavasli, A., Erouel, M., Khirouni, K., Diallo, A. K., Majewski, L. A.** 2023. Towards sustainable, solution-processed organic field-effect transistors using cashew gum as the gate dielectric. *Front Mater,* 10(1280543). Doi:10.3389/fmats.2023.1280543

- **Faraji, S., İşçi, R., Tavaslı, A., Majewski, L. A., Diallo, A. K., Öztürk, T.** 2023: Towards sustainable, environment-friendly and low-waste gas and photoactivated sensors for low-power health and air monitoring and medical diagnostics. 5th International Engineering and Technology Management Summit, October 19-21, 2023 İstanbul Technical University & Bahçeşehir University, İstanbul, Türkiye.
- **Tavasli, A., Gómez-Lor, B., Woo, H. Y., Uddin, M. A.,** 2023: Organic semiconductor design for efficient organic photovoltaic cells. 1st International Workshop in Organic Chemistry and Functional Materials, September 8, 2023 Universidad Rey Juan Carlos, Madrid, Spain.
- **Tavasli, A., Gurunlu, B., Gunturkun, D., Isci, R., Faraji, S.** 2022. A review on solution-processed organic phototransistors and their recent developments, *Electronics*, 11(3), 316. Doi: 10.3390/electronics11030316

OTHER PUBLICATIONS, PRESENTATIONS AND PATENTS:

- **Tavasli, A., Navidfar, A., Inangil, D., Inangil, G., Aslan, I., Trabzon, L.** 2024. Hydrophilic sol-gel TiO_2 coating on procaine-loaded injector needle for painless clinical treatments, *Colloids and Surfaces A: Physicochemical and Engineering Aspects*, 687(133556). Doi: 10.1016/j.colsurfa.2024.133556
- **Tavasli, A., Kocaaga, B., Guner, F. S.** 2023. Development of procaine loaded transdermal patches based on biopolymer pectin, castor oil, and polyethylene glycol for controllable drug release studies and their characterizations, *ChemistrySelect*, 8(34). Doi: 10.1002/slct.202301115
- **Tavasli, A., Kocaaga, B., Guner, F. S.,** 2019: Painkiller drug loaded transdermal patch. 1st Chemical Engineering Symposium, April, 2019 İstanbul Technical University, İstanbul, Türkiye.
- **Tavasli, A., Atam, D., Taşdelen, B.,** 2017: Fabrication of anodes for copper-based batteries in biomedical applications and their characterizations. 6th Biomedical Engineering Symposium, April, 2017 Tekirdağ Namık Kemal University, Tekirdağ, Türkiye.
- **Tavasli, A., Taşdelen, B.** Semi-interpenetration with conducting polyanilines on poly(acrylamide-co-kaolin) composite, 2017. 17th International Electric-Electronic, Computer, Biomedical Engineering Scientific Conference, *IEEE Xplore Library,* 1-3. Doi: 10.1109/EBBT.2017.